Application of Dynamic Fracture Mechanics Concepts to Composites: Annual Report 1998

by

J.J. Mason

Solid Mechanics Group

Department of Aerospace and Mechanical Engineering

University of Notre Dame

Notre Dame, Indiana 46556

Structural/Solid Mechanics
Laboratory Report No. 98/3

Application of Dynamic Fracture Mechanics Concepts to Composites: Annual Report 1998

by

J.J. Mason

Department of Aerospace and Mechanical Engineering
University of Notre Dame

Notre Dame, Indiana 46556
June, 1998

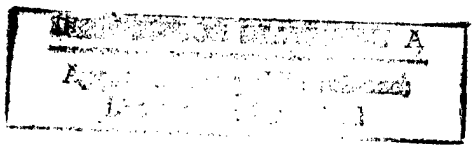

Structural/Solid Mechanics
Laboratory Report No. 98/3

UNIVERSITY OF NOTRE DAME

Aerospace and Mechanical Engineering

Founded 1842

FITZPATRICK HALL

August 25, 1998

Defense Technical Information Center
8725 John J. Kingman Road
STE 0944
Ft. Belvoir, VA 22060-6218

With this letter I am submitting two copies of the second annual report for ONR-YIP grant, number N00014-96-1-0774, entitled "On the Application of Dynamic Fracture Mechanics to Continuous Fiber Reinforced Composite Materials." A copy of SF-298 is included with each report.

Respectfully,

James Mason
Assistant Professor
Department of Aerospace and
Mechanical Engineering

NOTRE DAME,
INDIANA 46556-5637

219/631-5430
FAX 219/631-8341

Application of Dynamic Fracture Mechanics Concepts to Composites: Annual Report 1998

J.J. Mason [1]
Department of Aerospace and Mechanical Engineering
University of Notre Dame
Notre Dame, IN 46556

June, 1998

[1]Assistant Professor, Principal Investigator

Abstract

This report summarizes the work completed in the year June 1997–May 1998. The report is divided into two parts, one covering the work on orthotropic composites and the other covering the work on isotropic metals. Each part consists of two chapters which stand alone, each having been submitted, accepted or prepared for publication in a refereed journal. Separate bibliographies are given for parts I and II. The work on composites has succeeded in producing fundamental, dynamic Green's functions solutions for cracks in orthotropic materials. These solutions may be used in calculating the stress intensity factor history on stationary cracks subjected to dynamic loading and may be very useful in predicting crack initiation under such conditions. Currently, experimental investigation of the application of these solutions to crack initiation in composites in two different configurations is beginning. It is expected that a report on that work will be submitted next year. The work on metals has been successful in experimentally demonstrating the usefulness of the dynamic stress intensity factor in predicting shear failure in metals under impact loads. This demonstration is predicated on the assumption that small scale yielding conditions exist in the experiments. The last chapter reflects an ongoing experimental investigation into the validity of that assumption. It seems to suggest that the assumption is correct, but further, more conclusive results are sought.

Contents

List of Figures

List of Tables

Part I

Investigations of Orthotropic Composites

Chapter 1

Fundamental Solutions for the Stress Intensity Factor Evolution in Finite Cracks in Orthotropic Materials

Co-authored with C. Rubio-Gonzalez and submitted to International Journal of Fracture

Abstract

The elastodynamic response of an infinite orthotropic material with finite crack under concentrated loads is examined. Solution for the stress intensity factor history around the crack tips is found. Laplace and Fourier transforms are employed to solve the equations of motion leading to a Fredholm integral equation on the Laplace transform domain. The dynamic stress intensity factor history can be computed by numerical Laplace transform inversion of the solution of the Fredholm equation. Numerical values of the dynamic stress intensity factor history for some example materials are obtained. This solution can be used as a Green's function to solve dynamic problems involving finite cracks.

1.1 Introduction

With the growing use of composite materials in engineering applications, the need for fundamental understanding of their mechanical behavior becomes imperative. Dynamic crack propagation in composite materials and the response of cracked composite bodies under dy-

namic loads is a subject that has been investigated, both theoretically and experimentally, to a large extent. But while many exact solutions exist for the stress field around stationary and propagating cracks in isotropic solids, (Freund 1990, Parton and Boriskovsky 1989) only a few solutions are available for the stress field around stationary (Kassir and Bandyopadhyay 1983) and propagating (Stroh 1962) cracks in anisotropic solids. This may be due in part, to the mathematical complexity of such problems. Integral transform methods are usually the techniques employed to solve problems involving cracked orthotropic bodies subjected to impact loads (Kassir and Bandyopadhyay 1983, Shindo and Nozaki 1991a, Shindo and Nozaki 1991b). This approach leads to a Fredholm integral equation on the Laplace transform domain, rather than a Weiner-Hopf equation (Freund 1974) as is found for isotropic materials. The dynamic stress intensity factor on the time domain is recovered, in the most difficult step of the analysis, by numerical inversion of the solution of the Fredholm equation. This process can be numerically challenging and computationally intensive.

In this work, the problem of an infinite orthotropic body with a finite crack subjected to suddenly applied line loads on the faces is examined. The crack lies on the principal axes of the material. Roessig and Mason (1997) have shown that a solution of this problem is very useful in the analysis of the impact of blunt objects and fragments on solids, and the line load solution derived here can be used as a Green's function in a variety of problems involving finite cracks. The Green's function presented here, the solution related to the geometry shown schematically in Figure 1.1, has not been reported to date although the quasi-static solution is presented by Isida (1972) as

$$K_I(t=\infty) = \frac{q}{\sqrt{\pi a}}\left(\sqrt{\frac{a+\chi_0}{a-\chi_0}} + \sqrt{\frac{a-\chi_0}{a+\chi_0}}\right) \tag{1.1}$$

where χ_o, q and a are defined in the figure. The solution of the problem for the isotropic case should be identical to that of Freund (1974) for a semi-infinite crack for times $\tau \leq (a+\chi_0)/c_d$ where c_d is the dilatational wave speed. Freund solved the elastic wave propagation problem in the isotropic infinite body with semi-infinite crack by linear superposition of a fundamental dislocation solution. His exact solution for this problem serves as a useful verification of the

numerical Laplace transform inversion methods used here.

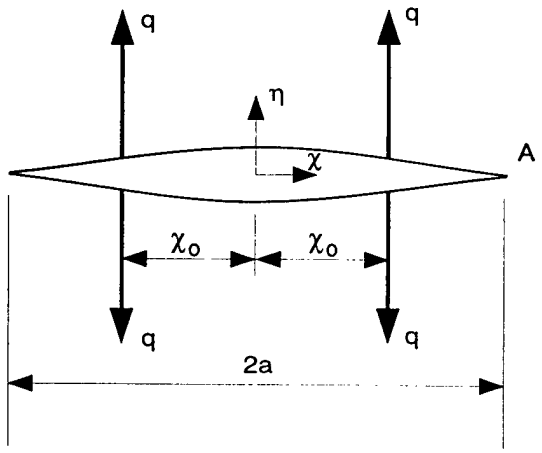

Figure 1.1: Schematic of the finite crack geometry with two pairs of opening concentrated loads.

As noted before, the most difficult step in the solution method is the numerical inversion of the Laplace transform. A method using Jacobi or Legendre polynomials to represent the function in time has been used in the past to invert the Laplace transform of the stress intensity factor (Kassir and Bandyopadhyay 1983, Shindo and Nozaki 1991a, Shindo and Nozaki 1991b). This type of spectral representation of the function in time leads to smoothing of the function and the loss of information at discontinuities. As a consequence, it is believed (Parton 1989) that such an approach cannot lead to the exact determination of the points of discontinuity of the stress intensity factor. It is expected in the problem analyzed here, from the nature of Fruend's (1974) solution for isotropic materials, that the stress intensity factor will be discontinuous and that the points of discontinuity will have physical meaning in terms of the arrival of various wave types at the crack tip. Hence, it is desirable to capture the discontinuities and, consequently, a different technique for the numerical inversion of the Laplace transform of the stress intensity factor is required. Under certain circumstances the Laplace transform is equivalent to the Fourier transform (Papoulis 1962). That is the case for this problem and therefore the inverse fast Fourier transform is used in this work to recover the stress intensity factor in the time domain. It was found that using other methods to invert the Laplace transform, e.g. Honig and Hirdes (1984), gave similar results although

they required more computational effort.

Two problems with different load configuration are solved. First the problem of a finite crack with two pairs of opening concentrated loads at $\chi = \pm\chi_0$ (figure 1.1) is considered. The second problem is that illustrated in figure 1.2(a) where the crack has only a single pair of concentrated loads at $\chi = \chi_0$. The quasi-static stress intensity factor for the second problem, figure 1.2(a), at the crack tip $x = +a$ is given by (Isida 1972)

$$K_I(t=\infty) = \frac{q}{\sqrt{\pi a}}\sqrt{\frac{a+\chi_0}{a-\chi_0}}. \tag{1.2}$$

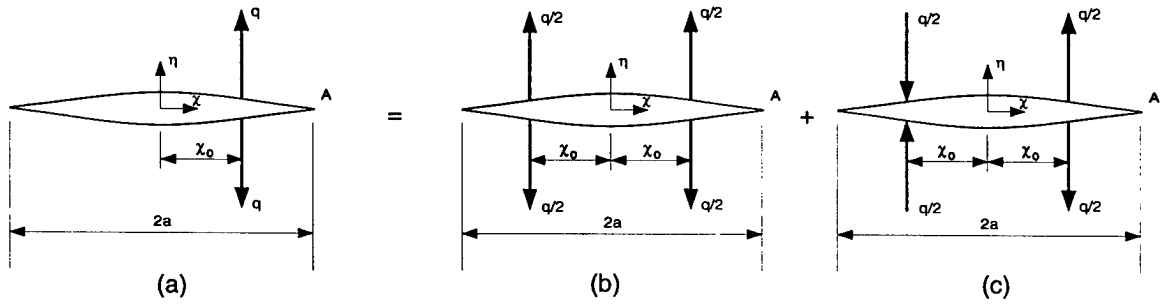

Figure 1.2: Schematic of the finite crack geometry with a single pair of concentrated loads. (a) Original problem which is solved by a superposition of, (b) a symmetric problem and, (c) an antisymmetric problem.

1.2 Governing Equations

Consider the plane problem of an infinite orthotropic medium containing a finite crack, Figure 1.1. Let E_i, μ_{ij} and ν_{ij} $(i,j = 1,2,3)$ be the engineering elastic constants of the material where the indices 1, 2, and 3 correspond to the directions (χ, η, z) of a system of Cartesian coordinates chosen to coincide with the axes of material orthotropy. The crack plane is $\eta = 0$ and the origin of the $\chi\eta$ axes is the mid-point of the distance between the crack tips. Henceforward, the coordinate χ will be normalized with respect to a. The normalized coordinates $x = \chi/a$ and $y = \eta/a$ are introduced such that the crack tips are located at $x = \pm 1$ and the loads at $x = \pm x_0$. The normalized time t is introduced in the form $t = c_s\tau/a$ where $c_s = \sqrt{\mu_{12}/\rho}$ with ρ being the mass density. Concentrated normal forces of magnitude q are applied as shown and tend to separate the crack faces.

The problem under consideration is restricted to two dimensions with wave propagation in the $x-y$ plane only. By setting all the derivatives with respect to z to be zero, it is readily shown that the displacement equations of motion (Nayfeh 1995) in the normalized coordinates reduce to

$$c_{11}\frac{\partial^2 u}{\partial x^2}+\frac{\partial^2 u}{\partial y^2}+(1+c_{12})\frac{\partial^2 v}{\partial x\partial y} = \frac{\partial^2 u}{\partial t^2}, \tag{1.3}$$

$$\frac{\partial^2 v}{\partial x^2}+c_{22}\frac{\partial^2 v}{\partial y^2}+(1+c_{12})\frac{\partial^2 u}{\partial x\partial y} = \frac{\partial^2 v}{\partial t^2}, \tag{1.4}$$

where u and v are the x and y components of the normalized displacement vector and c_{11}, c_{12} and c_{22} are non-dimensional parameters related to the elastic constants by the relations:

$$\begin{aligned} c_{11} &= \frac{E_1}{\mu_{12}[1-(E_2/E_1)\nu_{12}^2]}, \\ c_{22} &= (E_2/E_1)c_{11}, \\ c_{12} &= \nu_{12}c_{22}=\nu_{21}c_{11}, \end{aligned} \tag{1.5}$$

for generalized plane stress, and by

$$\begin{aligned} c_{11} &= \frac{E_1}{\mu_{12}\Delta}(1-\nu_{23}\nu_{32}), \\ c_{22} &= \frac{E_2}{\mu_{12}\Delta}(1-\nu_{13}\nu_{31}), \\ c_{12} &= \frac{E_1}{\mu_{12}\Delta}(\nu_{21}+\frac{E_2}{E_1}\nu_{13}\nu_{32}), \\ \Delta &= 1-\nu_{12}\nu_{21}-\nu_{23}\nu_{32}-\nu_{31}\nu_{13}-\nu_{12}\nu_{23}\nu_{31}-\nu_{13}\nu_{21}\nu_{32}, \end{aligned} \tag{1.6}$$

for plane strain. In the orthotropic solid, c_s represents the velocity of the in-plane shear wave propagating along the the principal material axes. The stresses are related to the displacements by the equations:

$$\begin{aligned} \frac{\sigma_x}{\mu_{12}} &= c_{11}\frac{\partial u}{\partial x}+c_{12}\frac{\partial v}{\partial y}, \\ \frac{\sigma_y}{\mu_{12}} &= c_{12}\frac{\partial u}{\partial x}+c_{22}\frac{\partial v}{\partial y}, \\ \frac{\tau_{xy}}{\mu_{12}} &= \frac{\partial u}{\partial y}+\frac{\partial v}{\partial x}. \end{aligned} \tag{1.7}$$

The corresponding boundary conditions are

$$\begin{aligned} \sigma_y(x,0,t) &= -\sigma(x)H(t) \quad \text{for} \quad |x|<1, \\ \tau_{xy}(x,0,t) &= 0 \qquad \text{for} \quad |x|<\infty, \\ v(x,0,t) &= 0 \qquad \text{for} \quad |x|>1, \end{aligned} \tag{1.8}$$

in addition to the condition of zero displacements at infinity and zero initial conditions. The traction $\sigma(x)$ is a known function of x and $H(t)$ is the Heaviside step function.

Equations (1.3), (1.4) and (1.8) constitute a mathematical statement of the problem. Because the nature of the boundary conditions in equation (1.8), this is a mixed boundary value problem. For the moment, $\sigma(x)$ represents a general load on the crack faces, later it will be substituted with a function representing the line loads.

1.3 Method of Solution

The method of solution of the governing equations presented here follows that of Kassir and Bandyopadhyay (1983), Chen and Sih (1977), and Sneddon (1966). In equations (1.3) and (1.4), the time variable may be removed by application of the Laplace transform

$$f^*(p) = \int_0^\infty f(t)\, e^{-pt}\, dt, \quad f(t) = \frac{1}{2\pi i}\int_{Br} f^*(p)\, e^{pt}\, dt, \tag{1.9}$$

where Br denotes the Bromwich path of integration which is a line parallel to the imaginary axis in the p-plane. Applying relations (1.9) to equations (1.3) and (1.4) and assuming zero initial conditions for the displacements and velocities, the transformed field equations become

$$c_{11}\frac{\partial^2 u^*}{\partial x^2} + \frac{\partial^2 u^*}{\partial y^2} + (1+c_{12})\frac{\partial^2 v^*}{\partial x \partial y} - p^2 u^* = 0, \tag{1.10}$$

$$\frac{\partial^2 v^*}{\partial x^2} + c_{22}\frac{\partial^2 v^*}{\partial y^2} + (1+c_{12})\frac{\partial^2 u^*}{\partial x \partial y} - p^2 v^* = 0, \tag{1.11}$$

where the transformed displacement components, u^* and v^*, are now functions of the variables x, y, and p. The application of the Laplace transform to the boundary conditions (1.8)

gives

$$\begin{aligned} \sigma_y^*(x,0,p) &= -\sigma(x)\frac{1}{p} \quad \text{for} \quad |x|<1, \\ \tau_{xy}^*(x,0,p) &= 0 \qquad \text{for} \quad |x|<\infty, \\ v^*(x,0,p) &= 0 \qquad \text{for} \quad |x|>1. \end{aligned} \tag{1.12}$$

To obtain a solution of the differential equations (1.10) and (1.11) subject to conditions (1.12), we exploit the symmetry of the problem by letting

$$u^*(x,y,p) = \int_0^\infty A(s,y,p)\sin(sx)ds, \tag{1.13}$$

$$v^*(x,y,p) = \int_0^\infty B(s,y,p)\cos(sx)ds, \tag{1.14}$$

where A and B are the Fourier sine and cosine transforms of the Laplace transform of the displacements, u^* and v^*, respectively, and are yet to be determined. Substituting these transforms into equations (1.10) and (1.11), the functions A and B are found to satisfy the simultaneous ordinary differential equations

$$(c_{11}s^2+p^2)A - \frac{d^2A}{dy^2} + (1+c_{12})s\frac{dB}{dy} = 0, \tag{1.15}$$

$$(s^2+p^2)B - c_{22}\frac{d^2B}{dy^2} - (1+c_{12})s\frac{dA}{dy} = 0. \tag{1.16}$$

The solution of these equations which vanishes for $|y|\to\infty$ is

$$\begin{aligned} A(s,y,p) &= A_1(s,p)e^{-\gamma_1 y} + A_2(s,p)e^{-\gamma_2 y}, \\ B(s,y,p) &= \frac{\alpha_1}{s}A_1(s,p)e^{-\gamma_1 y} + \frac{\alpha_2}{s}A_2(s,p)e^{-\gamma_2 y}, \end{aligned} \tag{1.17}$$

where A_1 and A_2 are arbitrary functions and $\alpha_j(s,p)$ stands for the functions

$$\alpha_j(s,p) = \frac{c_{11}s^2+p^2-\gamma_j^2}{(1+c_{12})\gamma_j}, \quad j=1,2 \tag{1.18}$$

with γ_1^2 and γ_2^2 being two distinct roots of the quadratic equation

$$c_{22}\gamma^4 + [(c_{12}^2+2c_{12}-c_{11}c_{22})s^2 - (1+c_{22})p^2]\gamma^2 + (c_{11}s^2+p^2)(s^2+p^2) = 0. \tag{1.19}$$

It can be shown that for many materials the roots γ_1 and γ_2 are real and positive and the expressions for the displacements in the Laplace transform domain become:

$$u^* = \int_0^\infty (A_1 e^{-\gamma_1 y} + A_2 e^{-\gamma_2 y}) \sin(sx) ds, \tag{1.20}$$

$$v^* = \int_0^\infty (\alpha_1 A_1 e^{-\gamma_1 y} + \alpha_2 A_2 e^{-\gamma_2 y}) \frac{\cos(sx)}{s} ds, \tag{1.21}$$

and using (1.7) the corresponding expression for τ_{xy}^* is given by

$$\tau_{xy}^* = -\mu_{12} \int_0^\infty [(\alpha_1 + \gamma_1) A_1 e^{-\gamma_1 y} + (\alpha_2 + \gamma_2) A_2 e^{-\gamma_2 y}] \sin(sx) ds. \tag{1.22}$$

Applying the second condition of (1.12) to equation (1.22) yields

$$\begin{aligned} A_2(s,p) &= -\beta A_1(s,p), \\ \beta &= \frac{\alpha_1 + \gamma_1}{\alpha_2 + \gamma_2}. \end{aligned} \tag{1.23}$$

Therefore the expressions for the transformed components of displacement become

$$u^*(x,y,p) = \int_0^\infty (e^{-\gamma_1 y} - \beta e^{-\gamma_2 y}) A_1(s,p) \sin(sx) ds, \tag{1.24}$$

$$v^*(x,y,p) = \int_0^\infty (\alpha_1 e^{-\gamma_1 y} - \beta \alpha_2 e^{-\gamma_2 y}) \frac{A_1(s,p)}{s} \cos(sx) ds, \tag{1.25}$$

and the associated stress components are given by

$$\sigma_x^* = \mu_{12} \int_0^\infty [(c_{11} s^2 - \alpha_1 \gamma_1 c_{12}) e^{-\gamma_1 y} - (c_{11} s^2 - \alpha_2 \gamma_2 c_{12}) \beta e^{-\gamma_2 y}] \frac{A_1(s,p)}{s} \cos(sx) ds, \tag{1.26}$$

$$\sigma_y^* = \mu_{12} \int_0^\infty [(c_{12} s^2 - \alpha_1 \gamma_1 c_{22}) e^{-\gamma_1 y} - (c_{12} s^2 - \alpha_2 \gamma_2 c_{22}) \beta e^{-\gamma_2 y}] \frac{A_1(s,p)}{s} \cos(sx) ds, \tag{1.27}$$

$$\tau_{xy}^* = -\mu_{12} \int_0^\infty (\alpha_1 + \gamma_1)[e^{-\gamma_1 y} - e^{-\gamma_2 y}] A_1(s,p) \sin(sx) ds. \tag{1.28}$$

Introducing the functions

$$D(s,p) = \frac{1}{s}(\alpha_1 - \beta \alpha_2) A_1(s,p), \tag{1.29}$$

$$F(s,p) = \frac{1}{(\alpha_1 - \beta \alpha_2) s \xi} [c_{12} s^2 - \alpha_1 \gamma_1 c_{22} - \beta (c_{12} s^2 - \alpha_2 \gamma_2 c_{22})], \tag{1.30}$$

$$\begin{aligned} \xi = \frac{1}{c_{11}(1 + c_{12})(N_1 + N_2)} &\{(c_{12}^2 + c_{12} - c_{11} c_{22})(c_{12} N_1 N_2 - c_{11}) \\ &- c_{22}[c_{12} N_1^2 N_2^2 + c_{11}(N_1^2 + N_1 N_2 + N_2^2)]\}, \end{aligned} \tag{1.31}$$

$$N_{1,2}^2 = \frac{1}{2c_{22}} \{c_{11} c_{22} - c_{12}^2 - 2c_{12} \pm [(c_{11} c_{22} - c_{12}^2 - 2c_{12})^2 - 4 c_{11} c_{22}]^{1/2}\}, \tag{1.32}$$

and in view of the first and third boundary conditions in (1.12), equation (1.25) and (1.27) yield the following pair of dual integral equations for the determination of the function $D(s,p)$

$$\int_0^\infty s\, F(s,p)\, D(s,p)\cos(sx)ds = -\frac{\sigma(x)}{\mu_{12}\xi p} \qquad 0<x<1, \tag{1.33}$$

$$\int_0^\infty D(s,p)\cos(sx)ds = 0 \qquad x>1, \tag{1.34}$$

where $\sigma(x)$ is the distributed load along the crack faces. The constant ξ in (1.30) has been chosen such that for large s, the function $F(s,p)$ becomes

$$F(s,p) = 1 + O(1/s)$$

Using $\cos(sx) = \sqrt{\frac{sx\pi}{2}}J_{-1/2}(sx)$ and defining $\bar{D}(s,p) = s^{1/2}D(s,p)$ and $r_1(s,p) = F(s,p) - 1$, these last equations can be written as

$$\int_0^\infty s[r_1(s,p)+1]\bar{D}(s,p)J_{-1/2}(sx)ds = g(x) \qquad 0<x<1,$$

$$\int_0^\infty \bar{D}(s,p)J_{-1/2}(sx)ds = 0 \qquad x>1,$$

where

$$g(x) = -\sqrt{\frac{2}{\pi x}}\frac{\sigma(x)}{\mu_{12}\xi p}. \tag{1.35}$$

Following the procedure given by Sneddon (1966), the function $D(s,p)$ of the original integral equations (1.33) and (1.34) can be found in terms of another unknown function, $\Phi(r,p)$, in the form

$$D(s,p) = -\frac{q}{\pi a\mu_{12}\xi p}\int_0^1 w^{1/2}\Phi(w,p)J_0(sw)dw. \tag{1.36}$$

where $\Phi(r,p)$ satisfies the following Fredholm integral equation

$$\Phi(r,p) + \int_0^1 \Phi(u,p)L(r,u,p)du = H(r), \tag{1.37}$$

with symmetrical kernel

$$L(r,u,p) = (ru)^{1/2}\int_0^\infty w\Big[F(w,p)-1\Big]J_0(rw)J_0(uw)dw, \tag{1.38}$$

and free term

$$H(r) = \frac{2a\sqrt{r}}{q} \int_0^r \frac{\sigma(w)}{\sqrt{r^2 - w^2}} dw. \tag{1.39}$$

For the case of concentrated loads as illustrated in figure 1.1, we have $\sigma(x) = \frac{q}{a}\delta(x - x_0)$ where the denominator appears due to the normalization of x, the free term becomes

$$H(r) = \begin{cases} \frac{2\sqrt{r}}{\sqrt{r^2 - x_0^2}} & \text{for} \quad x_0 < r \\ 0 & \text{for} \quad x_0 > r. \end{cases} \tag{1.40}$$

Note that the free term is discontinuous in r. Integrating $D(s,p)$ by parts in equation (1.36) gives

$$D(s,p) = -\frac{q}{\pi a \mu_{12} \xi p s} \left\{ \Phi(1,p) J_1(s) - \int_0^1 w J_1(sw) \frac{d}{dw} \left[w^{-1/2} \Phi(w,p) \right] dw \right\}. \tag{1.41}$$

From equation (1.27) we know that in the Laplace transform domain σ^*_{yy} is

$$\sigma^*_{yy}(x,0,p) = \mu_{12} \xi \int_0^\infty s \; F(s,p) \; D(s,p) \cos(sx) ds.$$

and substituting (1.41) it is found that

$$\begin{aligned} \sigma^*_{yy}(x,0,p) \;\; = \;\; & -\frac{q}{\pi a} \left[\frac{\Phi(1,p)}{p} \int_0^\infty F(s,p) J_1(s) \cos(sx) ds \right] \\ & -\frac{q}{\pi a p} \left\{ \int_0^\infty F(s,p) \cos(sx) ds \int_0^1 w J_1(sw) \frac{d}{dw} \left[w^{-1/2} \Phi(w,p) \right] dw \right\} \end{aligned} \tag{1.42}$$

As shown by Kassir and Bandyopadhyay (1983) the stress intensity factor extracted from (1.42) is

$$K_I(t) = \frac{q}{\sqrt{\pi a}} \mathcal{L}^{-1} \left\{ \frac{\Phi(1,p)}{p} \right\}, \tag{1.43}$$

where $\mathcal{L}^{-1}$ denotes the inverse of the Laplace transform.

1.4 A superposition problem

The problem of a finite crack with a single pair of impact concentrated loads (figure 1.2(a)) may be solved. As illustrated in figure 1.2, this problem can be treated by a superposition of the two problems shown, that is, one with a symmetric (figure 1.2(b)) and the other with an antisymmetric (figure 1.2(c)) displacement field. The symmetric part is just the

problem solved above with a load of magnitude $q/2$ instead of q. To solve the antisymmetric part we follow a similar procedure. Application of Laplace and Fourier transforms leads to a reduction of the governing equations to a system of dual integral equation. The stress intensity factor in the Laplace domain is obtained for each problem, and then they are superimposed in this domain. Finally the Laplace inversion is performed on the sum to obtain $K_I(t)$ for the original problem. For the symmetric part (figure 1.2(b)), the stress intensity factor $K_{Is}(t)$ is given by equation (1.43) with a correction in the load magnitude

$$K_{Is}(t) = \frac{q}{2\sqrt{\pi a}}\,\mathcal{L}^{-1}\left\{\frac{\Phi(1,p)}{p}\right\}. \tag{1.44}$$

1.4.1 Antisymmetric loading

To obtain a solution of the differential equations (1.10) and (1.11) subject to conditions (1.12) for the antisymmetric case, let

$$u^*(x,y,p) = \int_0^\infty A(s,y,p)\cos(sx)ds, \tag{1.45}$$

$$v^*(x,y,p) = -\int_0^\infty B(s,y,p)\sin(sx)ds, \tag{1.46}$$

where A and B are the Fourier cosine and sine transforms of the Laplace transform of the displacements, and are yet to be determined. Substituting these transforms into equations (1.10) and (1.11), the functions A and B are found to satisfy the simultaneous ordinary differential equations (1.15) and (1.16), therefore the variables α_j are given by (1.18) and γ_j by the solution of (1.19). The expressions for the displacements in the Laplace plane become:

$$u^* = \int_0^\infty (A_1 e^{-\gamma_1 y} + A_2 e^{-\gamma_2 y})\cos(sx)ds, \tag{1.47}$$

$$v^* = -\int_0^\infty (\alpha_1 A_1 e^{-\gamma_1 y} + \alpha_2 A_2 e^{-\gamma_2 y})\frac{\sin(sx)}{s}ds, \tag{1.48}$$

and using (1.7) the corresponding expression for τ^*_{xy} is given by

$$\tau^*_{xy} = -\mu_{12}\int_0^\infty [(\alpha_1+\gamma_1)A_1 e^{-\gamma_1 y} + (\alpha_2+\gamma_2)A_2 e^{-\gamma_2 y}]\cos(sx)ds. \tag{1.49}$$

Applying the second condition of (1.12) to equation (1.49) yields

$$\begin{aligned} A_2(s,p) &= -\beta A_1(s,p), \\ \beta &= \frac{\alpha_1+\gamma_1}{\alpha_2+\gamma_2}. \end{aligned} \tag{1.50}$$

Therefore the expressions for the transformed components of displacement become

$$u^*(x,y,p) = \int_0^\infty (e^{-\gamma_1 y} - \beta e^{-\gamma_2 y}) A_1(s,p)\cos(sx)ds, \tag{1.51}$$

$$v^*(x,y,p) = -\int_0^\infty (\alpha_1 e^{-\gamma_1 y} - \beta\alpha_2 e^{-\gamma_2 y})\frac{A_1(s,p)}{s}\sin(sx)ds, \tag{1.52}$$

and the associated stress components are given by

$$\sigma_x^* = -\mu_{12}\int_0^\infty [(c_{11}s^2 - \alpha_1\gamma_1 c_{12})e^{-\gamma_1 y} - (c_{11}s^2 - \alpha_2\gamma_2 c_{12})\beta e^{-\gamma_2 y}]\frac{A_1(s,p)}{s}\sin(sx)ds, \tag{1.53}$$

$$\sigma_y^* = -\mu_{12}\int_0^\infty [(c_{12}s^2 - \alpha_1\gamma_1 c_{22})e^{-\gamma_1 y} - (c_{12}s^2 - \alpha_2\gamma_2 c_{22})\beta e^{-\gamma_2 y}]\frac{A_1(s,p)}{s}\sin(sx)ds, \tag{1.54}$$

$$\tau_{xy}^* = -\mu_{12}\int_0^\infty (\alpha_1+\gamma_1)[e^{-\gamma_1 y} - e^{-\gamma_2 y}]A_1(s,p)\cos(sx)ds. \tag{1.55}$$

Introducing the function

$$E(s,p) = \frac{1}{s}(\alpha_1 - \beta\alpha_2)A_1(s,p), \tag{1.56}$$

and in view of the first and third boundary conditions in (1.12), equation (1.52) and (1.54) yield the following pair of dual integral equations for the determination of the function $E(s,p)$

$$\int_0^\infty s\ F(s,p)\ E(s,p)\sin(sx)ds = \frac{\sigma(x)}{\mu_{12}\xi p} \qquad 0<x<1, \tag{1.57}$$

$$\int_0^\infty E(s,p)\sin(sx)ds = 0 \qquad x>1. \tag{1.58}$$

Following the procedure given by Sneddon (1966), the function $E(s,p)$ of the original integral equations (1.58) and (1.57) can be found in terms of another unknown function, $\Psi(r,p)$, in the form

$$E(s,p) = \frac{q}{\pi a\mu_{12}\xi p}\int_0^1 w^{1/2}\Psi(w,p)J_1(sw)dw. \tag{1.59}$$

where $\Psi(r,p)$ satisfies the following Fredholm integral equation

$$\Psi(r,p) + \int_0^1 \Psi(u,p)M(r,u,p)du = R(r), \tag{1.60}$$

with symmetrical kernel

$$M(r,u,p) = (ru)^{1/2} \int_0^\infty w\Big[F(w,p) - 1\Big] J_1(rw) J_1(uw) dw, \tag{1.61}$$

and free term

$$R(r) = \frac{2a}{\sqrt{r}q} \int_0^r \frac{\sigma(w)}{\sqrt{r^2 - w^2}} dw. \tag{1.62}$$

For the case of concentrated loads of magnitude q, we have $\sigma(x) = \frac{q}{a}\delta(x - x_0)$, such that the free term becomes

$$R(r) = \begin{cases} \frac{2x_0}{\sqrt{r}\sqrt{r^2 - x_0^2}} & \text{for} \quad x_0 < r \\ 0 & \text{for} \quad x_0 > r \end{cases} \tag{1.63}$$

Integrating $E(s,p)$ by parts, equation (1.59), gives

$$E(s,p) = -\frac{q}{\pi a \mu_{12} \xi p s} \left\{ \Psi(1,p) J_0(s) - \int_0^1 J_0(sw) \frac{d}{dw} \left[w^{1/2} \Psi(w,p) \right] dw \right\}. \tag{1.64}$$

From equation (1.54) we know that in the Laplace transform domain σ^*_{yy} is

$$\sigma^*_{yy}(x,0,p) = -\mu_{12}\xi \int_0^\infty s\ F(s,p)\ E(s,p) \sin(sx) ds.$$

and inserting (1.64) it is found that

$$\begin{aligned} \sigma^*_{yy}(x,0,p) \ &= \ \frac{q}{\pi a} \left[\frac{\Psi(1,p)}{p} \int_0^\infty F(s,p) J_0(s) \sin(sx) ds \right] \\ &\quad - \frac{q}{\pi a p} \left\{ \int_0^\infty F(s,p) \sin(sx) ds \int_0^1 J_0(sw) \frac{d}{dw} \left[w^{1/2} \Psi(w,p) \right] dw \right\}. \end{aligned} \tag{1.65}$$

and the stress intensity factor extracted from (1.65) for a load of magnitude $q/2$ is

$$K_{Ia}(t) = \frac{q}{2\sqrt{\pi a}} \mathcal{L}^{-1} \left\{ \frac{\Psi(1,p)}{p} \right\}, \tag{1.66}$$

Therefore the stress intensity factor of the original problem (figure 1.2(a)) in the time domain is given by the sum of the symmetric contribution (1.44) and the antisymmetric part (1.66), that is

$$\begin{aligned} K_I(t) \ &= \ K_{Is}(t) + K_{Ia}(t) \\ K_I(t) \ &= \ \frac{q}{\sqrt{\pi a}} \mathcal{L}^{-1} \left\{ \frac{\Phi(1,p) + \Psi(1,p)}{2p} \right\}. \end{aligned} \tag{1.67}$$

1.5 Numerical Results

The Fredholm integral equation, (1.37), was solved numerically using the Nystrom method (Atkinson 1997) to find $\Phi(r,p)$. The values of $\Phi(1,p)$ were then extracted. This method requires the application of an approximate quadrature rule to the Fredholm integral equation (1.37) and then the evaluation of the resulting equation at the quadrature points r_i to get

$$\Phi(r_i,p) + \sum_{j=1}^{N} w_j L(r_i,u_j,p)\Phi(u_i,p) = H(r_i) \tag{1.68}$$

where w_j are the weights of the quadrature rule, while the N points r_i are the abscissas. This is a set of N linear algebraic equations in N unknowns. For this problem $N = 200$ quadrature points were selected in order to get good accuracy and the trapezoidal quadrature rule was chosen because of the complex behavior of Φ and the discontinuous nature of the free term H.

Numerical inversion of the Laplace transform was performed using inverse fast Fourier transform to find $K_I(t)$ according to equation (1.43). From the definition of the Laplace transform (1.9) it is seen (Papoulis 1962) that to every function $f(t)$, a real constant γ can be associated such that $f^*(p)$ converges for $\mathrm{Re}(p) > \gamma$, with p considered a complex variable. Thus the region of existence of (1.9) is the half plane to the right of the vertical line $\mathrm{Re}(p) = \gamma$. If the region of convergence of $f^*(p)$ contains the iw axis in its interior, i.e., if $\gamma < 0$, then the Fourier transform

$$F(w) = \int_0^\infty e^{-iwt} f(t)\, dt$$

is a special case of the Laplace transform (1.9) with $p = iw$, thus $F(w)$ is given by

$$F(w) = f^*(iw).$$

At this point the fast Fourier transform algorithm may be used to find $f(t)$. In equation (1.43) we remove the singularity at $p = 0$ performing the Laplace transform inversion

$$K_I(t)' = \frac{q}{\sqrt{\pi a}} \mathcal{L}^{-1}\left\{ \frac{\Phi(1,p) - K(\infty)\frac{\sqrt{\pi a}}{q}}{p} \right\} \tag{1.69}$$

	Orthotropic material	Isotropic material
E_1 (GPa)	156.75	200
E_2 (GPa)	10.41	199.8
ν_{12}	0.31	0.3
ν_{23}	0.49	0.3
μ_{12} (GPa)	7.07	76.92
ρ (Kg/m^3)	1580	7840

Table 1.1: Mechanical properties used for the analysis.

such that the Laplace transform exists for $\gamma < 0$ and we can relate it with the Fourier transform. Then we find $K_I(t) = K_I(t)' + K_I(\infty)$. Equation (1.69) comes from the final value theorem for the Laplace transform (Debnath 1995) which states that if $K_I(t)$ is given by (1.43) then

$$K_I(\infty) = \lim_{t\to\infty} K_I(t) = \lim_{p\to 0} \frac{q}{\sqrt{\pi a}}\Phi(1,p).$$

The numerical results presented correspond to isotropic and orthotropic cases. Properties of transversely isotropic materials (a typical graphite-epoxy composite) with fibers parallel and perpendicular to the x axis are considered in the second case. These properties are given in table 1.1.

Figure 1.3 shows the stress intensity factor history for short and long times for an isotropic material in plane stress with concentrated loads located at $x_o = 0.6$. Note that the isotropic material is a degenerate case of the governing equations (1.3) and (1.4). For the isotropic material $c_{11} = c_{22} = \frac{2}{1-\nu}$ and $c_{12} = \frac{2\nu}{1-\nu}$. Hence $\gamma_1 = \gamma_2$ for $p = 0$ leading to $\beta = 1$ and $F(s,p)$ not defined. Consequently, the isotropic case presented here was obtained from the orthotropic formulation letting $E_1 = E, E_2 = (1-\epsilon)E, \nu_{12} = \nu_{23} = \nu$ and $\mu_{12} = (E_1 + E_2)/(4(1+\nu))$ where E and ν correspond to the isotropic properties and ϵ is a small quantity with $\epsilon << 1$. In figure 1.3(a) where the stress intensity factor for short times is displayed, good comparison with the solution given by Freund (1974) for one semi-infinite crack with line loads is seen. For normalized times $t \leq c_s(1+x_0)/c_d(1-x_0) = 2.13$ the finite crack problem has the same dynamic stress intensity factor as that of semi-infinite crack

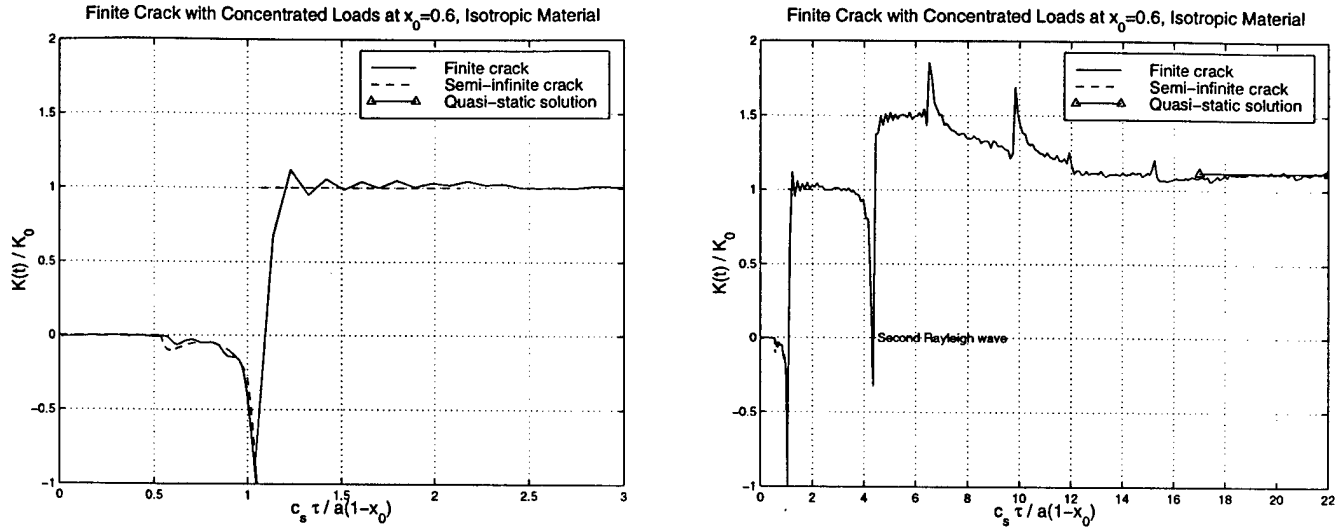

Figure 1.3: Stress intensity factor history for a finite crack with two pairs of concentrated loads in isotropic material. The normalization factor is $K_0 = q\sqrt{2/\pi a(1-x_0)}$. (a) Comparison of results for short times with Freund's (1974) exact solution for a semi-infinite crack in isotropic material. (b) For long times.

problem because the dilatational wave generated by the loads located at $x = -x_0$ has not arrived at the crack tip under consideration at $x = +1$ (see figure 1.1). The results shown in the figure 1.3(a) reflect this agreement. Note that the stress intensity factor is indeed discontinuous and that the numerical inversion technique captures the discontinuity quite well. It is worth noting that the presence of the singularity of $K_I(t)$ when the Rayleigh wave arrives is also captured in the numerical results. The singularity in $K_I(t)$ at $t = 1.078$ is similar to that found in the surface displacements in the calculated solution of Lamb's problem, where a concentrated load is applied on a half-space (Achenbach 1973).

The oscillations observed near the discontinuity in $K_I(t)$ are due to the convergence of the method employed to invert the Laplace transform. These oscillations are quite similar to Gibb's phenomenon as seen in the Fourier transform or Fourier series representation of a discontinuous function (Papoulis 1962).

After the arrival of the dilatational wave generated by the load at $x = -x_0$ the exact solution given by Freund is no longer valid. However, as seen in figure 1.3(b) the numerical

solution shows no appreciable change in $K_I(t)$ until the Rayleigh wave generated by the load at $x = -x_0$ arrives. At this time another discontinuity in $K_I(t)$ similar to that observed when the first Rayleigh wave arrived is observed. After that, several singularities are seen due to Rayleigh waves reflected from the crack tips. Eventually, these reflections die out and at $t = 15$, $K_I(t)$ reaches the quasi-static value given in equation (1.1). Disregarding the singularities, a dynamic overshoot of 36% is seen.

The results for $x_0 \neq 0.6$ are quite similar. However, if x_0 is very close to 1, then numerical difficulties arise in the solution of the Fredholm equation. Due the discontinuity in the free term $H(r)$ in (1.40), the discrete representation $H(r_i)$ in equation (1.68) would be a vector with almost only zeros for $x_0 \to 1^-$. Consequently, more quadrature points are needed.

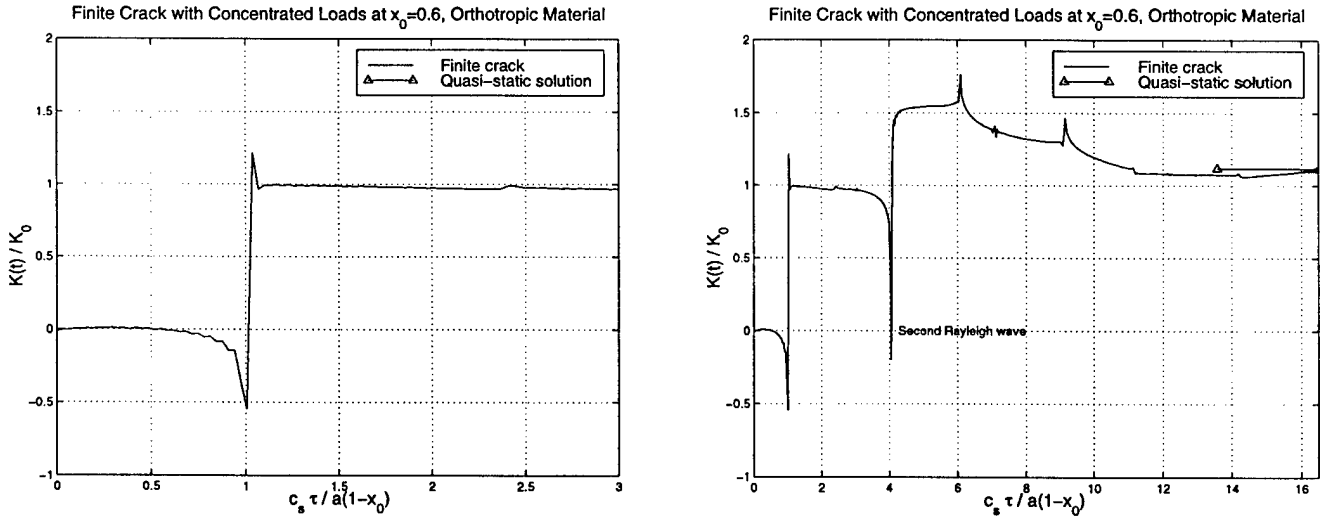

Figure 1.4: Stress intensity factor history for a finite crack with two pairs of concentrated loads in orthotropic material. The normalization factor is $K_0 = q\sqrt{2/\pi a(1-x_0)}$. The material properties correspond to a graphite-epoxy composite with the fibers parallel to the x axis. (a) For short times. (b) For long times.

Figure 1.4 shows the result for the orthotropic material in plane stress with concentrated loads also at $x_0 = 0.6$. Similar behavior to that shown in figure 1.3 for an isotropic material is seen. That is, $K_I(t)$ is initialy zero until the arrival of the dilatational wave. Then it becomes slightly negative before a singularity and a sudden discontinuous change is observed when

the Rayleigh wave arrives at the crack tip. It is also observed that another discontinuity occurs when the Rayleigh wave caused by the line loads at $x = -x_0$ arrives at the crack tip, the second Rayleigh wave results in another singularity and jump in $K_I(t)$. For long times the stress intensity factor reaches the quasi-static value as expected. The results shown in figure 1.4 correspond to a graphite-epoxy composite with mechanical properties shown in table 1.1. Figure 1.4 shows $K_I(t)$ for the case when the fibers are oriented parallel to the x axis. For wave propagation along the material principal axes wave pure modes are obtained (Nayfeh 1995), i.e., the polarization vector is directed either along or normal to the propagation direction. For wave propagation along the x axis of the composite mentioned above, the speed of the dilatational and shear waves are $c_d = 10,086\text{m/s}$ and $c_s = 2,115\text{m/s}$, respectively. Surface or Rayleigh waves in this case are found to propagate at a velocity of $c_R = 2090\text{m/s}$ (Nayfeh 1995).

For isotropic materials, $K_I(t)$ has a singularity at the time when the Rayleigh wave arrives, figure 1.3, this occurs between t=1 and t=1.078 for the properties shown in table 1.1; these normalized times correspond to the arrival of the shear and Rayleigh waves respectively. In figure 1.4, the orthotropic case, the arrival times are t=1 and t=1.012, that is, the singularity occurs in a shorter time interval, but even in this case the numerical solution is capable of predicting the singularity. It has been shown (Kraut 1963) that in the Lamb's problem for transversely isotropic materials there is also a singularity in the vertical displacements. Hence, a singularity in $K_I(t)$ is expected. Note that the numerical solution also predicts reflected pulses, i.e., the two peaks observed at t=6.06 and t=9.1 in figure 1.4(b), corresponding to the arrival at $x = +1$ of Rayleigh waves reflected by the tip $x = -1$.

Figure 1.5 illustrates the dynamic stress intensity factor $K_I(t)$ for the same composite material in plane stress with fibers parallel to y axis. A similar behavior is observed with respect to that of figure 1.4 where the composite has fibers parallel to x axis. In fact all three figures are quite similar. The magnitude of the jumps in the stress intensity factor are independent of the material constants c_{11}, c_{12} and c_{22}, as expected. Furthermore, since

dilatational waves have little effect on $K_I(t)$, the ratio of the Rayleigh wave speed to the shear wave speed, c_R/c_s, determines most of the behavior of $K_I(t)$ including the time of the singularities and jumps. This explains why the plots in figures 1.3, 1.4 and 1.5 are so similar even though they correspond to very different materials. Each has a very similar c_R/c_s ratio. In fact this ratio does not change dramatically for a wide range of materials.

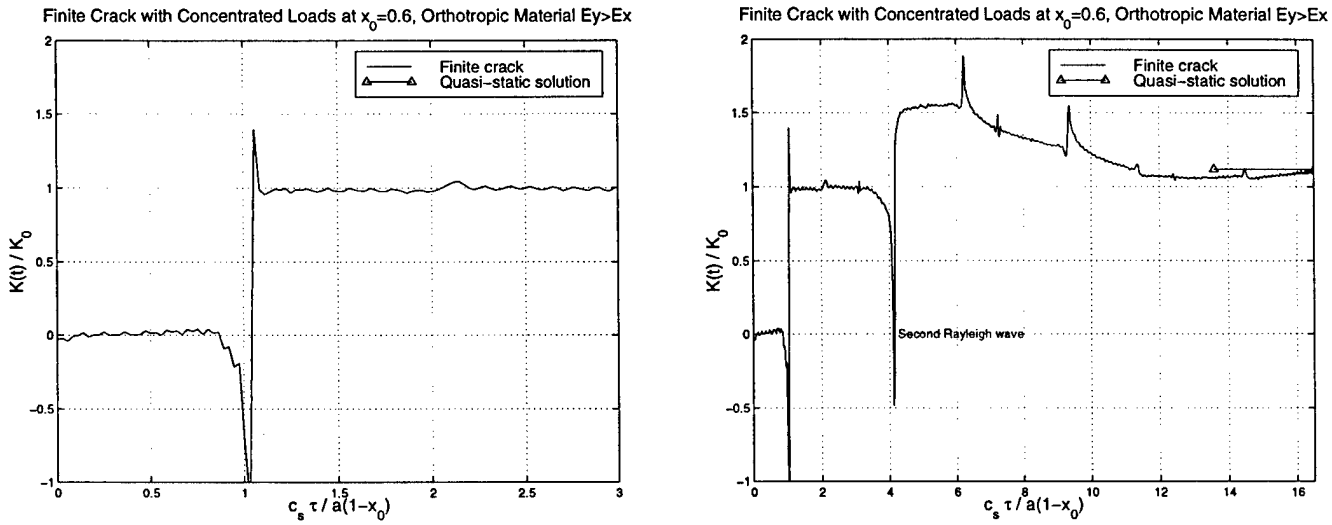

Figure 1.5: Stress intensity factor history for a finite crack with two pairs of concentrated loads in orthotropic material. The normalization factor is $K_0 = q\sqrt{2/\pi a(1-x_0)}$. The material properties correspond to a graphite-epoxy composite with the fibers perpendicular to the x axis. (a) For short times. (b) For long times.

1.5.1 Superposition problem

For the problem of a single pair of concentrated loads, figure 1.2(a), inversion of the Laplace transform was performed using inverse fast Fourier transform to find $K_I(t)$ according to equation (1.67). The function $\Psi(1,p)$ is evaluated numerically with the same procedure as $\Phi(1,p)$ of the first problem. The numerical results presented correspond to the orthotropic case. Properties of transversely isotropic materials with fibers parallel and perpendicular to the x axis, table 1.1, are considered. Figure 1.6 shows the results. The arrival at $x = +1$ of the Rayleigh wave causes a singularity and a jump in $K_I(t)$. Thereafter the plateau is maintained until the reflected Rayleigh wave from the tip $x = -1$ arrives at the tip $x = +1$.

The later behavior is a relatively smooth decreasing of $K_I(t)$ to reach the quasi-static value in equation (1.2). The dynamic overshoot is minimal at 5%.

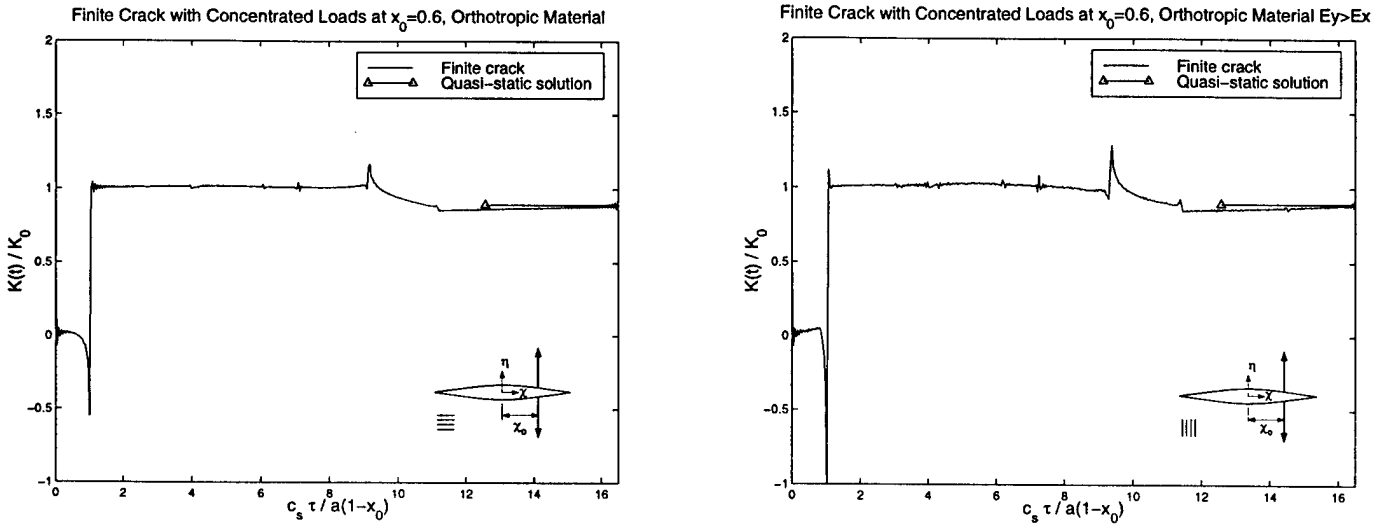

(a) (b)

Figure 1.6: Stress intensity factor history at $x = +1$ for a finite crack with a single pair of concentrated loads in orthotropic material, a) fibers parallel to $x-$axis, b) fibers parallel to $y-$axis.

1.6 Conclusions

The stress intensity factor history $K_I(t)$ has been determined for finite cracks in orthotropic materials subjected to impact concentrated loads. The singularities and discontinuities associated with the arrivals of stress waves have been predicted in the solution. The dynamic response of the crack has been analyzed until $K_I(t)$ reaches the quasi-static value. The limiting isotropic case in the orthotropic formulation agrees well with the exact solution available for isotropic material within that solution's period of validity. The overall time evolution of $K_I(t)$ is similar in isotropic and orthotropic materials. In fact, figures 1.3, 1.4 and 1.5 are very similar. This is due to several effects:

1. The values of $K_I(t)$ at the plateaus are independent of c_{11}, c_{22} and c_{12}.

2. Crack face displacements due to c_d are small and have little effect on the results.

3. The ratio of the Rayleigh wave speed to the shear wave speed varies little for each case, $c_R/c_s = 0.925$ for the isotropic and $c_R/c_s = 0.988$ for the orthotropic materials analyzed. Consequently, the singularities and jumps in $K_I(t)$ occur at similar normalized times. Many composite materials have c_R/c_s very near 1. Hence it is not expected that $K_I(t)$ would change for most other materials.

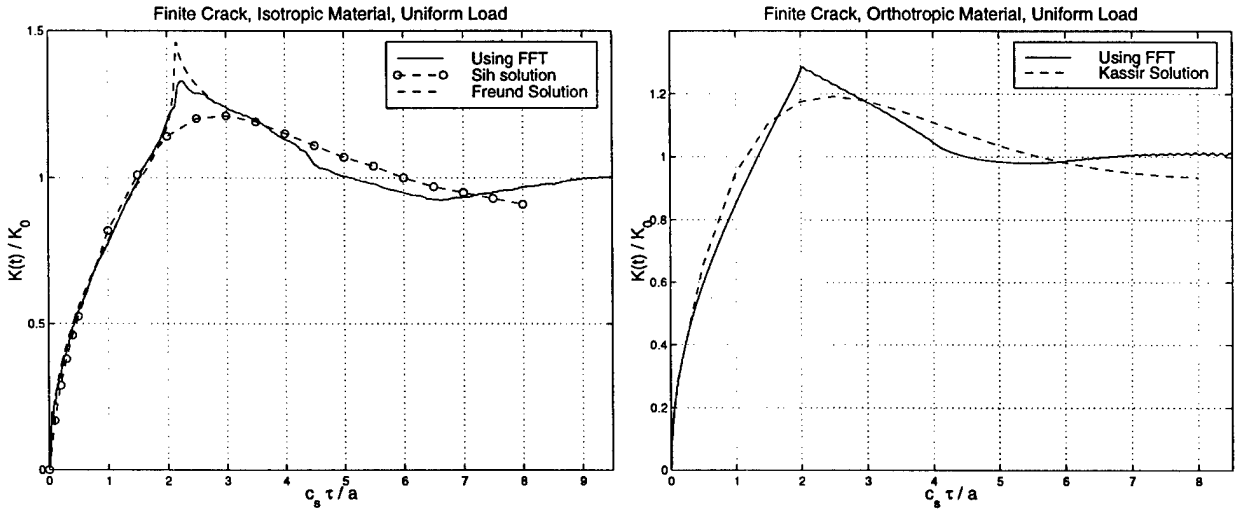

(a) (b)

Figure 1.7: Finite crack with uniform impact load, comparison of results. (a)Isotropic material, Freund's solution is exact. (b) Orthotropic material. The normalization factor is $K_0 = \sigma_0\sqrt{\pi a}$.

Several other problems have been solved in the literature using integral transform methods as mentioned in the introduction, however it seems from those studies that the accuracy of the method was weak. With the appropriate numerical methods to solve the Fredholm integral equation and to perform the Laplace inversion, it has been shown here that excellent results may be found. Figure 1.7 shows the stress intensity factor for a finite crack with uniform impact load in isotropic and orthotropic materials respectively. These problems were solved for the isotropic case by Chen and Sih (1979) using the method used here and by Freund (1990) using a superposition of solutions and the Weiner-Hopf Technique, and for the orthotropic case by Kassir and Bandyopadhyay (1983) using the method used here. The figure shows their results and those obtained using the FFT algorithm for the Laplace inver-

sion. Note that in the isotropic case, figure 1.7(a), a better approximation may be obtained using the FFT for the Laplace inversion as compared with Freund's solution which is exact for $t \leq 4c_s/c_d$. In the orthotropic case, figure 1.7(b), although there is no exact solution, we know that there should be a peak when a Rayleigh wave arrives from tip $x = -1$ at tip $x = +1$ and this behavior is well described in our solution. The dynamic overshoot in 1.7(b) is larger, 30% vs. 20%. In both cases, after reaching the maximum, the stress intensity factor decays to the quasi-static value without many oscillations as was previously claimed (Chen and Sih 1977).

Chapter 2

Response of Finite Cracks in Orthotropic Materials due to Concentrated Impact Shear Loads

Co-authored with C. Rubio-Gonzalez and submitted to ASME Journal of Applied Mechanics

Abstract

The elastodynamic response of an infinite orthotropic material with a finite crack under concentrated in-plane shear loads is examined. Solution for the stress intensity factor history around the crack tips is found. Laplace and Fourier transforms are employed to solve the equations of motion leading to a Fredholm integral equation on the Laplace transform domain. The dynamic stress intensity factor history can be computed by numerical Laplace transform inversion of the solution of the Fredholm equation. Numerical values of the dynamic stress intensity factor history for several example materials are obtained. The results differ from mode I in that there is heavy dependence upon the material constants. This solution can be used as a Green's function to solve dynamic problems involving finite cracks and in-plane shear loading.

2.1 Introduction

The use of composite materials is becoming more common in many engineering applications. The dynamic behavior of cracked bodies in such materials is a subject of many theoretical and experimental works. Both stationary and propagating cracks under dynamic loads in isotropic materials have been analyzed extensively (Freund 1990, Parton and Boriskovsky 1989, Chen and Sih 1977). However, for orthotropic materials the available solutions are few (Kassir and Bandyopadhyay 1983, Shindo and Nozaki 1991, Rubio-Gonzalez and Mason 1998), this is due in part, to the mathematical complexity of such problems. Recently Rubio-Gonzalez and Mason (1998) presented the solution for a finite crack in orthotropic materials subjected to concentrated impact loads in mode I. Their solution was able to predict the singularities and discontinuities in the stress intensity factor history associated with the arrival of shear, dilatational and Rayleigh stress waves at the crack tips. One conclusion of that work is that crack face displacements due to the dilatational wave are small and have little effect on the results. Thus the ratio of the Rayleigh wave speed to the shear wave speed, c_R/c_s, determines most of the behavior of $K_I(t)$ including the time of the singularities and jumps in this function. However, as will be seen here, the behavior for in-plane shear loading is very different. The arrival of the dilatational wave at the crack tip causes a jump in $K_{II}(t)$ which is significant in the overall shape of the stress intensity factor history, especially for fiber-reinforced composites with fibers aligned with the plane of the crack.

Shear loading of cracks in composite systems is drawing the attention of investigators as an important factor in dynamic failure of composites and debonding of bimaterials. The theoretical analysis of Liu, et al. (1995) predicts that the near-tip deformation field for transonic interfacial crack growth is predominantly of a shear nature. Experimental observations of Lambros and Rosakis (1995) and Shukla et al. (1998) support that prediction. Lambros and Rosakis (1995) were able to measure cracks propagating at 1.5 times the lower Rayleigh wave speed of the constituents in a bimaterial plate. More recent work by Rosakis and co-workers (1998) has demonstrated that shear loaded stationary cracks in unidirectional

composites can accelerate to supersonic speeds, speeds above the Rayleigh wave speed for that material and orientation. Finally in quasi-static tests, shear dominated loading can often lead to unstable crack growth (Shivakumar and Crews 1998). Consequently, it seems that dynamic shear loading of cracks may be of primary importance in the impact failure of composites.

In the present work, the problem of an infinite orthotropic body with a finite crack subjected to suddenly applied shear line loads on its faces is examined. The crack lies on the principal axes of the material. The Green's function presented here, the solution related to the geometry shown schematically in Figure 2.1, has not been reported to date although the quasi-static solution is presented by Isida (1972) as

$$K_I(t=\infty) = \frac{q}{\sqrt{\pi a}}\left(\sqrt{\frac{a+\chi_0}{a-\chi_0}} + \sqrt{\frac{a-\chi_0}{a+\chi_0}}\right) \tag{2.1}$$

where χ_o, q and a are defined in the figure. The quasi-static solution for tangent opposite loads on a semi-infinite crack will be used as a normalization parameter in this study, however, and it is given by

$$K_0 = q\sqrt{\frac{2}{\pi(a-\chi_0)}}. \tag{2.2}$$

It is worth noting that, while the dynamic stress intensity factor for normal opposite line loads on a semi-infinite crack has been published for isotropic materials (Freund 1974), it appears that the dynamic stress intensity factor for tangent opposite line loads in semi-infinite cracks is not available. However, a solution for tangent line loads pointing *in the same direction* on semi-infinite cracks is given by Abou-Sayed et al (1980).

Integral transform methods are usually the techniques employed to solve problems involving cracked orthotropic bodies subjected to impact loads (Kassir and Bandyopadhyay 1983, Shindo and Nozaki 1991). This approach leads to a Fredholm integral equation on the Laplace transform domain, rather than a Weiner-Hopf equation (Freund 1990) as is found for isotropic materials. The dynamic stress intensity factor on the time domain is recovered, in the most difficult step of the analysis, by numerical inversion of the solution of the Fredholm equation. This process can be numerically challenging and computationally intensive.

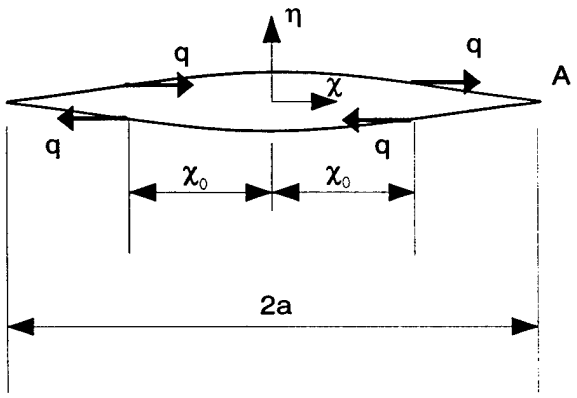

Figure 2.1: Schematic of the finite crack geometry with concentrated shear loads.

Rubio-Gonzalez and Mason (1998) have shown that with the appropriate numerical methods to solve the Fredholm integral equation and to perform the Laplace inversion, excellent results may be found in the solution of dynamic crack problems by integral transform methods. In this work the method of Honig and Hirdes (1984) is used for the inversion of the Laplace transform.

2.2 Governing Equations

Consider the plane problem of an infinite orthotropic medium containing a finite crack, Figure 2.1. Let E_i, μ_{ij} and ν_{ij} $(i,j = 1,2,3)$ be the engineering elastic constants of the material where the indices 1, 2, and 3 correspond to the directions (χ, η, z) of a system of Cartesian coordinates chosen to coincide with the axes of material orthotropy. The crack plane is $\eta = 0$ and the origin of the $\chi\eta$ axes is the mid-point of the distance between the crack tips. The normalized coordinates $x = \chi/a$ and $y = \eta/a$ are introduced such that the crack tips are located at $x = \pm 1$ and the loads at $x = \pm x_0$. The normalized time t is introduced in the form $t = c_s\tau/a$ where $c_s = \sqrt{\mu_{12}/\rho}$ with ρ being the mass density. Concentrated shear forces of magnitude q are applied as shown.

The problem under consideration is restricted to two dimensions with wave propagation in the $x - y$ plane only. By setting all the derivatives with respect to z to be zero, it is readily shown that the displacement equations of motion (Nayfeh 1995) in the normalized

coordinates reduce to

$$c_{11}\frac{\partial^2 u}{\partial x^2}+\frac{\partial^2 u}{\partial y^2}+(1+c_{12})\frac{\partial^2 v}{\partial x\partial y} = \frac{\partial^2 u}{\partial t^2}, \tag{2.3}$$

$$\frac{\partial^2 v}{\partial x^2}+c_{22}\frac{\partial^2 v}{\partial y^2}+(1+c_{12})\frac{\partial^2 u}{\partial x\partial y} = \frac{\partial^2 v}{\partial t^2}, \tag{2.4}$$

where u and v are the x and y components of the normalized displacement vector and c_{11}, c_{12} and c_{22} are non-dimensional parameters related to the elastic constants by the relations:

$$\begin{aligned} c_{11} &= \frac{E_1}{\mu_{12}[1-(E_2/E_1)\nu_{12}^2]}, \\ c_{22} &= (E_2/E_1)c_{11}, \\ c_{12} &= \nu_{12}c_{22}=\nu_{21}c_{11}, \end{aligned} \tag{2.5}$$

for generalized plane stress, and by

$$\begin{aligned} c_{11} &= \frac{E_1}{\mu_{12}\Delta}(1-\nu_{23}\nu_{32}), \\ c_{22} &= \frac{E_2}{\mu_{12}\Delta}(1-\nu_{13}\nu_{31}), \\ c_{12} &= \frac{E_1}{\mu_{12}\Delta}(\nu_{21}+\frac{E_2}{E_1}\nu_{13}\nu_{32}), \\ \Delta &= 1-\nu_{12}\nu_{21}-\nu_{23}\nu_{32}-\nu_{31}\nu_{13}-\nu_{12}\nu_{23}\nu_{31}-\nu_{13}\nu_{21}\nu_{32}, \end{aligned} \tag{2.6}$$

for plane strain. In the orthotropic solid, c_s represents the velocity of the in-plane shear wave propagating along the the principal material axes. The stresses are related to the displacements by the equations:

$$\begin{aligned} \frac{\sigma_x}{\mu_{12}} &= c_{11}\frac{\partial u}{\partial x}+c_{12}\frac{\partial v}{\partial y}, \\ \frac{\sigma_y}{\mu_{12}} &= c_{12}\frac{\partial u}{\partial x}+c_{22}\frac{\partial v}{\partial y}, \\ \frac{\tau_{xy}}{\mu_{12}} &= \frac{\partial u}{\partial y}+\frac{\partial v}{\partial x}. \end{aligned} \tag{2.7}$$

The corresponding boundary conditions are

$$\begin{aligned} \sigma_y(x,0,t) &= 0 \quad \text{for} \quad |x|<\infty, \\ \tau_{xy}(x,0,t) &= -\tau(x)H(t) \quad \text{for} \quad |x|<1, \\ u(x,0,t) &= 0 \quad \text{for} \quad |x|>1, \end{aligned} \tag{2.8}$$

in addition to the condition of zero displacements at infinity and zero initial conditions. The traction $\tau(x)$ is a known function of x and $H(t)$ is the Heaviside step function.

Equations (2.3), (2.4) and (2.8) constitute a mathematical statement of the problem. For the moment $\tau(x)$ represents a general load on the crack faces, later it will be substituted by a function representing the line loads.

2.3 Method of Solution

The method of solution of the governing equations presented here follows that of Kassir and Bandyopadhyay (1983) and Sneddon (1966). In equations (2.3) and (2.4), the time variable may be removed by application of the Laplace transform

$$f^*(p) = \int_0^\infty f(t)\, e^{-pt}\, dt, \quad f(t) = \frac{1}{2\pi i}\int_{Br} f^*(p)\, e^{pt}\, dt, \tag{2.9}$$

where Br denotes the Bromwich path of integration which is a line parallel to the imaginary axis in the p-plane. Applying relations (2.9) to equations (2.3) and (2.4) and assuming zero initial conditions for the displacements and velocities, the transformed field equations become

$$c_{11}\frac{\partial^2 u^*}{\partial x^2} + \frac{\partial^2 u^*}{\partial y^2} + (1+c_{12})\frac{\partial^2 v^*}{\partial x \partial y} - p^2 u^* = 0, \tag{2.10}$$

$$\frac{\partial^2 v^*}{\partial x^2} + c_{22}\frac{\partial^2 v^*}{\partial y^2} + (1+c_{12})\frac{\partial^2 u^*}{\partial x \partial y} - p^2 v^* = 0, \tag{2.11}$$

where the transformed displacement components, u^* and v^*, are now functions of the variables x, y, and p. The application of the Laplace transform to the boundary conditions (2.8) gives

$$\begin{aligned} \sigma_y^*(x,0,t) &= 0 \quad \text{for} \quad |x| < \infty, \\ \tau_{xy}^*(x,0,t) &= -\tau(x)/p \quad \text{for} \quad 0 < |x| < 1, \\ u^*(x,0,t) &= 0 \quad \text{for} \quad |x| > 1. \end{aligned} \tag{2.12}$$

To obtain a solution of the differential equations (2.10) and (2.11) subject to conditions (2.12), we exploit the symmetry of the problem by letting

$$u^*(x,y,p) = \int_0^\infty A(s,y,p)\cos(sx)ds, \tag{2.13}$$

$$v^*(x,y,p) = -\int_0^\infty B(s,y,p)\sin(sx)ds, \tag{2.14}$$

where A and B are the Fourier cosine and sine transforms of the Laplace transform of the displacements, u^* and v^*, respectively, and are yet to be determined. Substituting these transforms into equations (2.10) and (2.11), the functions A and B are found to satisfy the simultaneous ordinary differential equations

$$(c_{11}s^2+p^2)A - \frac{d^2A}{dy^2} + (1+c_{12})s\frac{dB}{dy} = 0, \tag{2.15}$$

$$(s^2+p^2)B - c_{22}\frac{d^2B}{dy^2} - (1+c_{12})s\frac{dA}{dy} = 0. \tag{2.16}$$

The solution of these equations which vanishes for $|y| \to \infty$ is

$$\begin{aligned} A(s,y,p) &= A_1(s,p)e^{-\gamma_1 y} + A_2(s,p)e^{-\gamma_2 y}, \\ B(s,y,p) &= \frac{\alpha_1}{s}A_1(s,p)e^{-\gamma_1 y} + \frac{\alpha_2}{s}A_2(s,p)e^{-\gamma_2 y}, \end{aligned} \tag{2.17}$$

where A_1 and A_2 are arbitrary functions and $\alpha_j(s,p)$ stands for the functions

$$\alpha_j(s,p) = \frac{c_{11}s^2+p^2-\gamma_j^2}{(1+c_{12})\gamma_j}, \quad j=1,2 \tag{2.18}$$

with γ_1^2 and γ_2^2 being two distinct roots of the quadratic equation

$$c_{22}\gamma^4 + [(c_{12}^2+2c_{12}-c_{11}c_{22})s^2 - (1+c_{22})p^2]\gamma^2 + (c_{11}s^2+p^2)(s^2+p^2) = 0. \tag{2.19}$$

It can be shown that for many materials the roots γ_1 and γ_2 are real and positive and the expressions for the displacements in the Laplace transform domain become:

$$u^* = \int_0^\infty (A_1e^{-\gamma_1 y} + A_2e^{-\gamma_2 y})\cos(sx)ds, \tag{2.20}$$

$$v^* = -\int_0^\infty (\alpha_1A_1e^{-\gamma_1 y} + \alpha_2A_2e^{-\gamma_2 y})\frac{\sin(sx)}{s}ds, \tag{2.21}$$

and using (2.7) the corresponding expression for σ_y^* is given by

$$\sigma_y^* = -\mu_{12}\int_0^\infty [(c_{12}s^2 - \alpha_1\gamma_1 c_{22})A_1 e^{-\gamma_1 y} + (c_{12}s^2 - \alpha_2\gamma_2 c_{22})A_2 e^{-\gamma_2 y}]\frac{\sin(sx)}{s}ds. \tag{2.22}$$

Applying the first condition of (2.12) to equation (2.22) yields

$$\begin{aligned} A_2(s,p) &= -\beta A_1(s,p), \\ \beta &= \frac{c_{12}s^2 - c_{22}\alpha_1\gamma_1}{c_{12}s^2 - c_{22}\alpha_2\gamma_2}. \end{aligned} \tag{2.23}$$

Therefore the expressions for the transformed components of displacement become

$$u^*(x,y,p) = \int_0^\infty (e^{-\gamma_1 y} - \beta e^{-\gamma_2 y})A_1(s,p)\cos(sx)ds, \tag{2.24}$$

$$v^*(x,y,p) = -\int_0^\infty (\alpha_1 e^{-\gamma_1 y} - \beta\alpha_2 e^{-\gamma_2 y})\frac{A_1(s,p)}{s}\sin(sx)ds, \tag{2.25}$$

and the associated stress components are given by

$$\sigma_x^* = -\mu_{12}\int_0^\infty [(c_{11}s^2 - \alpha_1\gamma_1 c_{12})e^{-\gamma_1 y} - (c_{11}s^2 - \alpha_2\gamma_2 c_{12})\beta e^{-\gamma_2 y}]\frac{A_1(s,p)}{s}\sin(sx)ds, \tag{2.26}$$

$$\sigma_y^* = -\mu_{12}\int_0^\infty (c_{12}s^2 - \alpha_1\gamma_1 c_{22})(e^{-\gamma_1 y} - e^{-\gamma_2 y})\frac{A_1(s,p)}{s}\sin(sx)ds, \tag{2.27}$$

$$\tau_{xy}^* = \mu_{12}\int_0^\infty [-(\alpha_1+\gamma_1)e^{-\gamma_1 y} + \beta(\alpha_2+\gamma_2)e^{-\gamma_2 y}]A_1(s,p)\cos(sx)ds. \tag{2.28}$$

Introducing the functions

$$S(s,p) = (1-\beta)A_1(s,p), \tag{2.29}$$

$$G(s,p) = \frac{-(\alpha_1+\gamma_1) + \beta(\alpha_2+\gamma_2)}{s(1-\beta)\eta}, \tag{2.30}$$

$$\begin{aligned} \eta = {} & \frac{1}{c_{22}N_1N_2(1+c_{12})(N_1+N_2)}\{(c_{12}^2 + c_{12} - c_{11}c_{22})(c_{12}N_1N_2 - c_{11}) \\ & -c_{22}[c_{12}N_1^2N_2^2 + c_{11}(N_1^2 + N_1N_2 + N_2^2)]\}, \end{aligned} \tag{2.31}$$

$$N_{1,2}^2 = \frac{1}{2c_{22}}\{c_{11}c_{22} - c_{12}^2 - 2c_{12} \pm [(c_{11}c_{22} - c_{12}^2 - 2c_{12})^2 - 4c_{11}c_{22}]^{1/2}\}, \tag{2.32}$$

and in view of the second and third boundary conditions in (2.12), equation (2.24) and (2.28) yield the following pair of dual integral equations for the determination of the function $S(s,p)$

$$\int_0^\infty s\, G(s,p)\, S(s,p)\cos(sx)ds = -\frac{\tau(x)}{\mu_{12}\eta p} \qquad 0 < x < 1, \tag{2.33}$$

$$\int_0^\infty S(s,p)\cos(sx)ds = 0 \qquad x > 1, \tag{2.34}$$

where $\tau(x)$ is the distributed load along the crack faces. The constant η in (2.30) has been chosen such that for large s, the function $G(s,p)$ becomes

$$G(s,p) = 1 + O(1/s)$$

Using $\cos(sx) = \sqrt{\frac{sx\pi}{2}} J_{-1/2}(sx)$ and defining $\bar{S}(s,p) = s^{1/2} S(s,p)$ and $r_1(s,p) = G(s,p) - 1$, these last equations can be written as

$$\begin{aligned} \int_0^\infty s[r_1(s,p)+1]\bar{S}(s,p) J_{-1/2}(sx) ds &= g(x) \qquad 0 < x < 1, \\ \int_0^\infty \bar{S}(s,p) J_{-1/2}(sx) ds &= 0 \qquad x > 1, \end{aligned}$$

where

$$g(x) = -\sqrt{\frac{2}{\pi x}} \frac{\tau(x)}{\mu_{12}\eta p}. \tag{2.35}$$

Following the procedure given by Sneddon (1966), the function $S(s,p)$ of the original integral equations (2.34) and (2.33) can be found in terms of another unknown function, $\Theta(r,p)$, in the form

$$S(s,p) = -\frac{q}{\pi a \mu_{12} \eta p} \int_0^1 w^{1/2} \Theta(w,p) J_0(sw) dw. \tag{2.36}$$

where $\Theta(r,p)$ satisfies the following Fredholm integral equation

$$\Theta(r,p) + \int_0^1 \Theta(u,p) K(r,u,p) du = H(r), \tag{2.37}$$

with symmetrical kernel

$$K(r,u,p) = (ru)^{1/2} \int_0^\infty w\Big[G(w,p) - 1\Big] J_0(rw) J_0(uw) dw, \tag{2.38}$$

and free term

$$H(r) = \frac{2a\sqrt{r}}{q} \int_0^r \frac{\tau(w)}{\sqrt{r^2 - w^2}} dw. \tag{2.39}$$

For the case of concentrated loads as illustrated in figure 2.1, we have $\tau(x) = \frac{q}{a}\delta(x - x_0)$ where the denominator appears due to the normalization of x, such that the free term becomes

$$H(r) = \begin{cases} \frac{2\sqrt{r}}{\sqrt{r^2 - x_0^2}} & \text{for} \quad x_0 < r \\ 0 & \text{for} \quad x_0 > r. \end{cases} \tag{2.40}$$

Note that the free term is discontinuous in r. Integrating $S(s,p)$ by parts in equation (2.36), gives

$$S(s,p) = -\frac{q}{\pi a \mu_{12} \eta p s}\left\{\Theta(1,p)J_1(s) - \int_0^1 wJ_1(sw)\frac{d}{dw}\left[w^{-1/2}\Theta(w,p)\right]dw\right\}. \qquad (2.41)$$

From equation (2.28) we know that in the Laplace transform domain τ^*_{xy} is

$$\tau^*_{xy}(x,0,p) = \mu_{12}\eta \int_0^\infty s\, G(s,p)\, S(s,p)\cos(sx)ds.$$

and substituting (2.41) it is found that

$$\begin{aligned}\tau^*_{xy}(x,0,p) &= -\frac{q}{\pi a}\left[\frac{\Theta(1,p)}{p}\int_0^\infty G(s,p)J_1(s)\cos(sx)ds\right] \\ &\quad -\frac{q}{\pi a p}\left\{\int_0^\infty G(s,p)\cos(sx)ds \int_0^1 wJ_1(sw)\frac{d}{dw}\left[w^{-1/2}\Theta(w,p)\right]dw\right\} \qquad (2.42)\end{aligned}$$

As stated by Kassir and Bandyopadhyay (1983) the stress intensity factor extracted from (2.42) is

$$K_{II}(t) = \frac{q}{\sqrt{\pi a}}\,\mathcal{L}^{-1}\left\{\frac{\Theta(1,p)}{p}\right\}, \qquad (2.43)$$

where $\mathcal{L}^{-1}$ denotes the inverse of the Laplace transform.

2.4 Numerical Results

2.4.1 Quasi-static solution

We can show that the dynamic formulation is consistent with the quasi-static solution; that is, we recover equation (2.1) exactly when $t \to \infty$. To do this we invoke the final value theorem for Laplace transforms, (Debnath 1995) which states that if $K_{II}(t)$ is given by (2.43) then

$$K_{II}(\infty) = \lim_{t\to\infty} K_{II}(t) = \lim_{p\to 0} \frac{q}{\sqrt{\pi a}}\Theta(1,p).$$

Noting that by construction $G(s,p) \to 1$ when $p \to 0$, therefore the kernel, equation (2.38), vanishes and equation (2.37) gives $\Theta(r,p) = H(r)$ for $p \to 0$, in particular $\Theta(1,p) = H(1)$,

and hence

$$K_{II}(\infty) = \frac{q}{\sqrt{\pi a}} \frac{2a}{\sqrt{a^2 - \chi_0^2}}.$$

which is exactly the expression (2.1). In the plots to follow, figures 2.2-2.5, it can be shown by careful numerical Laplace transform inversion that the results decay to the quasi-static solution as $t \to \infty$. For that reason interest is focused on the early time, transient response.

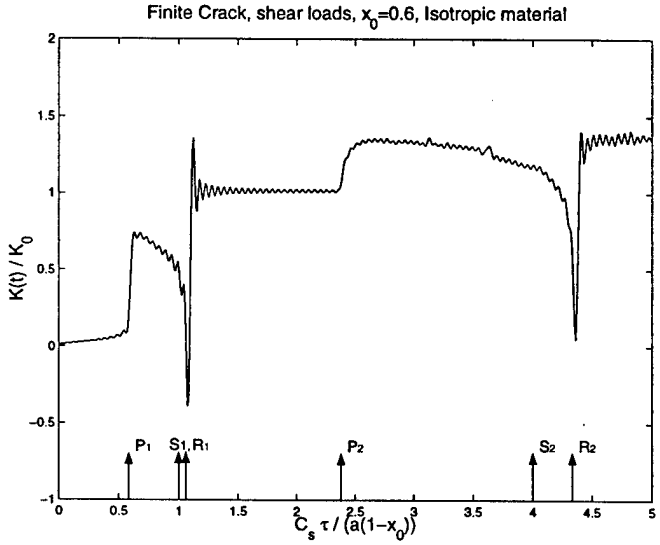

Figure 2.2: Stress intensity factor history for a finite crack with concentrated shear loads in isotropic material. The normalization factor is given by the equation (2.2). The labels P_1, S_1 and R_1 correspond to the arrival at the crack tip $x = +1$ of the dilatational, shear and Rayleigh waves at the crack tip $x = +1$ generated by the load at $x = +x_0$, respectively. Similarly, P_2, S_2 and R_2 correspond to the arrival of the dilatational, shear and Rayleigh waves at the crack tip $x = +1$ as generated by the load at $x = -x_0$.

2.4.2 Transient response

The Fredholm integral equation, (2.37), was solved numerically using the Nystrom method (Atkinson 1997) to find $\Theta(r, p)$. The values of $\Theta(1, p)$ were then extracted. This method requires the application of an approximate quadrature rule to the Fredholm integral equation (2.37) and then the evaluation of the resulting equation at the quadrature points r_i to get

$$\Theta(r_i, p) + \sum_{j=1}^{N} w_j K(r_i, u_j, p)\Theta(u_i, p) = H(r_i) \tag{2.44}$$

	Graphite Epoxy	E-Glass Epoxy	Boron Epoxy	Isotropic material
E_1 (GPa)	156.75	45	207	200
E_2 (GPa)	10.41	12	19	199.8
ν_{12}	0.31	0.19	0.21	0.3
ν_{23}	0.49	0.19	0.21	0.3
μ_{12} (GPa)	7.07	5.5	6.4	76.92
ρ (Kg/m^3)	1580	2100	1990	7840

Table 2.1: Mechanical properties used for the analysis.

where w_j are the weights of the quadrature rule, while the N points r_i are the abscissas. This is a set of N linear algebraic equations in N unknowns. For this problem $N = 200$ quadrature points were selected in order to get good accuracy and the trapezoidal quadrature rule was chosen because of the complex behavior of Θ and the discontinuous nature of the free term H.

Numerical inversion of the Laplace transform was performed using the method of Honig and Hirdes (1985) to find $K_{II}(t)$ according to equation (2.43). In this method the choice of the Bromwich path is made automatically using a straight-forward convergence criterion.

The numerical results presented correspond to isotropic and orthotropic cases. Properties of transversely isotropic materials with fibers parallel and perpendicular to the x axis are considered in the second case. The properties used are taken from Schwartz (1997) and are given in table 2.1.

Figure 2.2 shows the stress intensity factor history for an isotropic material in plane stress with concentrated loads located at $x_o = 0.6$. Note that the isotropic material is a degenerate case of the governing equations (2.3) and (2.4). For the isotropic material $c_{11} = c_{22} = \frac{2}{1-\nu}$ and $c_{12} = \frac{2\nu}{1-\nu}$. Hence $\gamma_1 = \gamma_2$ for $p = 0$ leading to $\beta = 1$ and $G(s,p)$ not defined. Consequently, the isotropic case presented here was obtained from the orthotropic formulation letting $E_1 = E, E_2 = (1-\epsilon)E, \nu_{12} = \nu_{23} = \nu$ and $\mu_{12} = (E_1 + E_2)/(4(1+\nu))$ where E and ν correspond to the isotropic properties and ϵ is a small quantity with $\epsilon << 1$. Note that the stress intensity factor is indeed discontinuous and that the numerical inversion

technique captures the discontinuity quite well. It is worth noting that the presence of the singularity of $K_{II}(t)$ when the Rayleigh wave arrives is also captured in the numerical results. The singularity in $K_{II}(t)$ at $t = 1.08$ (label R_1) is similar to that found in the surface displacements in the calculated solution of Lamb's problem, where a concentrated shear load is applied on a half-space (Chao 1960).

The stress intensity factor is zero until the arrival at the tip $x = +1$ at the normalized time $t = 0.59$ (label P_1) of the dilatational wave originated by the load at $x = x_0$; at this time a jump in $K_{II}(t)$ is observed. Before this time, a slight increase that is a numerical artifact is seen. Obviously the dilatational wave has an important effect in the dynamic response unlike in mode I loading where that wave had a minimum effect in $K_I(t)$ (Rubio-Gonzalez and Mason 1998). When the Rayleigh wave arrives, $K_{II}(t)$ experiences a singularity and a jump followed by a stable value given by equation (2.2). This cycle is repeated when a second dilatational wave arrives from the further point load at $t = 2.36$ (label P_2) but with decaying amplitude due to the increased distance between point load and crack tip.

The oscillations observed near the discontinuity in $K_{II}(t)$ are due to the convergence of the method employed to invert the Laplace transform. These oscillations are quite similar to Gibb's phenomenon as seen in the Fourier transform or Fourier series representation of a discontinuous function (Papoulis 1962).

The results for $x_0 \neq 0.6$ are very similar. However, if x_0 is very close to 1, then numerical difficulties arise in the solution of the Fredholm equation. Due the discontinuity in the free term $H(r)$ in (2.40), the discrete representation $H(r_i)$ in equation (2.44) becomes a vector with mostly zero components as $x_0 \to 1^-$. Consequently, more quadrature points are needed.

Figure 2.3 shows the results for the orthotropic material in plane stress with concentrated shear loads also at $x_0 = 0.6$. Figure 2.3(a) corresponds to the case of fibers parallel to the x-axis while 2.3(b) to fibers parallel to the y-axis. Note a clear difference in the behavior, this is due to the fact that c_d has an important effect in $K_{II}(t)$, and in this case the difference is more noticeable since c_d is quite different in each case, see table 2.2. Figure 2.3(b) is more similar

velocity (m/s)	Graphite Epoxy x	Graphite Epoxy y	Boron Epoxy x	E Glass Epoxy x	Isotropic material
c_d	10086	2974	10251	4685	5860
$c_d^{pl-\sigma}$	9992	2574	10219	4651	5294
c_s	2115	2115	1793	1618	3132
$c_R^{pl-\sigma}$	2083	2037	1783	1572	2869

Table 2.2: Wave speeds for the different materials. The composite materials are considered with fibers and wave propagation parallel to $x-$axis, except in Graphite-Epoxy y where wave propagation is considered along $y-$axis.

to figure 2.2, i.e. two separated cycles are observed, corresponding to the arrival of waves generated by the load at $x = +x_0$ and then the waves generated by the load at $x = -x_0$. This happens because $x_0/c_R < (1 + x_0)/c_d$. That is the Rayleigh wave from $+x_0$ arrives before the dilatational wave from $-x_0$. However, in figure 2.3(a) where $x_0/c_R > (1 + x_0)/c_d$ the dilatational waves caused by both loads arrive at the tip $x = +1$ before any other wave, thus their effects are added and as a result $K_{II}(t)$ reaches the maximum dynamic overshoot sooner. The three main jumps in figure 2.3(a) occur at $t = 0.21$ (arrival of the dilatational wave from $+x_0$, mark P_1), $t = 0.84$ (arrival of the dilatational wave from $-x_0$, mark P_2) and $t = 1.01$ (arrival of the Rayleigh wave from $+x_0$, mark R_1). Note that in figure 2.3(b) the numerical solution captures quite well the singularities and jumps when the Rayleigh waves arrive at $t = 1.03$ and $t = 4.15$, but for long times the solution shows rapid oscillations, this is due to the insufficient accuracy in the numerical Laplace inversion technique and can be remedied with more computational effort. Looking at figures 2.2 and 2.3(b) we note that the plateaus are independent of the elastic constants c_{11}, c_{12} and c_{22} as expected from equation (2.2). A small error is observed in figures 2.2 and 2.3 since the stress intensity factor should be zero until the dilatational wave arrives, and these figures show a value slightly different from zero. This is due to the approximate numerical methods used to solve the Fredholm integral equation and to invert the Laplace transform.

Figures 2.4 and 2.5 show the stress intensity factor $K_{II}(t)$ for boron-epoxy and E glass-epoxy composites respectively. In both cases the fibers are considered along the x-axis. For

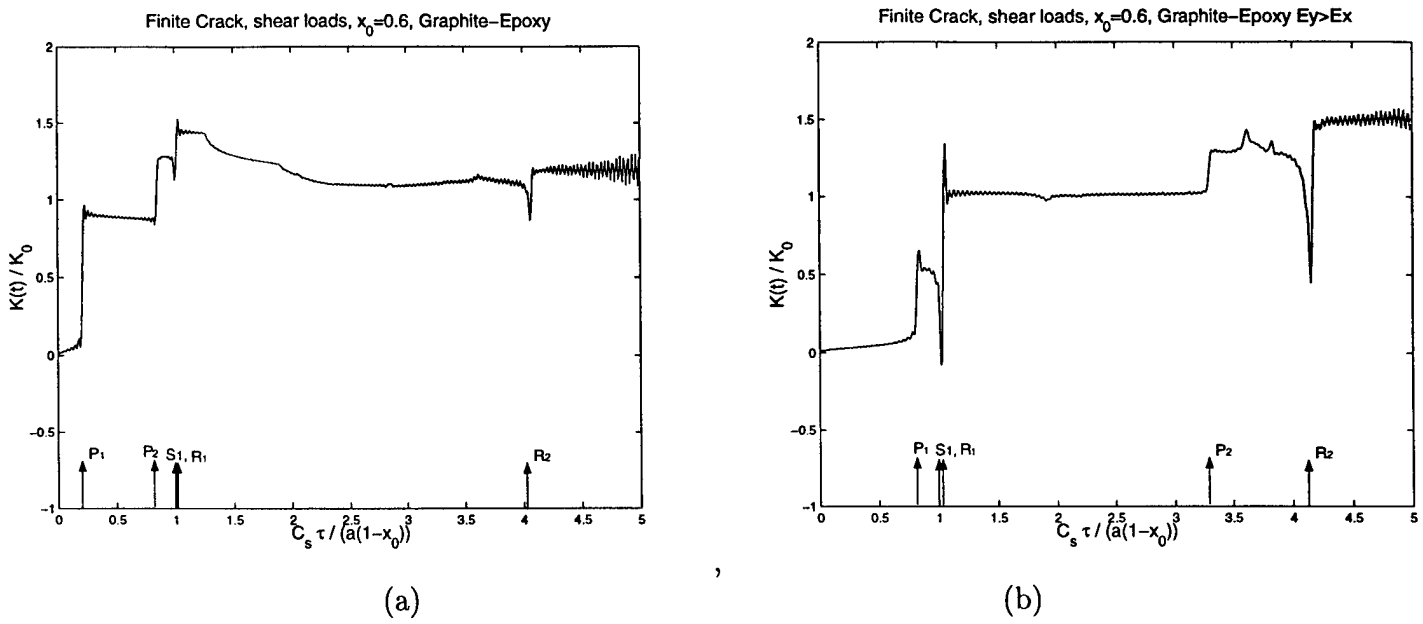

(a) (b)

Figure 2.3: Stress intensity factor history for a finite crack with concentrated shear loads in orthotropic material. The normalization factor is given by the equation (2.2). The material properties correspond to graphite-epoxy composite with the fibers (a) parallel to the x axis, and (b) fibers parallel to $y-$axis. Labels P_i, S_i and R_i are defined in figure 2.2.

fibers along the $y-$axis the results are quite similar to figures 2.2 and 2.3(b); two similar cycles of discontinuity at the arrival of the dilatational wave and singularity at the arrival of the Rayleigh wave are observed. We note a similar behavior in figure 2.4 to that illustrated in 2.3(a) for the graphite-epoxy material. The difference is in the times when the jumps occur, that is, the times of the arrival of the dilatational waves, marks P_1 and P_2. For figure 2.3(a) the jumps occur at $t = 0.2$ and $t = 0.84$, while in figure 2.4 they occur at $t = 0.17$ and $t = 0.70$. For the E glass-Epoxy composite, figure 2.5, even though the fibers are along the $x-$axis, we observe the two cycles typical of the case when the fibers are along the $y-$axis. This is due to the fact that for this material in this orientation $x_0/c_R < (1 + x_0)/c_d$. Clearly, there is a strong dependence of $K_{II}(t)$ on the elastic constants in these figures.

It should be noted that for wave propagation along the material principal axes wave pure modes are obtained (Nayfeh 1995), i.e., the polarization vector is directed either along or normal to the propagation direction. Hence, we can distinguish dilatational and shear waves without ambiguity for this case of a crack lying on the principal axes of the material. Also,

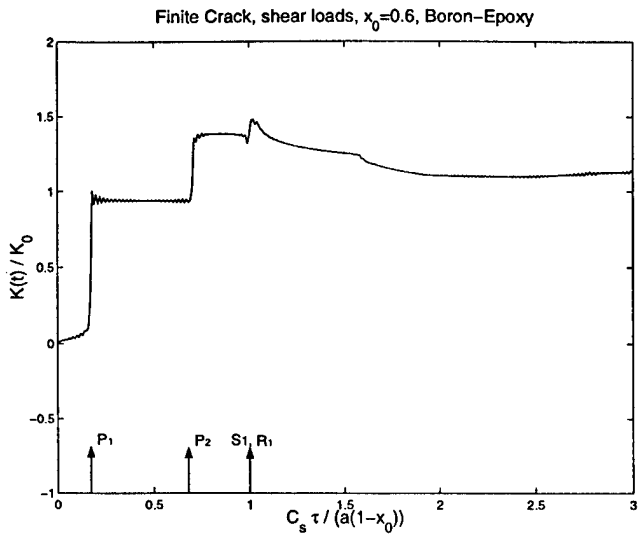

Figure 2.4: Stress intensity factor history for a finite crack with concentrated shear loads in orthotropic material. The normalization factor is given by the equation (2.2). The material properties correspond to boron-epoxy composite with the fibers parallel to the x axis. Labels P_i, S_i and R_i are defined in figure 2.2.

for some materials the singularity when the Rayleigh wave arrives is difficult to capture. This is because the singularity occurs at times between the arrival of the shear wave and the arrival of the Rayleigh wave. As $c_s/c_R \to 1$, the duration of this period approaches 0 making it hard to numerically capture the singularity. See figures 2.3(a) and 2.4 where $c_s/c_R = 1.015$ and 1.006 respectively.

The method outlined here can easily be applied to solve the problem of a finite crack with a single pair of impact concentrated shear loads (figure 2.6(a)). As illustrated in figure 2.6, this problem can be treated by a superposition of the two problems shown, that is, one with a symmetric (figure 2.6(b)) and the other with an antisymmetric (figure 2.6(c)) displacement field. The symmetric part is just the problem solved above with a load of magnitude $q/2$ instead of q. To solve the antisymmetric part we follow a similar procedure, the only difference would be the proposed displacement fields, equations (2.13) and (2.14), it would be required sine and cosine transforms instead of cosine and sine for u^* and v^*, respectively, due to the new symmetry. Application of Laplace and Fourier transforms leads to a reduction of the governing equations to a system of dual integral equation. The stress

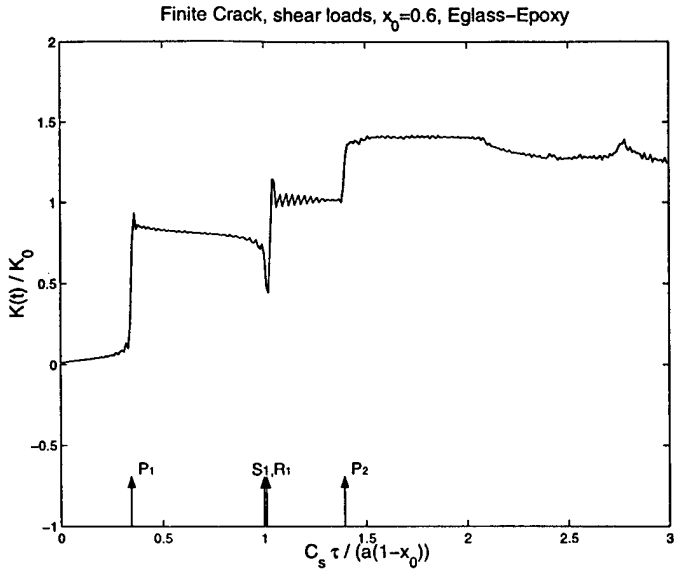

Figure 2.5: Stress intensity factor history for a finite crack with concentrated shear loads in orthotropic material. The normalization factor is given by the equation (2.2). The material properties correspond to E glass-epoxy composite with the fibers parallel to the x axis. Labels P_i, S_i and R_i are defined in figure 2.2.

intensity factor in the Laplace domain is obtained for each problem, and then they are superimposed in this domain. Finally the Laplace inversion is performed on the sum to obtain $K_{II}(t)$ for the original problem. This method of superposition was successfully used by Rubio-Gonzalez and Mason (1998) to find $K_I(t)$ for a single pair of normal loads in a finite crack.

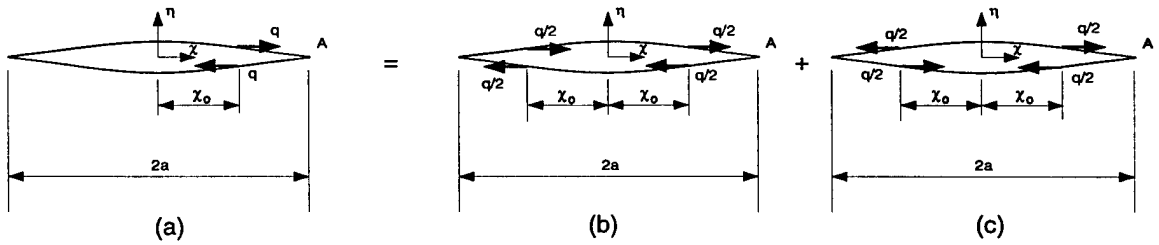

Figure 2.6: Schematic of the finite crack geometry with a single pair of concentrated shear loads. (a) Original problem which may be solved by a superposition of, (b) a symmetric problem and, (c) an antisymmetric problem.

2.5 Conclusions

The dynamic response of a finite crack in orthotropic materials subjected to concentrated in-plane impact shear loads has been presented. The quasi-static solution can be extracted exactly from the dynamic formulation when $t \to \infty$. The transient response shows a strong dependence on the material properties. Some important points follow from this analysis:

1. The arrival of the dilatational wave at the crack tip makes an important contribution to the dynamic stress intensity factor $K_{II}(t)$ unlike in mode I loading where that wave had a minimum effect in $K_I(t)$.

2. The condition if x_0/c_R is greater or less than $(1+x_0)/c_d$, where $x_0 = 0.6$ for this analysis, determines the main features of the dynamic stress intensity factor $K_{II}(t)$. When the greater sign holds, the dilatational waves caused by both loads arrive at the tip $x = +1$ before any other waves, thus their effects are added and as a result $K_{II}(t)$ reaches the maximum dynamic overshoot sooner; this behavior is illustrated in figures 2.3(a) and 2.4 corresponding to graphite-epoxy and boron-epoxy composites respectively with fibers along the $x-$axis in both cases. When the lesser sign holds, two separated and similar cycles in $K_{II}(t)$ occur; each one corresponding to the arrival of stress waves at the crack tip generated by the two load pairs. This behavior is illustrated in figures 2.2, 2.3(b) and 2.5.

3. When $x_0/c_R < (1+x_0)/c_d$, figures 2.2, 2.3(b) and 2.5, a plateau is observed between the two cycles (between R_1 and P_2). On this plateau $K_{II}(t)/K_0 = 1$ regardless of the value of the elastic constants.

Bibliography

[1] Abou-Sayed I.S., Burgers P., and Freund L.B. 1980 *Stress Intensity Factor Due to the Parallel Impact Loading of the Faces of the Crack* Fracture Mechanics: Twelfth Conference ASTM STP 700, pp164-173.

[2] Achenbach, J.D., 1973, *Wave Propagation in Elastic Solids*, North-Holland Publishing Company.

[3] Atkinson, K.E., 1997, *The Numerical Solution of Integral Equations of the Second Kind*, Cambridge University Press.

[4] Chao C.C., 1960, *Dynamical Response of an Elastic Half-space Surface Loadings.*, ASME, J. Appl. Mech. v.27, pp.559-567.

[5] Chen, E.P., and Sih, G.C. 1977, *Transient Response of Cracks to Impact Loads* in Elastodynamic Crack Problems, ed. G.C. Sih, Noordhoff International Publishing.

[6] Debnath, L., 1995, *Integral Transforms and their Applications*, CRC Press.

[7] Freund, L.B., 1974, *The Stress Intensity Factor due to Normal Impact Loading on the Faces of a Crack*, Int. J. Engng. Sci., v12, pp.179-189.

[8] Freund, L.B., 1990, *Dynamic Fracture Mechanics*, Cambridge University Press.

[9] Honig, G. and Hirdes, U., 1984, *A Method for the Numerical Inversion of Laplace Transforms*, J. Comp. Appl. Math., v10, pp. 113-132.

[10] Isida, M., 1972, *Data on Crack Tip Stress Intensity Factors*, JSME v75, n642, pp. 1127-1135.

[11] Kassir, M.K., and Bandyopadhyay, K.K., 1983, *Impact Response of a Cracked Orthotropic Medium*, ASME, J. Appl. Mech. v.50, pp.630-636.

[12] Kraut, E.A., 1963, *Advances in the Theory of Anisotropic Elastic Wave Propagation*, Rev. Geoph. v.1, No.3 pp.401-448.

[13] Lambros J. and Rosakis A., 1995, *Shear Dominated Transonic Interfacial Crack Growth in a Bimaterial-I. Experimental Observations.*, J. Mech. Phys. Solids. v.43, No.2, pp.169-188.

[14] Liu C., Huang Y. and Rosakis A., 1995, *Shear Dominated Transonic Interfacial Crack Growth in a Bimaterial-II. Asymptotic Fields and Favorable Velocity Regimes.*, J. Mech. Phys. Solids. v.43, No.2, pp.189-206.

[15] Nayfeh, A.H., 1995, *Wave Propagation in Anisotropic Media with Applications to Composites*, North-Holland Publishing Company.

[16] Papoulis, A., 1962, *The Fourier Integral and Its Applications*, McGraw Hill, Inc., New York

[17] Parton, V.Z., and Boriskovsky, V.G., 1989, *Dynamic Fracture Mechanics*, v.1, Stationary Cracks, Hemisphere Publishing Corporation.

[18] Roessig, K.M. and Mason, J.J., 1997, *Dynamic Stress Intensity Factors in a Two Dimensional Punch Test*, submitted to Engr. Frac. Mech.

[19] Rubio-Gonzalez, C. and Mason, J.J., 1998, *Fundamental Solutions for the Stress Intensity Factor Evolution in Finite Cracks in Orthotropic Materials.*, Submitted to Int. J. of Fracture.

[20] Rosakis A.J., (1998) Plenary Lecture, The US National Congress in Applied Mechanics, Gainesville, Florida, June 1998

[21] Shindo, Y. and Nozaki, H., 1991a, *Impact Response of a Finite Crack in an Orthotropic Strip*, Acta Mechanica, v.62, pp.87-104.

[22] Shindo, Y., and Nozaki, H., 1991b, *Impact Response of Symmetric Edge Cracks in an Orthotropic Strip*, JSME, v34, No. 1, pp.7-12.

[23] Shivakumar K.N. and Crews J.H., 1998, *Modified Mixed-Mode Bending Test Apparatus for Measuring Delamination Fracture Toughness of Laminates Composites.* To appear in J. Composites Materials.

[24] Schwartz, M. M., 1997 *Composite Materials. Properties, Nondestructive Testing and Repair*, v.1, Prentice-Hall. Upper Saddle River N.J.

[25] Shukla A., Singh R., Lambros J., and Rosakis A. (1998) *Investigation of the Mechanics of Intersonic Crack Propagation Along a Bimaterial Interface Using Coherent Gradient Sensing and Photoelasticity.* To appear in the Proceedings of Royal Society London.

[26] Sneddon, I.N., 1966, *Mixed Boundary Value Problems in Potential Theory*, North-Holland Publishing Company.

[27] Stroh, A.N., 1962, *Steady State Problems in Anisotropic Elasticity*, J. Math. Phys., v41, pp. 77-103.

Part II

Investigations of Isotropic Metals

Chapter 3

Adiabatic Shear Localization in the Impact of Edge Notched Specimens

Co-authored with K.M. Roessig, to appear in Experimental Mechanics

Abstract

Impact experiments are performed on edge notched specimens in the two dimensional punch geometry. Materials tested include 18Ni(350) maraging steel, S7 tool steel, 4340, 300M, HP 9-4-20, and D-6ac ultra high-strength steels and titanium 6% Al-4% V alloy (Ti6Al4V). These materials have shown a high susceptibility to dynamic shear failure in previous studies. Impact velocity ranged from 25 m/s to 45 m/s, and shear bands were found to form at the notch tip and at the die corner on the back side of the specimen for all materials tested. Metallurgical analysis confirms the existence of adiabatic shear bands followed by a crack propagating through the fully developed shear band. High speed photography was used to observe the initiation of adiabatic shear bands shortly after impact. Laser etched lines on the specimen surfaces allowed the determination of the time of impact and the initiation time of shear failure. The elapsed time between the two was used to estimate the stress intensity factor at the time of shear band initiation. Comparisons of shear band initiation stress intensity factors at the notch tip and die corner are made. It is seen that the shear bands initiate at approximately the same stress intensity factor at both the notch tip and die corner. Finite element simulations support the use of a square root singularity for the

stress in the plate near the corners of a deformable punch or die.

3.1 Introduction

In the plastic deformation of metals, adiabatic shear bands may form through high loading rates, geometry constraints, or a combination of the two. Adiabatic shear bands are zones of intense shear deformation in which local heating due to plastic work causes temperatures to become very high, thus softening the material and allowing for greater deformation and further heating. The process becomes self feeding and can lead to a collapse of the deformation to a very narrow region. Several reviews of adiabatic shear banding have appeared, the most extensive ones are by Bai and Dodd [1] and Rogers [2].

In the modeling and study of shear bands, one of the most desirable accomplishments is to accurately predict the onset of shear localization. Zener and Hollomon [3] originally proposed an adiabatic shear localization criterion which states that when the stress decreases with an increase in strain at a material point, the deformation at that material point is unstable. A more common criterion used, primarily for its simplicity, is a critical strain criterion [1, 4]. Other proposed criteria include those related to kinetic energy changes [5, 6], internal work hardening parameters [7], and maximum stress conditions [8].

Recently, the stress intensity factor has also been proposed as a shear band initiation criterion [9, 10, 11]. Chen and Batra [9] argue that a critical stress intensity factor is equivalent to a critical strain criterion under adiabatic conditions. The stress intensity factor is a measure of the energy release rate based on the elastic stress field. Therefore, it will only apply while the assumption of small scale yielding is valid, i. e., up to and including shear band initiation but not including subsequent propagation. Mason et al. [10] found that laser interference fringe patterns formed after impact of an edge notched specimen resemble the stress field of mode II elastic deformation under the assumption of small scale yielding. After the shear band initiates, the fringe patterns begin to change, and no longer resemble a pure mode II elastic deformation field. Therefore, up to shear band initiation, a mode II K-dominant field exists and the stress intensity factor can be determined for the stress field. It is clear that rate dependency in the initiation of adiabatic shear bands is important.

Critical stress intensity factors for mode I crack propagation have long been known to be rate dependent [12, 13, 14, 15]. Also, in Chen and Batra's analysis [9] it is stated that the instability strain for the onset of shear localization is rate dependent through the constitutive equation. Therefore, the mode II adiabatic shear band initiation stress intensity factor is also expected to be rate dependent.

Adiabatic shear localization has been studied in a variety of tests including the torsional split Hopkinson bar, axisymmetric punch tests, and the impact of edge notched specimens. The impact of edge notched specimens was first conducted by Kalthoff [16], and since has received attention from many researchers [9, 10, 11, 17, 18, 19, 20, 21]. Though the test has met with success for the initiation of shear bands from a notch tip, it's application to a variety of metals is limited. Maraging steels and Ti6Al4V alloy have been used, but beyond that, for example for the metals used in this study, forming shear bands in other metals using this geometry has been difficult if not impossible [22]. Finite element simulations examining the stress intensity factor histories in impact tests on plate and edge notched specimens placed under various geometric constraints show that when the back face is a free surface, the reflected wave is tensile [23], and with the arrival of the tensile wave from the back edge of the specimen, a drop in stress intensity factor results. However, using a fixed back edge or two dimensional punch support geometry results in a compressive reflected wave, and the stress intensity factor increases with the arrival of this wave. Therefore a higher maximum stress intensity factor can be achieved with the same impact velocity if support of the back edge is provided.

Roessig and Mason [24, 25] have recently conducted axisymmetric punch tests and examined the failure of Ti6Al4V under a wide range of loading rates and punch/die clearances. Finite element simulations were also performed to examine localized behaviors within the material and estimate initiation of shear instabilities. By extrapolating the stress intensity factor histories derived by Roessig and Mason [23], a rough estimate of 100 MPa$\sqrt{\text{m}}$ can be made for the initiation stress intensity factor in the punch tests reported in these

studies. Also, impact of Ti6Al4V edge notched plates was conducted by Zhou et. al [11], and in this study, the J-integral was evaluated at initiation for different impact velocities. Extrapolation of these results to the punch velocity in the Ti6Al4V punch tests conducted by Roessig and Mason results in a second estimate for the initiation stress intensity factor of 125 MPa$\sqrt{\text{m}}$. With this encouraging comparison of the stress intensity factor at shear band initiation between these two dissimilar studies, one is motivated to further consider a critical stress intensity factor as a parameter describing the material susceptibility to adiabatic shear localization and as a criterion predicting the initiation of adiabatic shear bands. The purpose of this work is to compare the initiation stress intensity factors from two different stress fields within a single test and to experimentally examine the validity of the stress intensity factor as an adiabatic shear band initiation criterion.

3.2 Experimental Methods

Impact tests of edge notched plates are conducted. In an earlier study, Roessig and Mason [23] examined the dynamic stress intensity factors in the impact of edge notched and rectangular plates with various support geometries. Of the combinations discussed in that work, only the impact of edge notched specimens in the two dimensional punch support configuration is examined here. The edge notched specimens used in this study are 50.8 mm by 101.6 mm. The notch is 12.5 mm in length and is placed 35 mm from one end as shown in Figure 3.1. Tests with double notched specimens were also conducted for S7 tool steel to examine any differences in shear band initiation due to that change in geometry.

The experimental setup consists primarily of an air gun, a Cordin 330 high speed camera, and a specimen/die apparatus. The projectile is a cylinder 15 cm long and 30 mm in diameter and is made of a 18Ni(350) maraging steel hardened to 50 HRC. Impact speeds ranged from 25-45 m/s. The die insert that supports the specimen, as shown in Figure 3.1, is made of 4340 steel hardened to 48 HRC. These materials were chosen to minimize plastic deformation of the projectile and support. A specimen support is threaded onto the barrel to ensure a

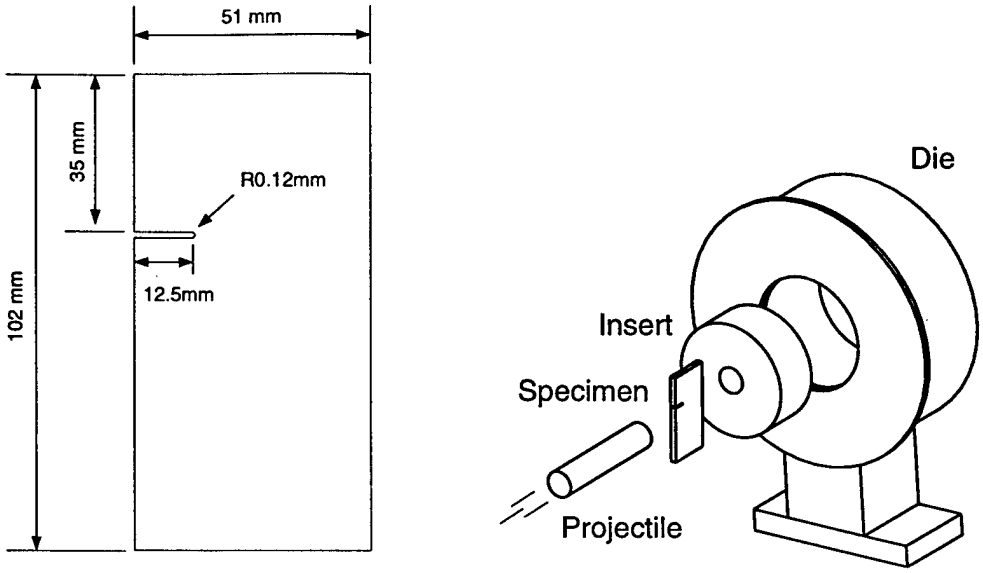

Figure 3.1: Schematic of the edge notched specimen and punch/die configuration.

normal impact. The high speed camera is placed to view the face of the specimen. Lines were etched by laser onto the surface of the specimen at a density of 16 lines/cm to make the shear deformation after impact observable. The Cordin 307 light source was placed in line with the camera, and was triggered by an infrared emitter-detector pair placed on the barrel. A schematic of the experimental setup can be seen in Figure 3.2.

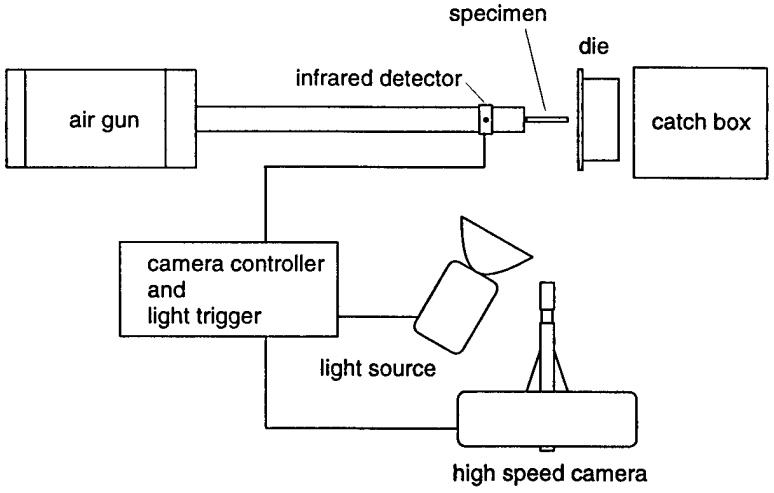

Figure 3.2: Schematic of the experimental setup.

Several materials were tested including Ti6Al4V, 18Ni(350) maraging steel, S7 tool steel, and the ultra high-strength steels 4340, 300M, HP 9-4-20, and D-6ac. The Ti6Al4V was used

in the mill annealed condition, while the other materials were quenched and tempered to Rockwell C hardnesses of 58, 58, 51, 52, 46, and 53, respectively. The heat treatments used are the same as those used by Dillmore and Foster [26] and Mason [22]. In previous studies, these materials have been shown to be susceptible to adiabatic shear banding [27, 28, 29, 4]. Their properties are shown in Table 3.1. Tension tests were conducted on an ATS 900 Universal Testing Machine with strain being measured by an MTS 632.12E-20 Extensometer. All tests were performed according to ASTM Standard E8 to determine the yield strength, σ_y, and strain hardening coefficient, n. The hardening coefficient is found using the relation $n = d(\log\sigma)/d(\log\epsilon)$ in the range from yielding to the maximum engineering stress. These material parameters are measured because they are known to be important in determining a materials susceptibility to adiabatic shear banding [2, 24].

Material	Yield Strength (MPa)	Strain Hardening Exponent
C350	2300	0.081
Ti6Al4V	1000	0.021
4340	1370	0.104
300M	1450	0.172
D6ac	1440	0.160
S7	1500	0.130

Table 3.1: Constitutive properties of the materials used in this work.

In the study by Roessig and Mason [23], the stress intensity factor histories are shown to be different for the notch tip and the die corner. As the stress intensity factor is dependent upon the impact speed, two different impact speeds were used in this study to compare the initiation stress intensity factors, K_i, at the die corner and notch tip. A 45 m/s impact speed yields a stress intensity factor history for the notch tip that is comparable to a stress intensity factor history for the die corner at a 35 m/s impact speed. The sets of experiments described here do not examine the rate dependency of shear band initiation, so similar $K(t)$ time histories were used to eliminate rate effects. It is felt that before rate effects can be examined, the concept of using the stress intensity factor as an initiation criterion for adiabatic shear bands should be validated. That is the purpose of this work. Examination

of rate effects is left for future studies.

Stress intensity factor histories used to estimate K_i were determined through finite element analyses following the method of Roessig and Mason [23]. These finite element simulations used quarter point elements at the punch corner to force a square root singularity, and plane stress elements were used to model the thin plate. This method makes many idealizations which are not true for the experiments described here. For example, the projectile was assumed to be rigid. Due to the high strength and modulus of the specimen materials, the use of an approximately rigid projectile is not experimentally feasible in the impact tests. The projectile used here is made of hardened 18Ni(350) maraging steel, which has a higher yield strength and equivalent modulus as the specimen materials, consequently, it will not act as a rigid projectile. This reduces the effective impact speed as a compressive wave will also travel back down the projectile. Therefore, the stress intensity factors derived from the numerical analysis in [23] will be higher than for the actual tests. To obtain similar impact speeds in the finite element and experimental tests, an impact speed for the rigid projectile in the finite element analysis of half the physical impact speed in the experiment was used [20].

The stress singularity assumed at the punch corner in the finite element analysis may also be different for the experiment. It is well known that a square root singularity in stress exists in a deformable material near the sharp corner of a rigid punch [30, 31, 32, 33], but the singularity at the corner of a deformable punch may be different. For that reason, a separate three dimensional, static, elastic finite element analysis of the stress singularity in the specimen loaded under a deformable punch is conducted. This is the simplest analysis which does not assume the form of the singularity, as in the analysis described in the previous paragraph, and also eliminates the assumptions of a rigid punch or plane stress conditions. The finite element package ABAQUS/Standard is used. The mesh of the specimen consisted of 20-node quadratic bricks with 15-node quadratic prisms at the point under the corner of the punch, see Figure 3.3. Near the punch corner, there are 25 layers of 20-node bricks

to model the deformation as accurately as possible. The punch was made of 8-node linear bricks, and a prescribed displacement was given to the end opposite the one in contact with the specimen. Displacements were recorded along a radial line directly under the punch corner. The singularity was determined by the slope of the logarithm of the displacements. This singularity was compared to the same specimen loaded by a rigid punch with the same prescribed displacement. In this way, any error associated with the contact between two bodies could be neglected.

Other differences between the idealized test and the physical impact test exist. The first of these differences is the notch radius as compared to a sharp crack. The stress field around a finite radius notch was examined by Tada et al. [34] for small angles away from the notch axis. It is stated that the equations for the sharp crack are valid for a slender notch as long as the radial distance in question is large compared to the notch radius. The notch in these experiments was created by an electric discharge machining (EDM) process, and the notch radius is approximately 0.075 mm. At distances of only 1 mm away, the radius is over an order of magnitude larger than the notch radius, so any variations due to the finite notch radius are neglected for this work. The projectile and die corners are also not sharp as in the analytical analysis, but have finite machined radii of 0.25 mm. Again, by the argument above, these effects are neglected in this work.

3.3 Results

Formation of shear bands at the die corner is confirmed by a metallographic analysis. Post mortem polishing and etching of the specimens reveals shear bands as the white etched lines mentioned by Rogers [2]. Figure 3.4 shows a shear band tip initiated at the die corner in a specimen of HP 9-4-20 impacted at 35 m/s. The fully developed band was measured at 1.4 mm in length and appears as a white line in the picture. In front of the band, the grains show large shear deformation. A rough estimate of the process zone length from the micrograph is 75 μm. After further deformation, and the shear band has propagated well into the specimen,

a)

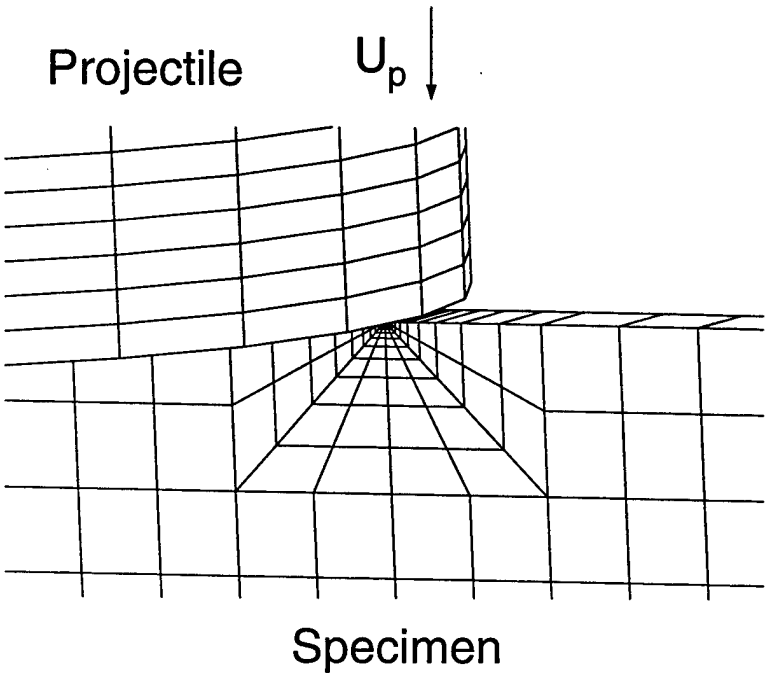

b)

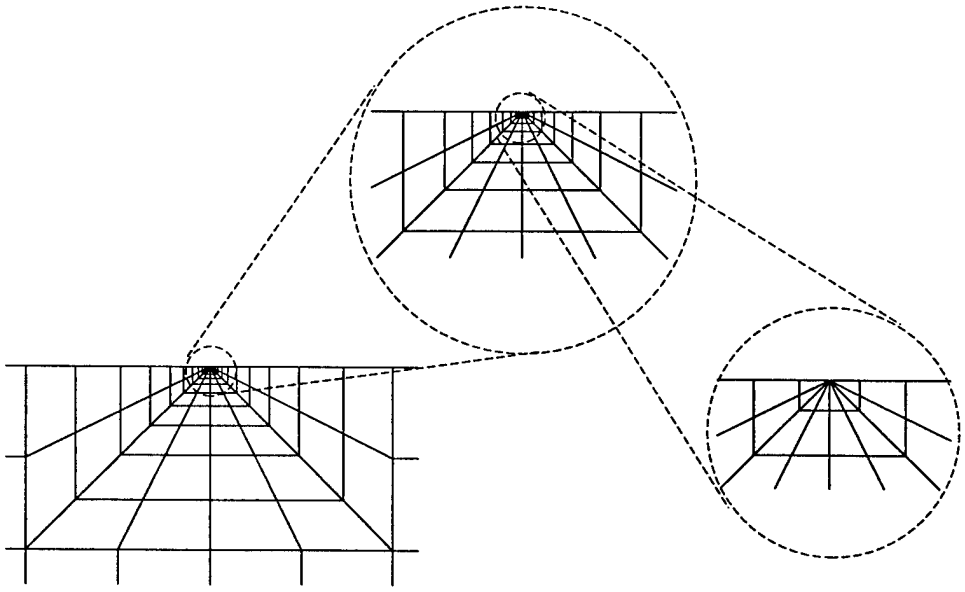

Figure 3.3: The three dimensional finite element mesh used under the corner of the deformable punch is shown in a), while a close view of the elements at the punch corner is shown in b).

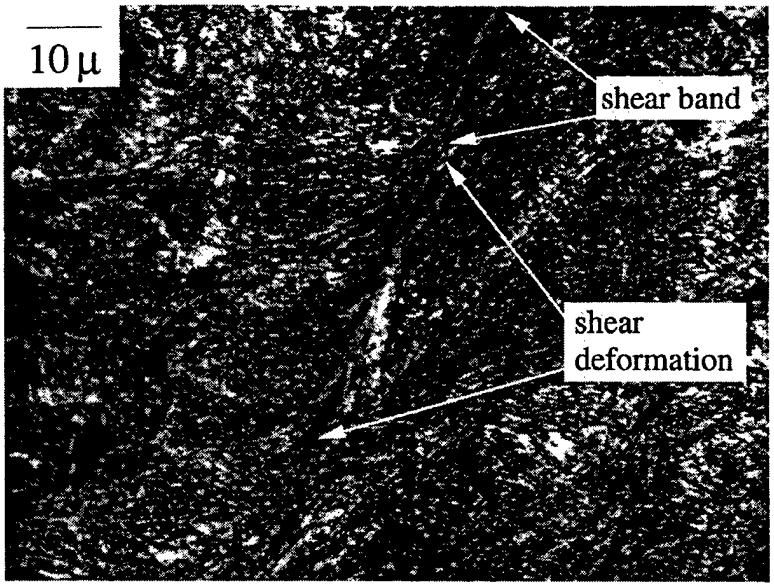

Figure 3.4: Adiabatic shear band tip and process zone near the die corner in an HP 9-4-20 specimen impacted at 35 m/s. The shear band tip shown here is the end of a long white etching band similar to the one shown in Figure 3.5.

a crack initiates at the shear band initiation site and propagates along the path of the shear band. Figures 3.5 and 3.6 show a well formed shear band with a crack that initiated at the die corner in a D6ac specimen impacted at 35 m/s. The band has already propagated into the specimen approximately 4 mm. At later times, the crack propagated through the shear band as seen in Figure 3.7. In this picture of a Ti6Al4V specimen impacted at 45 m/s, the crack eventually splits the white etching layer. In all materials, at the die corner and notch tip, the adiabatic shear band is observed to have initiated first with a crack propagating behind during failure of the specimen. The fracture surface confirms that the failure mode was ductile and shear in nature. Figure 3.8 shows the parabolic voids characteristic of a ductile shear failure found during adiabatic shear localization [1, 35, 36]. The fracture surfaces of the 4340 and 300M steel specimens shown in Figure 3.8 are representative of all the fracture surfaces of the various materials, with void sizes ranging from 1-5μm. Extensive plastic deformation after shear band initiation prevented a complete examination of all materials at different impact speeds. Additionally, shear band often propagated completely through the specimen. For these reasons, a comparison of shear band lengths and widths is not given.

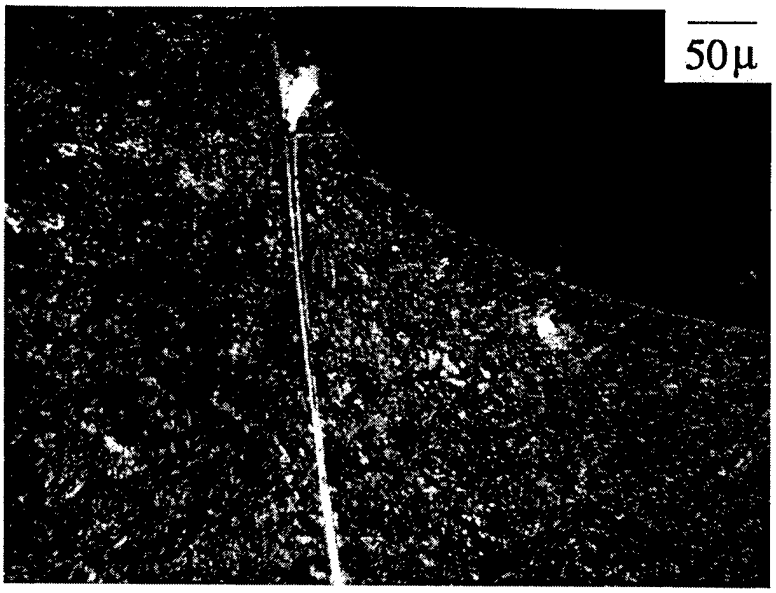

Figure 3.5: Adiabatic shear band initiation site at die corner in a D6ac specimen impacted at 35 m/s. A crack has initiated propagated through the shear band.

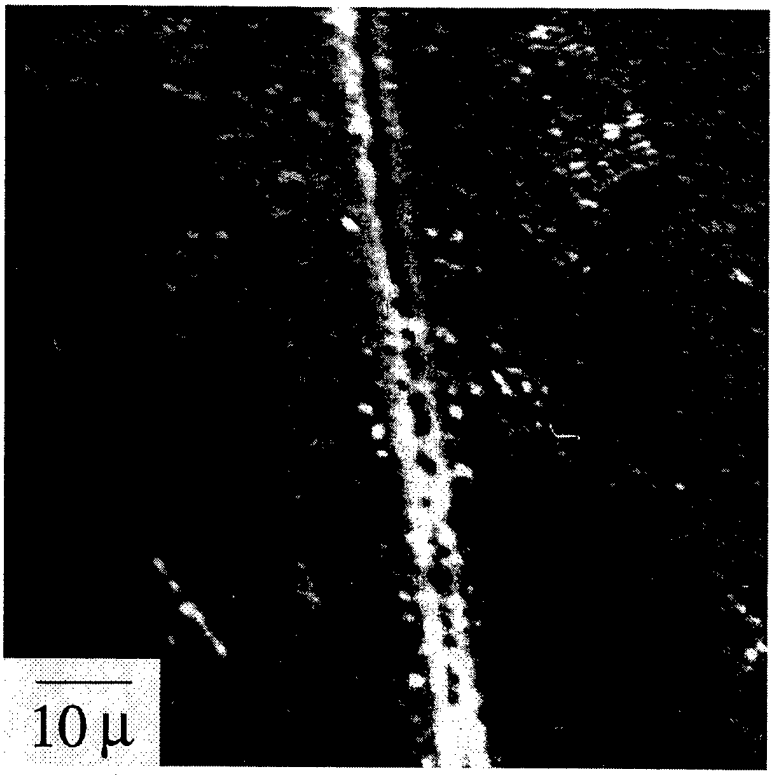

Figure 3.6: Close view of the crack tip seen in Figure 3.5.

High speed photography of the laser etched specimens allowed for the recording of the development and propagation of adiabatic shear bands. Figure 3.9 shows the formation

of an adiabatic shear band at the die corner in a 300M steel specimen impacted at 35 m/s. Initiation of the shear band was determined to occur just before the frame in which propagation is initially observed. The first picture shows the undeformed lines before the compressive wave has impinged on the back surface. After 20 μs, the etched lines have been sheared at the middle of the picture on the right side. In the third picture, just 3 μs later, the shear has collapsed to a much thinner region occurring along a line extending from the die corner. In the last picture, after another 8 μs, the shear band is seen propagating into the specimen. Shear band formation at the notch tip and die corner during the impact of double notched specimens was identical to that of the single notched specimens.

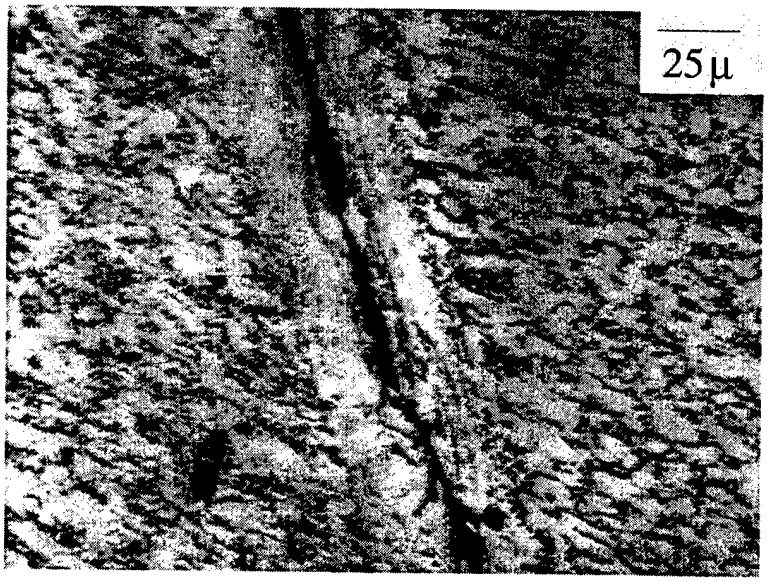

Figure 3.7: Adiabatic shear band in Ti6Al4V alloy with a crack that completely propagated through the band.

One interesting point is that two shear bands can form at the die corner. Figure 3.10 shows two shear bands initiating from the die corner in a 4340 steel specimen impacted at 45 m/s. This behavior has been observed in post mortem examinations of Ti6Al4V alloy by Holt et al. [37], but this is first time the formation of the two bands has been recorded in real time. The shorter shear band initiates first, the other initiates approximately 8μs later but then propagates further into the specimen. The shear bands have separate initiation sites along the die corner; this is also seen in micrographs by Holt et al. Unfortunately,

extensive deformation after the shear band formation shown in Figure 3.10 prevented post mortem examination of the microstructure in the region. This is the only occurrence of this phenomenon seen during this work.

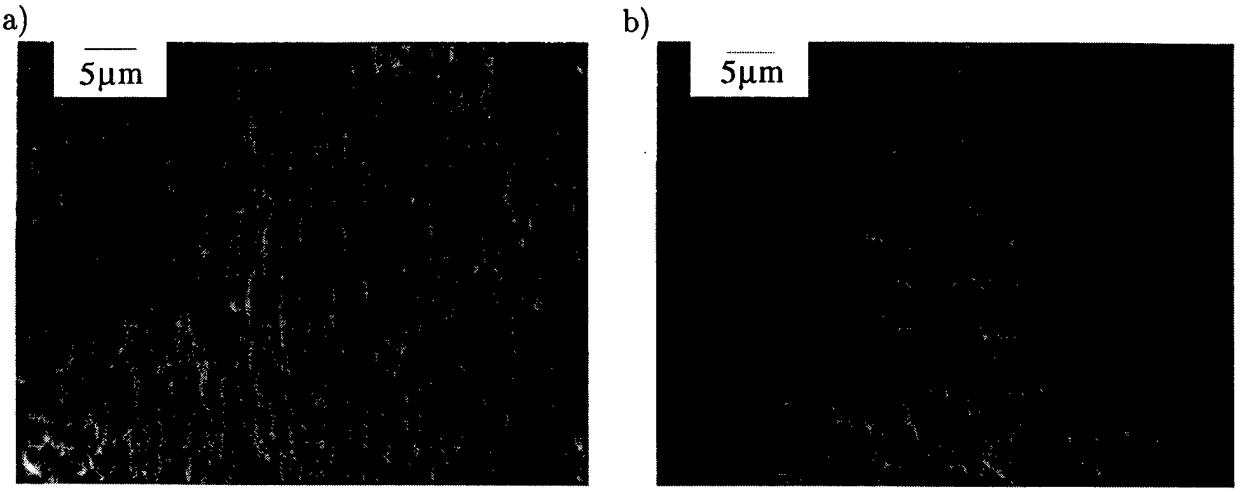

Figure 3.8: Fracture surfaces near the die corner of 4340 and 300M steel specimens impacted at 45 m/s. Parabolic voids characteristic of ductile shear fracture are present.

The finite element analysis revealed that the use of a square root singularity is a good approximation to the stress field in the specimen even in the case of a deformable punch. Assuming a relation between radial distance and displacement of the form $u = Cr^{\lambda}$, the stress singularity has a value of $\lambda - 1$. For the circumferential direction, the finite element simulation rigid punch results in an exponent of λ=0.5293 on the displacements, giving a power of $\lambda - 1$=-0.4707 for the stress and strain field. The deformable punch gives an exponent of λ=0.5353 on the displacements, a difference of approximately of 1%. The radial directions reveal exponents of λ=0.5359 and λ=0.5509 for the rigid and deformable punches, respectively. The difference between these two values is approximately 3%. From these results, it is concluded that the singularity of the stress fields are comparable between the rigid and deformable punch cases. By modeling the deformable punch on an elastic half space as a 90° corner of a single elastic body, the singularity can be found explicitly. From the analysis of Seweryn and Molski [38], the exponent on the displacements is seen to be λ=0.5445, which leads to a singularity power of $\lambda - 1$=-0.4555 on the stress and strain

fields. This number is comparable to the powers found by the finite element simulations. Therefore, within a few percent, the singularity of the rigid and deformable punch stress fields are assumed to be the same.

3.4 Discussion

The analysis of the high speed photography allowed for a number of macroscopic observations. The main focus of this experiment was the determination of an initiation stress intensity factor. Combined with the tension test data, a comparison of adiabatic shear band susceptibility can be made. The angle at which the shear bands form from the die corner can also be examined and compared with theoretical predictions. Microscopically, the location of shear band initiation point along the punch/die corner can be examined to determine the effect of rounded corners as opposed to sharp ones. Each of these points will be discussed in detail.

The average initiation stress intensity factors, K_i, for the different materials for nominally the same stress intensity factor history at both the die corner and the notch tip are shown in Table 3.2. Initiation times, measured from th time of impact, representative of each material are also listed in the same table. These values change with impact speed and are provided only to give the reader an idea of the time scales involved. The last column is the average K_i for all tests for shear bands initiated at the die corner or the notch tip. Comparison of K_i for the die corner and notch tip shows that there is not a large difference between the initiation values for the two different stress fields. Maximum differences between the two are about 10%. The interframe time used in these tests was 2.78μs. From the stress intensity factor histories used to determine the initiation values, a difference of 2.78μs means an approximate change in K_i of 20 MPa$\sqrt{\text{m}}$. Therefore, assuming a possible error in judging the initiation frame by plus or minus one frame leads to an uncertainty in K_i of $\pm$20 MPa$\sqrt{\text{m}}$. By this argument, the initiation values of the stress intensity factor for both the notch tip and die corners are essentially equivalent in these tests. The novel

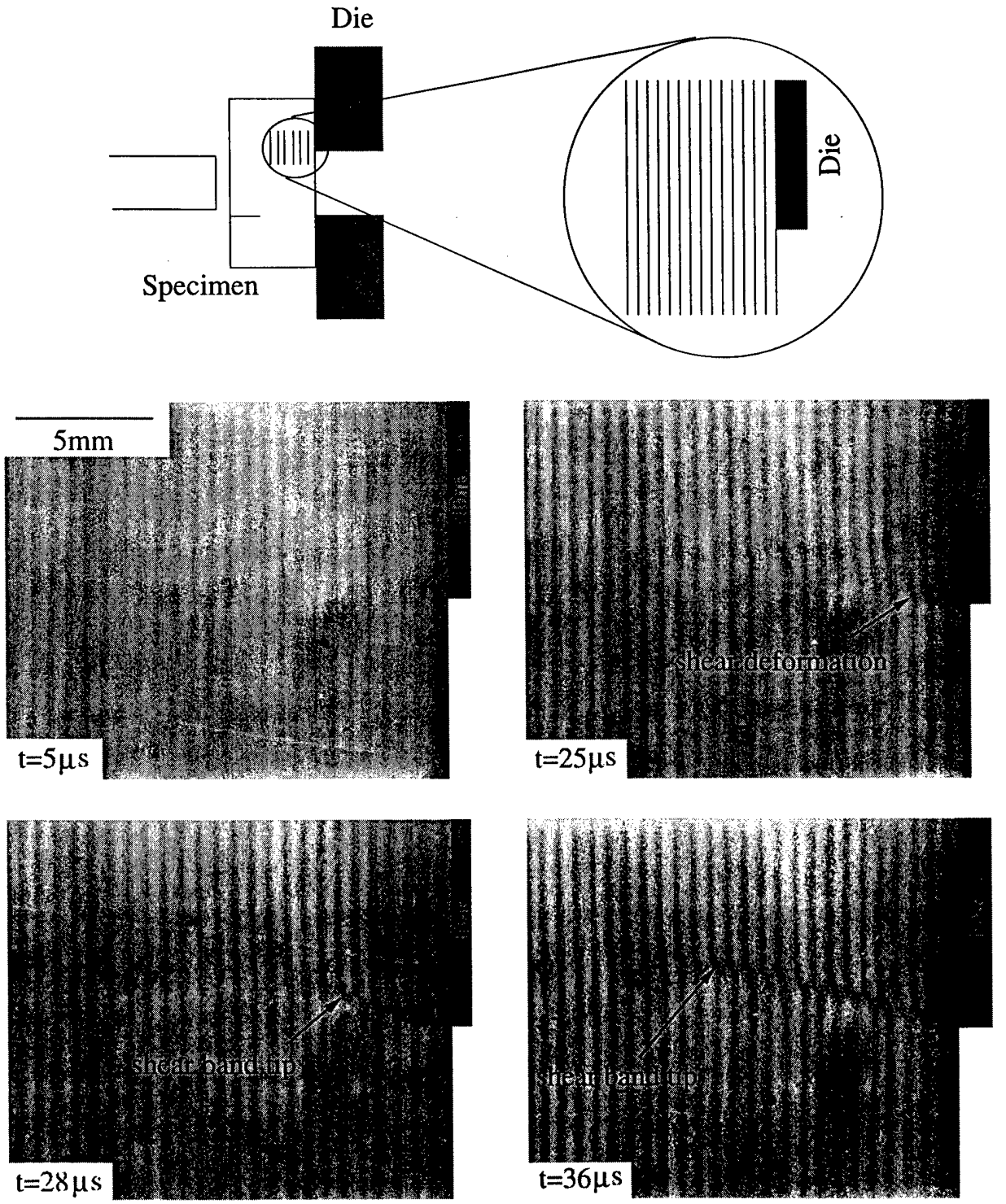

Figure 3.9: High speed photography sequence of adiabatic shear band formation near the die corner in 300M steel impacted at 35 m/s. The schematic indicates the area on the specimen surface that appears in the photographs.

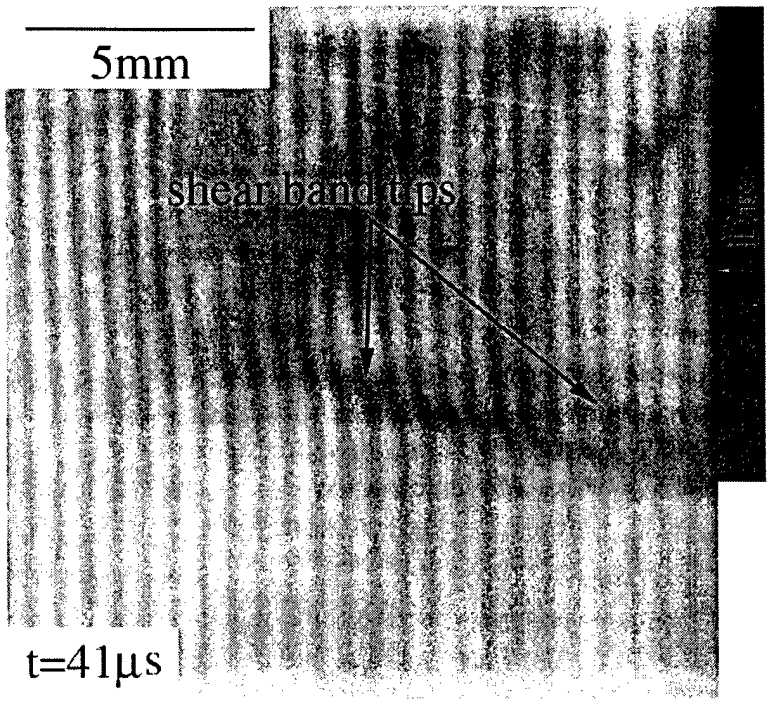

Figure 3.10: High speed photograph of two shear bands forming at the die corner in a 4340 steel specimen.

concept of this comparison is that the geometry at each initiation location is quite different; yet the stress intensity factors at shear band initiation are essentially equivalent. This result strongly supports the assertion that the stress intensity factor can be used as a criterion for shear band initiation in the same manner it is for tensile crack initiation.

Plotting the initiation stress intensity factors against material parameters allows for a comparison of the shear band susceptibility and a demonstration of the dependence of this parameter upon the material constitutive law. Chen and Batra [9] obtain a monotonically increasing relationship between the instability stress intensity factor, K_i, and the critical strain, γ_i. The critical strain can be related to the material parameters through the instability analysis of Bai and Dodd [1]. By assuming a power law hardening model with constant strain rate, adiabatic conditions and linear thermal softening, it can be shown that the critical strain for adiabatic shear localization is proportional to square root of the strain hardening

Material	t_{iD} (μs)	K_{iD} (MPa$\sqrt{m}$)	t_{iN} (μs)	K_{iN} (MPa$\sqrt{m}$)	Avg. K_i (MPa$\sqrt{m}$)
C350	13	81	26	88	83
Ti6Al4V	25	132	40	115	127
4340	22	222	36	195	211
300M	23	220	38	200	213
D6ac	25	241	40	210	231
HP 9-4-20	27	293	45	295	294
S7	N/A	N/A		225	225

Table 3.2: Average initiation stress intensity factors, K_i, for each material at the die corner and notch tip. The subscripts D and N represent values for shear band initiation at the die corner and notch tip respectively. The last column represents the average K_i over all the tests. The initiation times listed here are representative values only and will vary with impact speed.

exponent divided by the yield strength, or

$$\gamma_i \propto \sqrt{\frac{n}{\sigma_y}} \tag{3.1}$$

following the notation of Bai and Dodd and Chen and Batra. Figure 3.11 shows K_i as a function of the yield strength, σ_y, divided by the strain hardening exponent, n, for each material. As the instability stress intensity factor will monotonically increase with instability strain, the data presented here is expected to vary as $1/\sqrt{\gamma_i}$, or $1/\sqrt{\sigma_y/n}$. High strength and low strain hardening are known to make a metal more susceptible to shear banding [2, 24]. Tensile tests of 1018 mild steel gave a lower σ_y/n parameter than the materials shown, and shear localization could not be attained in the impact tests. This indicates a very high K_i and further motivates the upward slope of the curve near σ_y/n=0. The shape of the plot is similar to a plot found for mode I fracture of metals [35]. For mode I fracture, the crack initiation stress intensity factor is a function of the yield strength of the material, and the general trend is that higher strength materials have lower critical stress intensity factors. A similar trend is seen here; a material will have a lower critical stress intensity factor for shear band initiation with higher yield strength and lower strain hardening. This does not mention strain rate effects, which are important [25], but gives a general idea of which materials are more likely to shear band and how that susceptibility depends on yield strength and strain

hardening. The investigation of rate effects is left for a future study.

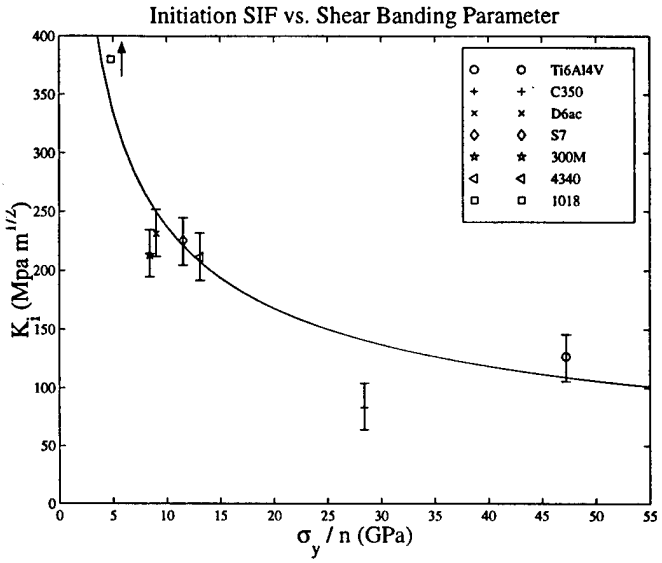

Figure 3.11: Initiation stress intensity factors as a function of the shear banding parameter σ_y/n for all materials tested.

The angle at which the shear band forms with respect to the notch tip or the free surface at the die corner can be predicted. In a pure mode II elastic stress field around a crack tip, the maximum shear stress occurs along the crack axis, but shear bands typically form 5°-15° away from the crack axis. Chen and Batra [9] analyze the angle at which the maximum plastic strain occurs along the elastic-plastic boundary at the notch tip to show that a 6°-20° variation can be found analytically, depending upon the mixity parameter. A similar type of analysis can be performed on the stress field around a die corner. The elastic stress field at the die corner is given by Nadai [32], and analysis of the shear stress leads to a maximum shear stress direction of 110° away from the free surface of the specimen. Examining the plastic zone at the die corner in a way similar to Batra's analysis, an angle of shear band initiation of 95° is found. Actual angles measured from specimens gave an angle of approximately 105°, which falls between the two analytical estimates given above. The elastic estimate is closer to the actual value, and because it is easier to determine, the elastic analysis for maximum shear stress is recommended as an adequate method for estimating

the shear band angle in the case of the die corner. It is interesting to note that the angle of shear band propagation measured above would cause the shear bands formed at the punch corners in an impact test of a plate specimen to propagate in a direction toward each other and may form a projectile-like point in the specimen.

The location of shear band initiation relative to the punch corner reveals information about the stress distribution under the punch. The projectile and die used in the impact experiments have a corner radius of 0.25 mm. In reality because of this finite corner radius, there is not a singular stress field at the punch/die corner. Johnson [30] states an important principle that the pressure distribution between two elastic bodies, whose profiles are continuous through the boundary of the contact area, falls continuously to zero at the boundary. The stresses, therefore, will follow the square root singularity away from the punch/die corner, but must fall to zero at the point where contact between the punch/die and plate ends. The stress distribution will then have a maximum away from the end contact point, as shown schematically in Figure 3.12. One would expect a shear band to initiate at the point of maximum stress, and indeed that seems to be the case, see Figure 3.5. The shear band initiates from the surface in contact with the rounded edge along the die corner where the maximum stress is presumed to be and not from the point where the die and plate initially come into contact. In a punch or die with square corners, these two points would coincide with each other. The effect of rounding the punch or die corners, therefore, reduces the maximum contact pressure and shifts that point away from the initial contact point between specimen and punch/die. Similar effects are seen in finite element studies of shear band initiation at the notch tip [39].

3.5 Conclusion

The impact of edge notched plates has been conducted to examine the initiation of shear bands at the punch/die corners and notch tip. High speed photography was used to view the formation and propagation of adiabatic shear bands within the specimens. An initiation

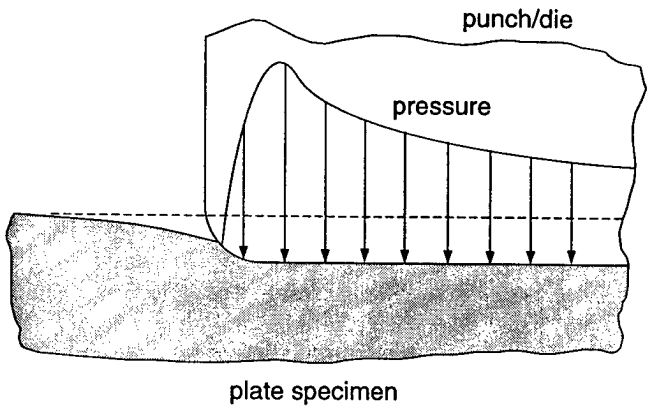

Figure 3.12: Schematic of the pressure distribution under a punch/die corner with a finite radius (K.L. Johnson, 1994).

stress intensity factor for the shear bands in each material tested was determined from a stress intensity factor history obtained through finite element analyses. The materials tested include 18Ni(350) maraging steel, S7 tool steel, 4340, 300M, HP 9-4-20, and D-6ac ultra high-strength steels and titanium 6% Al-4% V alloy. Comparable initiation stress intensity factors for both the punch/die corner and notch tip stress fields were found. The initiation stress intensity factor decreases with increasing yield strength and decreasing strain hardening coefficient. Strain rate hardening is not included in the parameterization.

The use of a square root singularity for the deformable punch is validated by a three dimensional, static, elastic finite element analysis. The singularities between the deformable and rigid punches were shown to differ by less than 3%. The finite punch corner radius is seen to reduce the maximum contact pressure between the specimen and punch, but does not prevent the formation of adiabatic shear bands. In fact, it may promote the formation of multiple bands.

Chapter 4

Stress Field Evaluation Around Adiabatic Shear Band Initiation from a Notch Tip and Die Corner

Co-authored with K.M. Roessig

Abstract

The coherent gradient sensing (CGS) technique is used to examine the out of plane displacement fields around adiabatic shear bands initiating at a notch tip and a die corner. The stress fields around the notch tip, die corner and shear band are modeled using a combination of the mode II or mode I stationary crack tip stress fields and a superposition of shear point loads acting on a propagating crack face. A plane stress assumption is made to relate in plane stresses to out of plane displacements. In 18(Ni)300 maraging steel, shear bands are observed to initiate at the notch tip at a stress intensity factor of 95 MPa$\sqrt{\text{m}}$ and propagate at an average velocity of 650 m/s. Initiation at the die corner in a 4340 steel specimen occurred at a stress intensity factor of about 200 MPa$\sqrt{\text{m}}$ with an average shear band speed of 1020 m/s. In both geometries, a large increase in the stress intensity factor is observed after shear band initiation until an apparent steady state value is reached. In the die corner initiation tests, greater shear band velocities and ratio of increase for the stress intensity factor reflect that a greater $\dot{K}$ at the die corner. The validity of the small scale

yielding assumption is confirmed through the recording and prediction of the elastic stress fields around the notch tip and die corner.

4.1 Introduction

Adiabatic shear banding is the process in which an instability forms in a material under dynamic loading due to the generation of heat from plastic work. Either high loading rates or geometric constraints concentrate deformation in a small area, and large amounts of heat are generated. If loading rates are high enough, heat conduction is negligible, and thermal softening dominates the material behavior over strain and strain rate hardening. As deformation proceeds, thermal softening causes the material to be weaker and deform even further. The deformation can then form a self feeding process and collapse to a small band [1].

Recent experimental studies have used the side impact tests of edge notched specimens to study shear band formation. Originally performed by Kalthoff [16, 40], the test has also been used by Zhou et al. [11] and Mason et al. [10]. The impact tests in these works placed no constraints upon the specimen, so the reflected wave from the back surface is tensile. The main drawback to this experiment is the limited number of materials that exhibit shear localization in this geometry. The tests described here use a variation of this test that included a die support behind the specimen which caused a compressive reflected wave and a subsequent increase in the stress intensity factor at the notch tip. This allowed for shear localization to occur at both the notch tip and die corner during a single test. It was found that the dynamic stress intensity factor at the initiation of the two shear bands was equivalent within the uncertainty of the experimental analysis.

The stress intensity factor has been proposed as a possible adiabatic shear band initiation criterion [9], and its equivalence to a critical shear strain criterion has been shown. The critical strain criterion has been widely used [1], but its applicability to engineering problems as opposed to laboratory conditions has been limited. The stress intensity factor has been

widely used to describe the stress field around a crack or slender notch and has recently been applied to sharp corners [41]. Its use as an adiabatic shear band localization criterion, though, has only been recently investigated [10]. Though the results of the previous chapter are encouraging, the stress intensity factor should be measured directly from the specimen during deformation, and accurately enough to determine if the initiation stress intensity factors at the notch tip and die corner are consistent.

Here, the complete stress field for an initiating shear band is determined from the addition of a dynamic, asymptotic cohesive zone stress field to a stationary crack tip stress field. The cohesive zone is modeled as having a constant shear stress by superposing the solution of a pair of point loads acting on opposite sides of a crack face a constant distance l from the crack tip moving at velocity v [42]. The shear stress need not be constant, but is modeled as such here for simplicity. In previous analyses by Mason et al. [10], the shear band was modeled as a static Dugdale zone. The stress intensity factor history in that study was obtained from the results of Lee and Freund [20] and coherent gradient sensing (CGS) impact experiments performed on PMMA [43], and then the shear stress in the Dugdale zone was modified to fit fringe patterns to the data. The problem with that method is that the stress intensity factor history is assumed known before the test is conducted. Also, no dynamic effects are included. By superposing a point load solution [42], the dynamic effects of the band propagation are included here. The shear band length is measured directly from high speed photographs, and the shear band velocity is determined by a linear regression. As all other parameters depend on material or geometrical considerations, a two variable fit including the stress intensity factor from the notch or die corner and shear stress from the cohesive zone is conducted. The cohesive zone is assumed to have no thickness, and small scale yielding is also assumed. By using the CGS technique to examine the deformation fields around adiabatic shear band initiation from a notch tip or die corner, this work attempts to validate the small scale yielding assumption incorporated into the analysis of the previous chapter and measure K_i rather than calculate it. Additionally, the shear stress in the band

is measured as well.

4.2 Experimental Methods

The specimen geometry is a 50mm × 100mm rectangle with a thickness of 6.4mm. For specimens where notch tip initiation is examined, a notch 25.4 mm in length is placed through an electric discharge machining process 35mm from one edge so that impact occurs just below the notch. The notch radius from this process is approximately 0.075 mm. These specimens are made of 18(Ni)300 maraging steels, also denoted C300, hardened to 52 Rockwell C. For the specimens in which die corner initiation is of interest, a similar notch 12.7 mm in length is used in AISI 4340 steel hardened to 45 Rockwell C. A schematic of the specimens is shown in Figure 4.1. The materials used here are known to be susceptible to adiabatic shear localization.

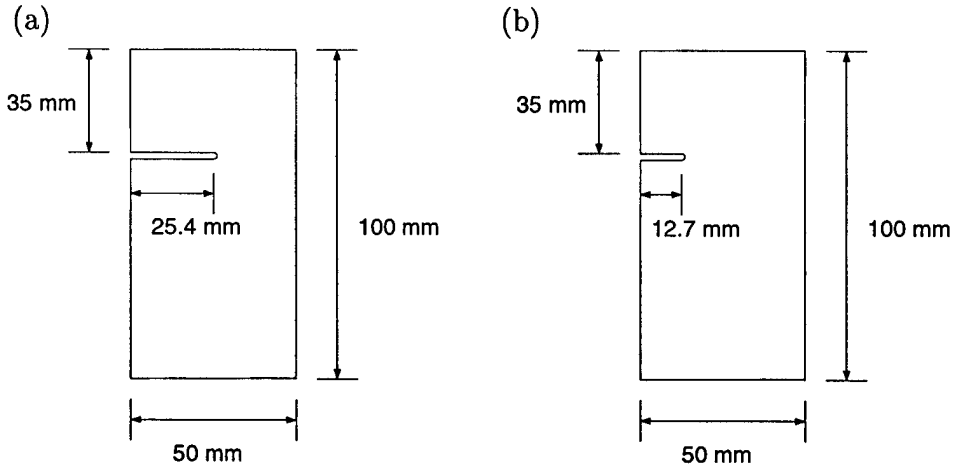

Figure 4.1: Specimen geometries for the study of shear band initiation from the notch tip (a) and die corner (b).

4.2.1 Apparatus

The projectile used in the impact of the specimens is a cylinder 15 cm long and 30 mm in diameter. It is made of 18(Ni)350 maraging steel hardened to HRC 50. An air gun is used to fire the projectile, and a specimen support is threaded onto the barrel to ensure a normal

impact. Two back support configurations are used. A free back surface places no constraints upon the specimen other than to ensure normal impact, while a die is placed behind the specimen to achieve a fixed back support. Figure 4.2 shows the experimental configuration when the die is placed behind the specimen. The insert is used to obtain different punch/die clearances, the clearance being about 0.5 mm for the tests conducted here. The insert is made of AISI 4340 steel hardened to HRC 50, while the die is made of a mild steel. The air gun, barrel, and die are all clamped to a large I-beam to ensure proper alignment. Infra-red emitter-detector pairs are placed at the end of the barrel to both measure the velocity of the projectile as well as trigger the laser and camera.

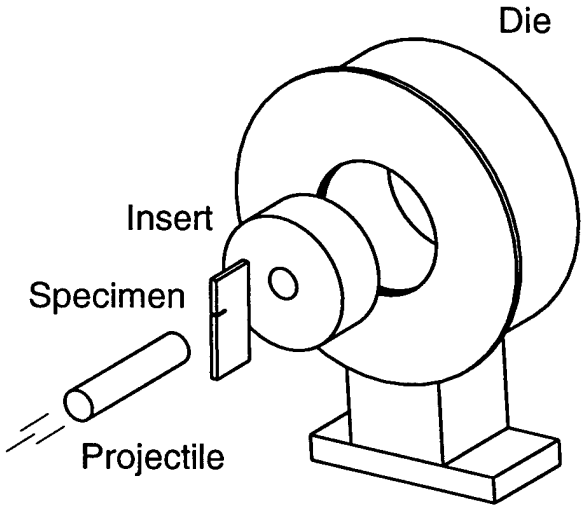

Figure 4.2: Experimental configuration when the die is placed behind the specimen for a fixed back surface.

A collimated argon ion laser beam with a wavelength of 514 nm and 50 mm in diameter is passed through a beam splitter and reflected off the specimens during impact. The CGS technique is used to obtain the fringe patterns of the stress field in the specimen after impact. This system consists of passing the beam through a pair of high density diffraction gratings (40 lines/mm) and then a lens to focus the image. This system will be described more fully in Section 4.2.2. As many images will form from the diffraction gratings, a spatial filter is needed. In this case, the long lens of the Cordin 330 High Speed Camera acts as the spatial filter. The camera is aligned to allow the first order image into the camera. During

the test, the laser is sent through a cavity dumper so that the beam is pulsed for 50 ns in synchronization with the framing rate of the high speed camera.

4.2.2 Coherent Gradient Sensing

The CGS method is used to examine the stress fields in the specimen during a dynamic impact event. The prenotched specimen is lapped and polished to provide a highly reflective, optically flat surface. As the specimen deforms, out of plane displacements will cause the reflected beam to be distorted and the laser light will no longer be parallel. This in effect creates a path length differential between the different light rays. The reflected beam is then passed through a diffraction grating with a line density of 40 lines/mm. This grating, denoted G_1 in Figure 4.3, splits the beam into numerous diffraction orders. For the sake of simplicity, only the first order diffractions are included here. These are shown as E_1, E_0, and E_{-1} in Figure 4.3. Each of these then impinges on a second grating, G_2, of the same line density. There are now nine beams after the second grating as each beam was again diffracted into three more. Of these nine beams, the (-1,0)/(0,-1) and (1,0)/(0,1) beam pairs are parallel. A filtering lens can then be used to focus these parallel beams to a single spot. In the focal plane, a spatial filter is used to eliminate all the superfluous beams. Another lens is then required to produce the final image.

A brief discussion of the analysis as described by Mason et al. [10] now follows, while a full explanation can be found by Tippur et al. [44]. The wave that impinges on the first diffraction grating is assumed to be parallel with some phase difference, $S(x_1, x_2)$, due to the out of plane deformation in the specimen. All disturbances in the beam propagation direction, denoted x_3 in Figure 4.4, are neglected. The two gratings shift the beam a distance

$$\epsilon = \Delta \tan\theta \approx \Delta\theta, \tag{4.1}$$

where Δ is the grating separation distance defined in Figure 4.4, and θ is the diffraction angle shown in Figure 4.3. The diffraction angle is given by the relation

$$\theta = \sin^{-1}\frac{\lambda}{p} \approx \frac{\lambda}{p} \tag{4.2}$$

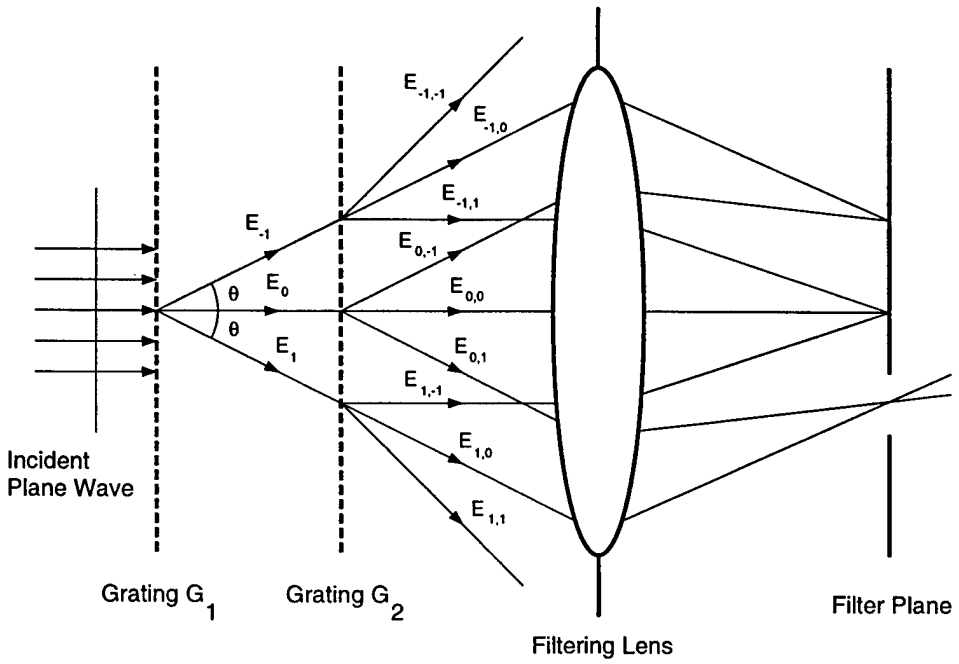

Figure 4.3: Schematic of the principle of CGS.

where λ is the wavelength of the light and p is the grating pitch.

The two parallel, sheared wavefronts constructively interfere if their phase difference is an integer multiple of the wavelength, or

$$S(x_1 + \epsilon, x_2) - S(x_1, x_2) = m\lambda. \tag{4.3}$$

Dividing by ϵ yields

$$\frac{S(x_1 + \epsilon, x_2) - S(x_1, x_2)}{\epsilon} = \frac{m\lambda}{\epsilon} \tag{4.4}$$

which can be approximated as

$$\frac{\partial(S(x_1, x_2))}{\partial x_i} = \frac{mp}{\Delta} \tag{4.5}$$

for small ϵ. Equation (4.5) is valid for the derivative in either the x_1 or x_2 directions.

For an isotropic, linearly elastic material, the out of plane displacements are given by the formula

$$u_3 = -\frac{\nu h}{2E}(\sigma_{11} + \sigma_{22}), \tag{4.6}$$

where ν is the Poisson's ratio and E is the elastic modulus of the material. The stress σ_{11} and σ_{22} are the average plane stresses through the thickness. As plane stress is assumed,

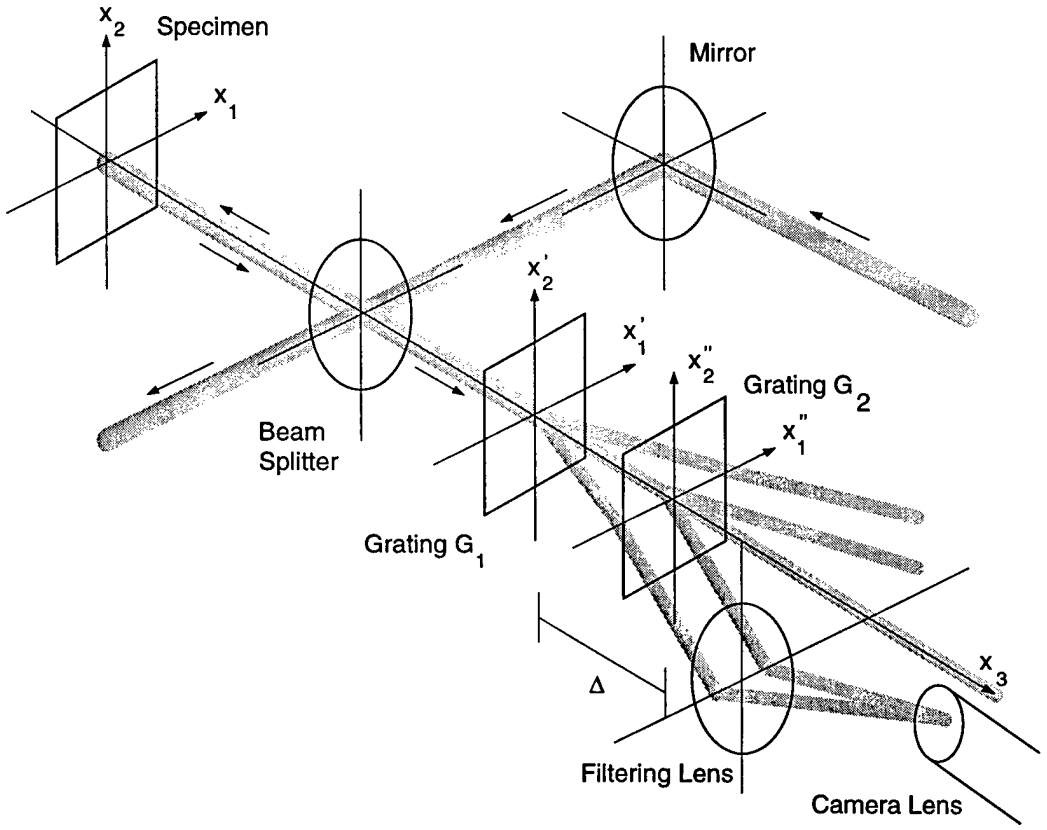

Figure 4.4: Configuration for CGS in this experiment.

σ_{33}=0. The phase difference is related to the displacement and can be approximated by

$$S(x_1, x_2) \approx 2u_3 = -\frac{\nu h}{E}(\sigma_{11} + \sigma_{22}). \tag{4.7}$$

Substituting Equation (4.7) into (4.5) yields

$$2\frac{\partial u_3}{\partial x_i} = -\frac{\nu h}{E}\frac{\partial(\sigma_{11} + \sigma_{22})}{\partial x_i} \approx \frac{mp}{\Delta}. \tag{4.8}$$

Equation (4.8) is used to examine all the fringe patterns produced by the CGS system in this work.

4.2.3 Data Reduction

As stated in Section 4.2.2, CGS measures gradients of the out of plane displacement of the specimen. Assuming a two dimensional stress state, these displacements can be related to the in plane stress fields. Therefore, to predict the shape of the fringe patterns after impact, the stress field must be found. The following sections describe the stress field derivation for each of the cases described in this work.

Notch Tip Initiation

The stress field around the notch tip during shear band initiation is assumed to be given by the superposition of two separate stress fields. The first is the well known mode II stress field around a crack tip [45] given by

$$\sigma_{ij} = \frac{K_{II}(t)}{\sqrt{2\pi r}}\Sigma_{ij}(\theta) \tag{4.9}$$

where for mode II

$$\Sigma_{11} = -\sin\frac{\theta}{2}\left\{2 + \cos\frac{\theta}{2}\cos\frac{3\theta}{2}\right\}, \tag{4.10}$$

$$\Sigma_{12} = \sin\frac{\theta}{2}cos\frac{\theta}{2}\cos\frac{3\theta}{2}, \tag{4.11}$$

$$\Sigma_{22} = cos\frac{\theta}{2}\left\{1 - \sin\frac{\theta}{2}\sin\frac{3\theta}{2}\right\}. \tag{4.12}$$

The assumptions for these stresses are a linear elastic material in the presence of a K-dominant field. The final form of the fringe equations determined by Equation 4.8 becomes

$$\frac{\partial(\sigma_{11}+\sigma_{22})}{\partial x} = \frac{K_{II}}{\sqrt{2\pi}} r^{-\frac{3}{2}} \sin\left(\frac{3}{2}\theta\right) \tag{4.13}$$

$$\frac{\partial(\sigma_{11}+\sigma_{22})}{\partial y} = -\frac{K_{II}}{\sqrt{2\pi}} r^{-\frac{3}{2}} \cos\left(\frac{3}{2}\theta\right). \tag{4.14}$$

Examples of the expected fringe pattern for the mode II deformation field are shown in Figure 4.5. The solid and dashed lines correspond to dark and light fringes, respectively. The thick line on the negative x axis represents the notch.

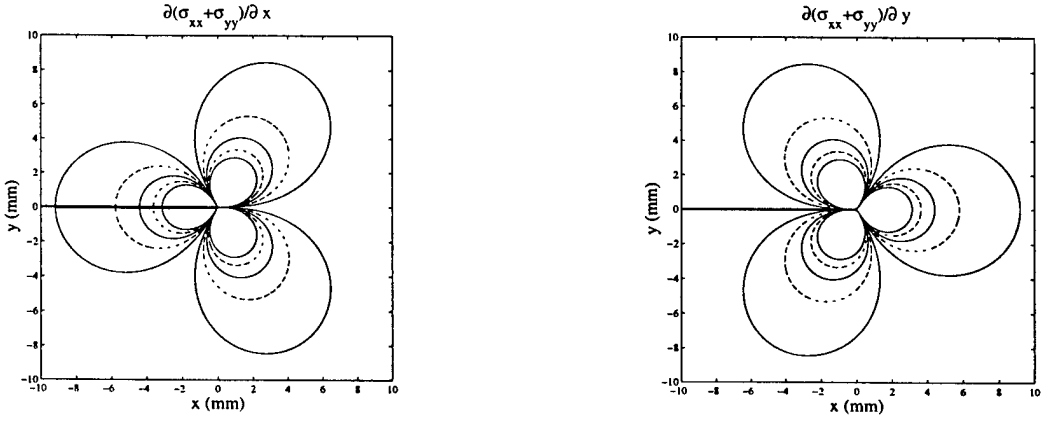

Figure 4.5: Example fringes for the derivatives in both the x and y directions for a mode II deformation field.

The second stress field is due to shear band itself after initiation. This is modeled by a cohesive zone along the notch axis in front of the notch. The cohesive zone uses the solution for a pair concentrated shear loads acting on the faces of a propagating crack [42], see Figure 4.6. By placing many point loads along the crack face, the value of l being different for each point load, a constant shear stress applied over the length of the shear band can be approximated. The value of each pair of point loads depends upon the shear stress and the number of point loads used. In the analysis here, point loads were spaced at every 0.1mm along the shear band length. At late times after shear band initiation, as many as 80 point loads were used.

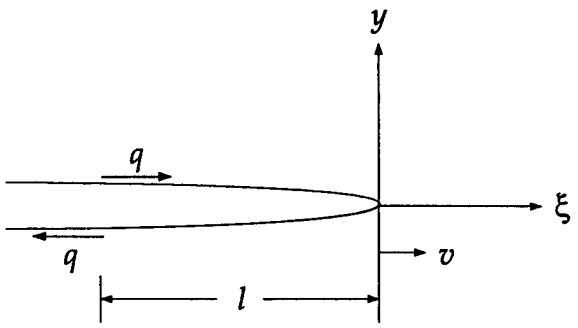

Figure 4.6: Diagram of steady crack growth in mode II due to action of concentrated forces acting a distance l behind the crack tip (Freund, 1990). This solution is integrated along the length of the cohesive zone to model a shear band propagating at velocity v.

The boundary conditions for the point load problem are

$$\sigma_{xy}(\xi, \pm 0) = -q\ \delta(\xi + l), \qquad \sigma_{yy}(\xi, \pm 0) = 0 \tag{4.15}$$

for $-\infty < \xi < 0$ where $\xi = x - vt$. The displacement potentials from a Helmholtz decomposition can be derived by using functions of the complex variables $\zeta_d = \xi + i\alpha_d y$ and $\zeta_s = \xi + i\alpha_s y$ where $\alpha_d = \sqrt{1 - v^2/{c_d}^2}$ and $\alpha_s = \sqrt{1 - v^2/{c_s}^2}$. Because this solution depends upon the shear band velocity, this value must be determined graphically from the photographs. The final solution of the stresses becomes

$$\sigma_{xx}(\xi, y) = \mu \mathrm{Re}\left\{\left(1 - \alpha_s^2 + 2\alpha_d^2\right) F''(\zeta_d) + 2\alpha_s G''(\zeta_s)\right\} \tag{4.16}$$

$$\sigma_{yy}(\xi, y) = -\mu \mathrm{Re}\left\{\left(1 + \alpha_s^2\right) F''(\zeta_d) + 2\alpha_s G''(\zeta_s)\right\} \tag{4.17}$$

$$\sigma_{xy}(\xi, y) = -\mu \mathrm{Im}\left\{2\alpha_d F''(\zeta_d) + \left(1 + \alpha_s^2\right) G''(\zeta_s)\right\} \tag{4.18}$$

where

$$F''(\zeta) = -\frac{2i\alpha_s\sqrt{l}}{\pi D\sqrt{\zeta}(\zeta + l)}\frac{q}{\mu} \tag{4.19}$$

$$G''(\zeta) = -\frac{1 + \alpha_s^2}{2\alpha_s} F''(\zeta) \tag{4.20}$$

and μ is the elastic shear modulus. As seen in Figure 4.6, the origin of the axes is at the tip of the cohesive zone, not at the notch tip. Therefore, a shift of the coordinates by the length of the cohesive zone is required during calculation and subsequent superposition of the stress

fields. This solution assumes small scale yielding, i.e. the deformation outside the cohesive zone is elastic and therefore can be superposed with the stress field around a stationary notch tip. Derivatives of Equations (4.16-4.18) for use in Equation (4.8) were obtained by calculating the stresses at each point shifted by a small amount Δx and then using the first order formula $(F(x+\Delta x) - F(x))/\Delta x$. This method was checked for accuracy using the closed form solutions of the mode II notch tip field and found to be accurate.

Die Corner Initiation

The solution for the complete stress field around the die corner is very similar to that of the notch tip. Again, a stress field around a stationary die corner is generated. The solution of the stresses around the die corner by Nadai [32] is the same as the mode I crack stress field after a rotation. Therefore, the mode I stress field is used here for consistency and is given by

$$\sigma_{ij} = \frac{K_I(t)}{\sqrt{2\pi r}}\Sigma_{ij}(\theta) \tag{4.21}$$

where for mode I

$$\Sigma_{11} = cos\frac{\theta}{2}\left\{1 - \sin\frac{\theta}{2}\sin\frac{3\theta}{2}\right\} \tag{4.22}$$

$$\Sigma_{22} = cos\frac{\theta}{2}\left\{1 + \sin\frac{\theta}{2}\sin\frac{3\theta}{2}\right\} \tag{4.23}$$

$$\Sigma_{12} = \cos\frac{\theta}{2}sin\frac{\theta}{2}\cos\frac{3\theta}{2}. \tag{4.24}$$

The same assumptions apply to the mode I equations as for the mode II equations, (4.10-4.12). The derivatives for the mode I stress field become

$$\frac{\partial(\sigma_{11}+\sigma_{22})}{\partial x} = -\frac{K_I}{\sqrt{2\pi}}\, r^{-\frac{3}{2}}\cos\left(\frac{3}{2}\theta\right) \tag{4.25}$$

$$\frac{\partial(\sigma_{11}+\sigma_{22})}{\partial y} = -\frac{K_I}{\sqrt{2\pi}}\, r^{-\frac{3}{2}}\sin\left(\frac{3}{2}\theta\right). \tag{4.26}$$

Example fringes along with the position of the die and free surface are shown in Figure 4.7. Again, the solid and dashed lines correspond to dark and light fringes, respectively.

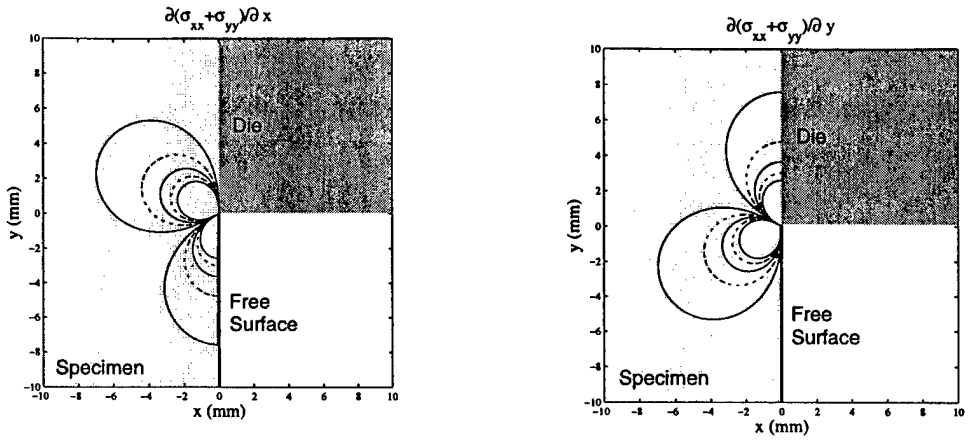

Figure 4.7: Example fringes for the derivatives in both the x and y directions for a mode I deformation field.

To model the shear band growing from the die corner, the same procedure for the notch tip shear band is used. The solution for a pair of concentrated shear forces acting on a propagating crack face is integrated along the cohesive zone length to generate the stress field for the entire shear band. This time, however, the solution must be rotated and translated as the shear band growth direction is not in the same direction as the crack axis from the mode I crack stress solution. This method is approximate because the dynamic point solution assumes an infinite elastic space and does not take into account the boundary conditions along the y axis. Error from the approximation should be limited to the stress field very near the y axis.

4.3 Results & Discussion

Results for each of the two cases listed above will be presented and discussed separately. As the analysis of the initiation of shear bands from a notch tip is simpler and has been addressed to lesser degrees of accuracy by previous researchers [10, 11], these results are presented first. The initiation of shear bands from a die corner is presented second.

4.3.1 Notch Tip Initiation

The sequence of pictures in Figure 4.8 shows the time evolution of the fringe patterns created by the stress field around the notch tip and subsequent shear band after impact of a C300 specimen. The impact speed was 45 m/s. The times shown on the pictures are the time elapsed after impact, and the scale is shown on each picture for digitization purposes. The vertical black line through the picture is due to the light being removed from the framing camera for use in the streak camera apparatus. The shear band length was measured directly from these pictures. The example fringe pattern in Section 4.2.3 shows that the two frontal lobes of the fringe pattern meet at the shear band tip. The shear band length was measured as the length between the origin and the point where the frontal lobes merge. The origin is taken to be at the center of the notch tip and at later times is measured relative to the dark vertical line. This length can be plotted as a function of time to determine the average shear band speed needed to compute the fringe pattern after the shear band initiates, as described in Section 4.2.3. The average shear band speed was determined to be 650 m/s. This number is approximately twice the velocity reported by Mason et al. [10], but the impact speed in the test described here is greater than the one used by Mason. This speed is on the order of the shear band velocities reported by Mason et al. [17] for peak aged C300. Zhou et al. [11] report average shear band velocities from 80 to 1000 m/s depending upon impact speed for the same material for impact speeds less than 45 m/s and with larger specimens.

With the shear band speed known, the fringe patterns from the photographs could be digitized and fitted to theoretical ones. Figure 4.9 shows a sequence of fringe pattern fits for the same photographs shown in Figure 4.8. Only the top half of the fringe pattern is digitized as the lower half is severely distorted due to wave interaction. (The specimen was impacted below the notch.) Also, no digitization points were taken inside the region where three dimensional effects are important. The size of this region is approximately half the specimen thickness [44, 46]. The solid and dashed lines represent theoretical dark and light fringes respectively. The circles are digitized points that should correspond to the solid lines,

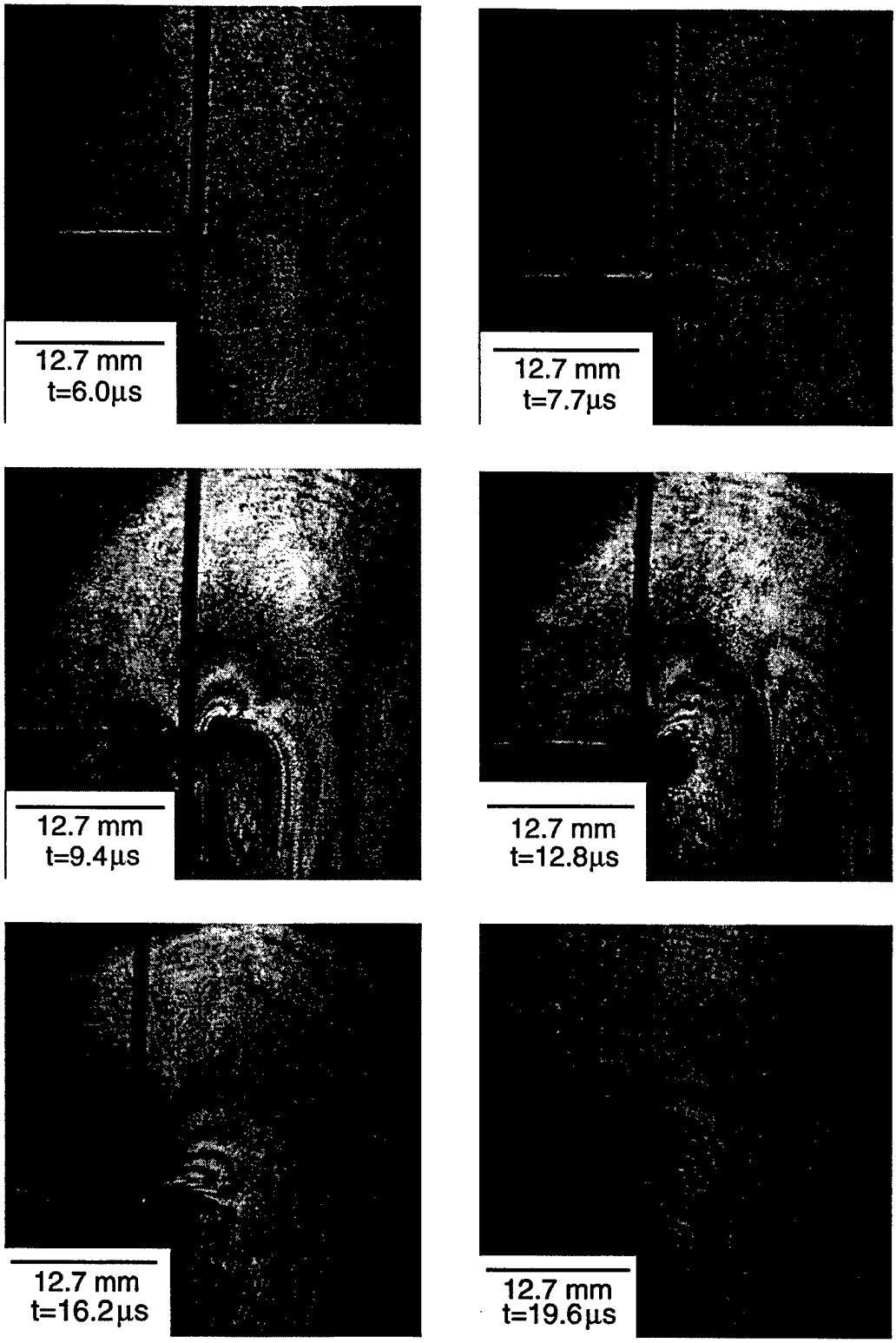

Figure 4.8: Sequence of fringe pattern photographs of an edge notched 18Ni(300) maraging steel specimen impacted at 45 m/s.

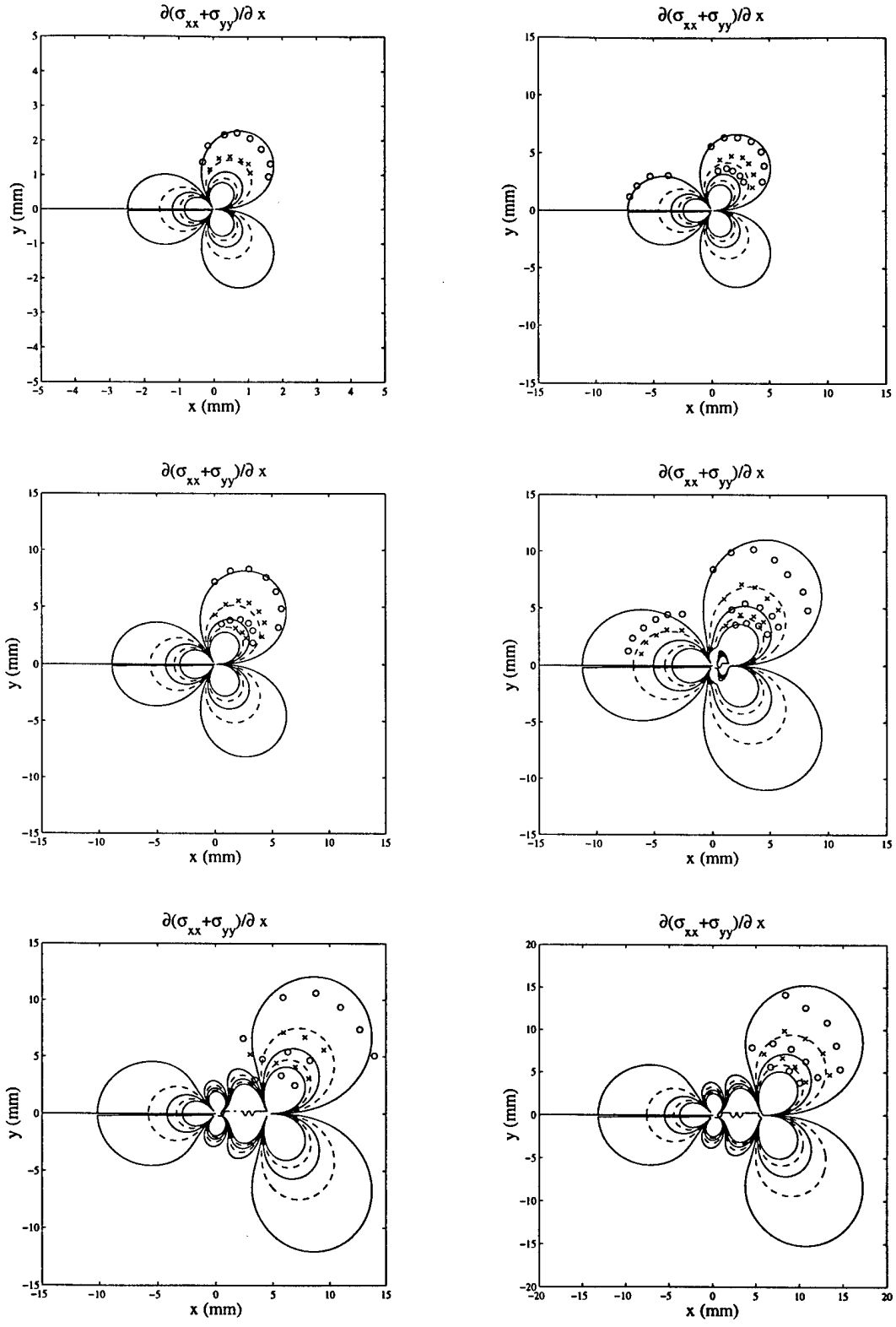

Figure 4.9: Sequence of fringe pattern fits for an edge notched 18Ni(300) maraging steel specimen impacted at 45 m/s.

while the $\times$ points should fall on the dashed lines. The first three graphs are modeled by pure mode II elastic deformation, while the last three combine the mode II elastic deformation and a mode II cohesive zone. The origin in these plots corresponds to the origin in the fringe patterns in Figure 4.8, i.e., the center of the notch tip. The digitization points for the first order fringe match very well until the shear band forms. After shear band formation, it becomes very hard to match the outer fringe while keeping good agreement with the higher order, inner fringes. For this reason, greater emphasis was placed on matching the higher order fringes as these seem to have a greater dependence upon the value of the shear stress used in the cohesive zone fit. In Equation (4.19), for small values of l compared to the spatial coordinate, the power on ζ is -3/2, greater than the -1/2 exponent associated with the mode II elastic crack solution. Additionally, the -3/2 exponent acts from the position of point load application, not the origin. Therefore, the cohesive zone stress field will begin to dominate when close to the cohesive zone but far from the origin, i.e. near the shear band tip. By fitting the higher order fringes more accurately near the shear band tip, the fit for the first order fringe becomes less accurate. This could be due to wave reflection, possible stress relaxation away from the shear band as propagation proceeds, or lack of K-dominance at these distances.

The shear stress and shear band length as a function of time can be seen in Figure 4.10. The shear stress is greater than that reported by Mason et al. [10], but again, the impact speed of the projectile was higher. Greater impact speeds lead to greater shear band propagation speeds, meaning a higher strain rate within the band [11, 18]. The rate effect seems to be displayed here with the greater shear stresses needed to match the observed fringes with the theoretical.

The stress intensity factor history can be examined in Figure 4.11. The measured values from the fits are plotted against the solution by Lee and Freund [20]. The first two points fall very close to the solution by Lee and Freund. The later points, however, show a dramatic increase in the stress intensity factor. This is the first frame in which the shear band has

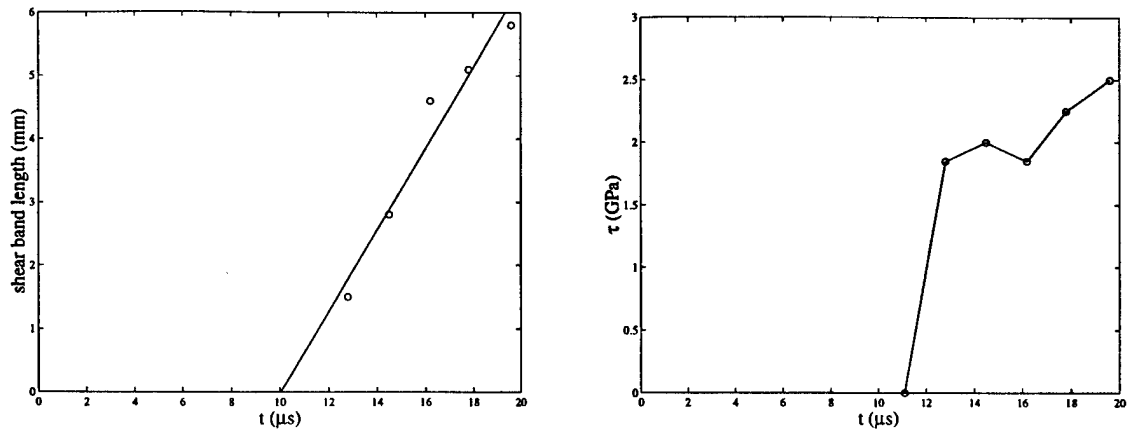

Figure 4.10: Shear band lengths and cohesive zone stresses for an edge notched 18Ni(300) maraging steel specimen impacted at 45 m/s.

initiated. A similar jump in the stress intensity factor is seen by Kalthoff in his measurements through the method of caustics [40]. The initiation stress intensity factor is estimated from the frame immediately prior to initiation to be 95 MPa$\sqrt{\text{m}}$, which is much lower than the value of 140 MPa$\sqrt{\text{m}}$ given by Mason et al. [10]. The measured K_i for C350 from teh 1997 annual report for this contract is 83 MPa$\sqrt{\text{m}}$. The stress intensity factor then continues to increase until the last two points. At this time, the stress intensity factor appears to reach a constant value. It is not clear if this is caused by the wave reflection distorting the outer fringes or if the stress intensity factor reaches a steady state value once the shear band begins to propagate.

4.3.2 Die Corner Initiation

The initiation of an adiabatic shear band from a die corner presents a much more complicated situation than the notch tip initiation. The pictures in Figure 4.12 show the fringe pattern evolution of the initiation event. The impact speed was again 45 m/s, and the vertical black line is present for the same reasons mentioned above. The edge of the specimen is on the right side of the picture and the die corner is the the point at which the black aperture spot begins. This dark area above the die corner is probably due to large out of plane displacements of the specimen against the die and will be discussed in greater detail later. The first two pictures

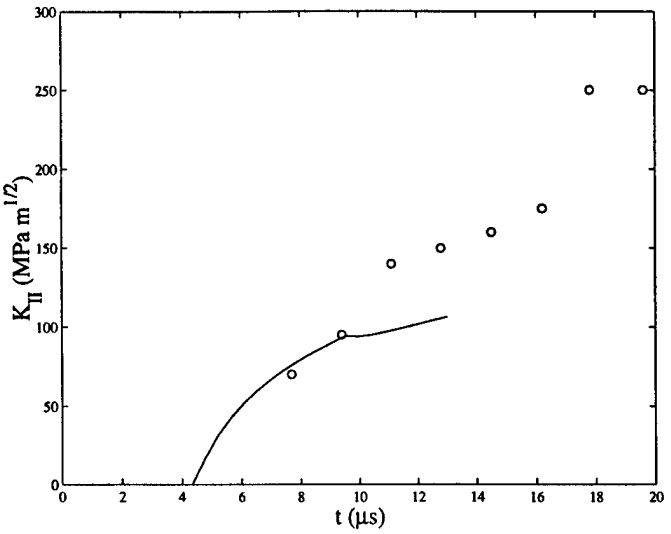

Figure 4.11: Stress intensity factor history for an edge notched 18Ni(300) maraging steel specimen impacted at 45 m/s.

exhibit fringes from the mode I elastic crack solution only, though in the second picture taken at 19.2μs after impact the fringes are admittedly very faint. At 22.6μs, a change in the fringe shape is seen. At this point, the fringes are too small and faint to record any data from them, but by 26.1μs after impact, the picture becomes much clearer. The shear band has propagated approximately 2.7mm into the specimen in this frame. The pattern below the band propagation axis is due solely to the shear band. Above the band propagation axis, though, interference is seen between fringes due to shear band propagation and those due to the compression of the specimen against the die. The last two pictures show the same type of behavior, with fringe patter interference occurring above the band propagation axis. However, as the band propagates further into the specimen, the fringes exhibit the greater curvature around the band tip that is expected as shown by the arrow in the last picture of Figure 4.12. From these graphs, the average shear band velocity was determined to be 1020m/s. The angle of propagation with respect to the die face was measured directly from the specimen after test completion and was found to be 75^o, in agreement withthe previous chapter.

With shear band length, propagation speed and direction known, theoretical fringe pat-

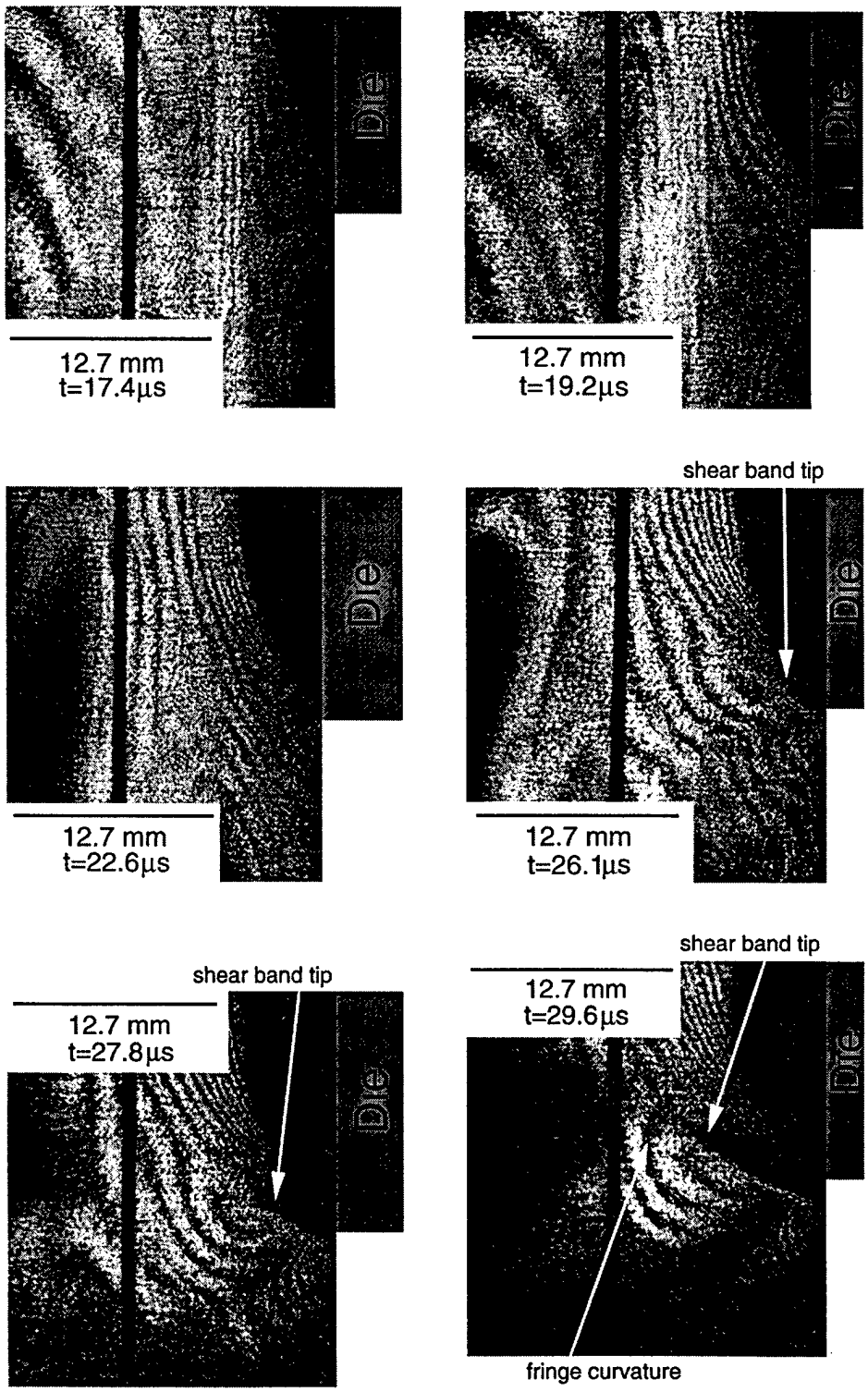

Figure 4.12: Sequence of fringe pattern photographs of shear band initiation at the die corner in an AISI 4340 steel specimen impacted at 45 m/s.

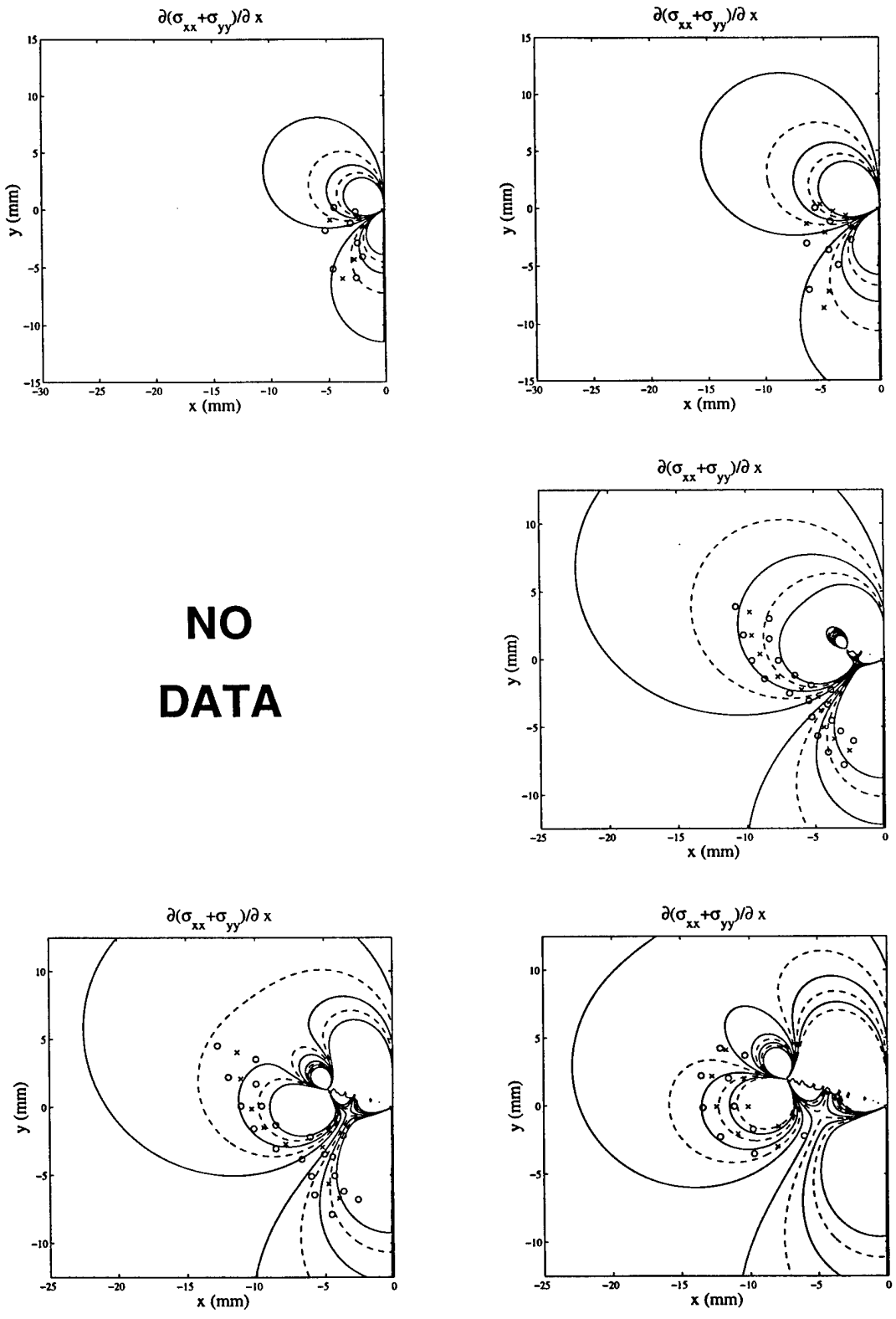

Figure 4.13: Sequence of fringe pattern fits for shear band initiation at the die corner in an AISI 4340 steel specimen impacted at 45 m/s.

terns could be determined. Figure 4.13 displays the expected fringe patterns along with the digitized data points. Again, solid lines and circular points represent dark fringes and dashed lines and $\times$ points represent light fringes. The five graphs correspond to the fringe pattern photographs of the same position in Figure 4.12. As stated before, data could not be obtained from the picture at 22.6μs due its poor quality. The y-axis corresponds to the edge of the specimen, with the positive y-axis in contact with the die face and the negative y-axis a free surface. The first two graphs are for a purely mode I crack stress field. Interference from reflected waves allows only a portion of the fringes to be digitized, but these points agree well with theory in the regions. The last three graphs include a cohesive zone emanating from the origin and propagating at an angle of 75^o from the die face (positive y-axis). The first order fringes were not digitized due to the distortion of the fringes with those from the notch tip. Also, only points below the shear band were digitized because of the presence of the aperture spot against the die face above the shear band. For the regions away from large interference, good agreement is shown. Near the shear band propagation axis, the points begin to diverge away from the expected fringe pattern.

The stress intensity factors measured from the photographs are shown in Figure 4.14 plotted with the dimensionalized stress intensity factor history from finite element analysis. For the two data points where only the mode I crack solution is applicable, good agreement with the finite element solution is seen. However, after the shear band begins to propagate, another dramatic increase in the stress intensity factor occurs. And similar to the notch tip history, an apparent steady state value is reached. The last estimate for the stress intensity factor before initiation begins is 200 MPa$\sqrt{\text{m}}$. This should be viewed as a low estimate as the shear band seems to initiate after this frame, but fringe analysis was hindered due to the quality of those frames. In the previous chapter, the initiation stress intensity factor for AISI 4340 steel at the die corner is estimated to be 222 MPa$\sqrt{\text{m}}$, which agrees very well with the estimate provided in this chapter.

The shear stress used for the cohesive zone calculations for the theoretical fringe patterns

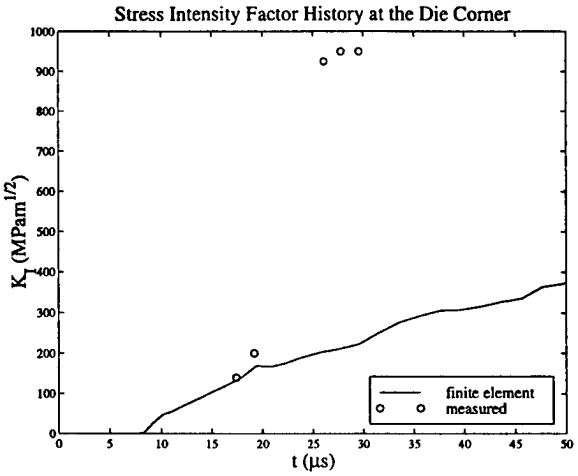

Figure 4.14: Stress intensity factor history at the die corner from measured values and finite element analysis of an AISI 4340 steel specimen impacted at 45 m/s.

is a constant 2.5 GPa. The fringes that showed the most change due to variations in the shear stress were at the shear band tip and above the shear band. Unfortunately, these are the same fringes eliminated by the large aperture spot at the die face. Though this value seems very high, the tension test data from the previous chapter gives a yield strength of 1.37 GPa for 4340 steel, it gives the best fit for the fringes. It is known from the annual report for this contract filed in 1997 that in these tests, a higher $\dot{K}$ exists at the die corner than at the notch tip. The high shear stress could be a result from the high loading rates involved. The increased $\dot{K}$ may also explain the greater increase in the stress intensity factor after shear band initiation. For the notch tip, the stress intensity factor almost tripled from initiation to the apparent steady state value. The initiation value at the die corner increases by a factor of about 4.5, possibly due to the higher loading rates. The high shear band speed of 1020 m/s is much higher than for the notch tip shear band in C300. Shear band speed is known to scale with loading rate [11], and these three facts support the conclusion that there is a higher $\dot{K}$ at the die corner than at the notch tip for a given impact speed.

Though the results of the test are very promising, there are some aspects of the test that need to be discussed. The first issue is the large aperture spot that forms along the die face above the propagating shear band. As the compressive wave impinges on the die

face, the material expands through a Poisson effect, but friction between the specimen and die may prevent this expansion at the die face. Large curvatures may then form at the edge of the specimen reflecting light at a large enough angle to not be included in the shearing interferometer, thus causing a dark area on the film. The aperture spot eliminates data from both the purely mode I crack stress field as well as shear band propagation data. Most notably, determination of the shear stress in the band emanating from the die corner becomes very difficult. The troubling part of the aperture spot is that it is a result of three dimensional deformation, while all the theoretical modeling is two dimensional in nature. There is evidence, though, that the aperture spot only affects a local region and not the entire stress field. As the shear band propagates away from the die corner, the fringes exhibit a greater amount of curvature, as shown in the last photograph of Figure 4.12, which is consistent with the theoretical fringe patterns. There are two other dark regions in the area under analysis which are expected from the theoretical fringes. Along the path of shear band propagation, a long dark region forms and expands with subsequent shear band growth. This shear band aperture spot is easily seen in the 27.8 and 29.6 μs photographs in Figure 4.12. Another dark region in the last photograph extends almost perpendicularly from the shear band aperture spot. This region again is expected from the high density of contour lines seen in the last graph of Figure 4.13. As much of the deformation field away from the die face aperture spot agrees with theory, its effect is assumed to be local and not distort the rest of the deformation field. In future tests however, steps should be taken in future tests to eliminate curvature in the specimen to make more accurate measurements and to ensure that a two dimensional analysis is valid.

One other phenomenon that needs to be examined is the dramatic increase in the stress intensity factor observed at shear band initiation. This is seen by Kalthoff [40] and in both tests conducted here. It does not appear to be geometry specific as it occurs at initiation at the notch tip and at the die corner. As stated earlier, the cohesive zone stresses near the shear band tip begin to exhibit a singularity stronger than the crack tip square root

singularity. The cohesive zone stresses were modeled as a constant value, but this may not be true. There may be a distribution where the shear stresses are higher near the shear band tip and decrease farther away from the band tip. A schematic of this is shown in Figure 4.15. Just as a finite distributed load on an elastic half space will resemble a point load away from the area of application, the shear stress distribution may be different than the constant stress assumed, which may lead to a greater singularity in the elastic stresses. This in effect would increase the measured value of a stress intensity factor while using an assumed square root singularity. More tests should be done and a more detailed analysis completed, though, before any formal conclusions are drawn.

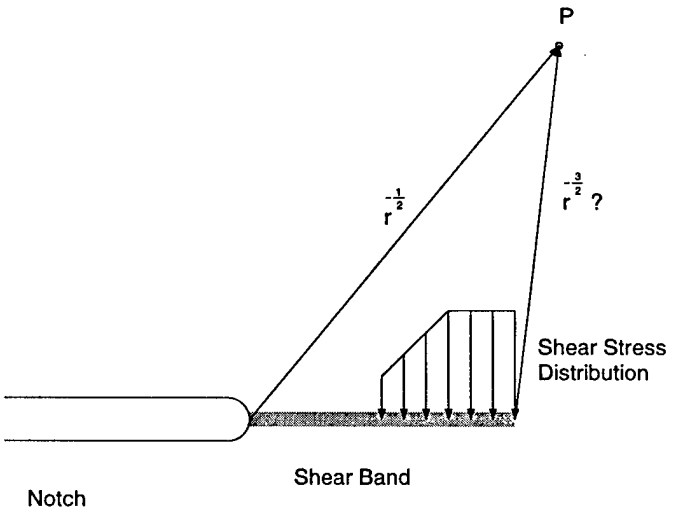

Figure 4.15: Schematic of possible shear stress variation within the shear band.

4.4 Conclusion

The coherent gradient sensing technique is used to examine the stress fields around adiabatic shear bands initiating at a notch tip and a die corner. The stress fields around the notch tip and die corner are modeled using the mode II and mode I stationary crack tip stress fields respectively. The shear band is modeled as a cohesive zone composed of shear point loads acting on a propagating crack face. In this way, the dynamics of the band propagation can be captured and the stress intensity factors K_{II} and K_I can be separated from the cohesive

zone shear stress during the fitting procedure.

For the notch tip in C300, shear bands are observed to initiate at a stress intensity factor of K_i=95 MPa$\sqrt{\text{m}}$. The shear band propagates at an average velocity of 650 m/s while the average shear stress within the band is 2.1 GPa. Initiation at the die corner in a 4340 steel specimen occurred at a stress intensity factor of about 200 MPa$\sqrt{\text{m}}$, though this is probably a low estimate. Average shear band speed and cohesive zone shear stress are 1020 m/s and 2.5 GPa. In both geometries, a large increase in the stress intensity factor is observed after shear band initiation. A steady state value is eventually reached. In the die corner initiation tests, greater shear band velocities and factors of increase for the stress intensity factor confirm that a greater $\dot{K}$ exists at the die corner.

Though the presence of a large aperture spot on the die face prevented full fringe patterns from being recorded, it is seen that there does exist an elastic stress field around the adiabatic shear band which can be predicted. The validity of the small scale yielding assumption is confirmed, and with continued experimental refinements, the use of CGS to study shear band initiation in different geometries can lead to accurate measurements of initiation properties.

Bibliography

[1] Y. Bai and B. Dodd. *Adiabatic Shear Localization: Occurrence, Theories and Applications.* Pergamon Press, New York, 1992.

[2] H.C. Rogers. Adiabatic plastic deformation. *Ann. Rev. Mater. Sci.*, 9:283–311, 1979.

[3] C. Zener and J.H. Holloman. Effect of strain rate upon plastic flow of steel. *Journal of Applied Physics*, 15:22–32, 1944.

[4] R.C. Batra, X. Zhang, and T.W. Wright. Critical strain ranking of 12 materials in deformations involving adiabatic shear bands. *Transactions of the ASME*, 62:252–255, March 1995.

[5] T.G. Shawki. An energy criterion for the onset of shear localization in thermal viscoplastic materials, Part I: Necessary and sufficient initiation conditions. *Transactions of the ASME*, 61:530–537, September 1994.

[6] T.G. Shawki. An energy criterion for the onset of shear localization in thermal viscoplastic materials, Part II: Applications and implications. *Transactions of the ASME*, 61:538–547, September 1994.

[7] R.C. Batra and Z. Peng. Development of shear sands during the perforation of a steel plate. *Computational Mechanics*, 1996.

[8] R.C. Batra and C.H. Kim. Analysis of shear banding in twelve materials. *Int. J. Plasticity*, 8(4):425–452, 1992.

[9] L. Chen and R.C. Batra. Analysis of thermoviscoelastic instability at an impact loaded crack tip. *unpublished*, 1997.

[10] J.J. Mason, A.J. Rosakis, and G. Ravichandran. Full field measurements of the dynamic deformation field around a growing adiabatic shear band at the tip of a dynamically loaded crack or notch. *J. Mech. Phys. Solids*, 42(11):1679–1697, 1994.

[11] M. Zhou, A.J. Rosakis, and G. Ravichandran. Dynamically propagating shear bands in impact-loaded prenotched plates I. Experimental investigations of temperature signatures and propagation speed. *J. Mech. Phys. Solids*, 44(6):981–1006, 1996.

[12] G. R. Irwin. Basic concepts for dynamic fracture testing. *Transactions of the ASME. Journal of Basic Engineering*, 91(3), September 1969.

[13] G. R. Irwin. Crack toughness testing of strain-rate sensitive materials. *Transactions of the ASME. Journal of Engineering for Power*, 86(4), October 1964.

[14] F.A. McClintock and G.R. Irwin. Plasiticity aspects of fracture mechanics. In *Symposium on Fracture Toughness Testing and its Applications.* American Society for Testing and Materials, 1965. Special Technical Publication No. 381.

[15] J. Eftis and J.M. Krafft. A comparison of the initiatioj with the rapid propagation of a crack in a mild steel. *Transactions of the ASME. Journal of Basic Engingeering*, 87(1), March 1965.

[16] J.F. Kalthoff and S. Wrinkler. Failure mode transition at high rates of shear loading. In C.Y. Chiem, H.-D. Kunze, and L.W. Meyer, editors, *Impact Loading and Dynamic Behavior of Materials*, pages 185–195, 1987. Vol. 1.

[17] J.J. Mason, J.A. Zimmerman, and K.M. Roessig. The effects of aging condition on shear localization from the tip of a notch in maraging steel. *to appear Journal of Material Science*, 1998.

[18] M. Zhou, G. Ravichandran, and A.J. Rosakis. Dynamically propagating shear bands in impact-loaded prenotched plates II. Numerical simulations. *J. Mech. Phys. Solids*, 44(6):1007–1032, 1996.

[19] R.C. Batra and N.V. Nechitailo. Analysis of failure modes in impulsively loaded pre-notched steel plates. *Int. J. Plasticity*, to appear.

[20] Y.J. Lee and L.B. Freund. The stress intensity factor due to normal impact loading of the faces of a crack. *Int. J. Engng Sci.*, 12:179–189, 1974.

[21] K. Ravi-Chandar. On the failure mode transitions in polycarbonate under dynamic mixed mode loading. *Int. J. Solids Structures*, 32(6/7):925–938, 1995.

[22] J.J. Mason. Investigations of shear localization in energetic materials systems. Technical report, AFOSR Summer Research Extension Program, 1995.

[23] K.M. Roessig and J.J. Mason. Dynamic stress intensity factors in a two dimensional punch test. *submitted to Eng. Frac. Mechanics*, 1997.

[24] K.M. Roessig and J.J. Mason. Adiabatic shear localization in the dynamic punch test, Part I: Experimental investigation. *submitted to Int. J. of Plasticity*, 1997.

[25] K.M. Roessig and J.J. Mason. Adiabatic shear localization in the dynamic punch test, Part II: Numerical simulations. *submitted to Int. J. of Plasticity*, 1997.

[26] M.F. Dillmore and J.C. Foster. Mechanical properties of high strength steels for hard target warhead applications. In *presented at ADPA Conference*, Huntsville, AL, 1995.

[27] W. Ramachandran, X.J. Zhang, R.W. Armstrong, W.H. Holt, Jr. W. Mock, G. Soper, and C.S. Coffey. In *Microstructure/Property Relationships in Titanium Aluminides and Alloys*. The Minerals, Metals, and Materials Society, 1991.

[28] J.J. Mason, A.J. Rosakis, and G. Ravichandran. On the strain and strain-rate dependence of the fraction of plastic work converted to heat: An experimental study using high speed infrared detectors and the kolsky bar. *Mechanics of Materials*, 17(2-3), 1994.

[29] A.K. Zurek. The study of adiabatic shear band instability in a pearlitic 4340 steel using a dynamic punch test. *Metallurgical and Material Transactions A*, 25A:2483–2489, 1994.

[30] K.L. Johnson. *Contact Mechanics.* Cambridge University Press, Melbourne, Australia, 1994.

[31] G.M.L. Gladwell. *Contact Problems in the Classical Theory of Elasticity.* Sijthoff & Noordhoff, Alphen aan den Rijn, The Netherlands, 1980.

[32] A. Nadai. *Theory of Flow and Fracture of Solids*, volume 2. McGraw-Hill Book Company, 1963.

[33] S.P. Timoshenko and J.N. Goodier. *Theory of Elasticity.* McGraw-HIll Book Company, New York, 3rd edition, 1976.

[34] H. Tada, P.C. Paris, and G.R. Irwin. *The Stress Analysis of Cracks Handbook.* Paris Productions Inc., St. Louis, Missouri, 2nd edition, 1985.

[35] R.W. Hertzberg. *Deformation and Fracture Machanics of Engineering Materials.* John Wiley & Sons, Ney York, 3rd edition, 1989.

[36] C.R. Brooks. *Metallurgical Failure Analysis.* McGraw-Hill, Inc., New York, 1993.

[37] W.H. Holt, Jr. W. Mock, W.G. Soper, C.S. Coffey, V. Ramachandran, and R.W. Armstrong. Reverse-ballistic impact study of shear plug formation and displacement in ti6al4v alloy. *Journal of Applied Physics*, 73(8):3753–3759, April 1993.

[38] A. Seweryn and K. Molski. Elastic stress singularities and corresponding generalized stress intensity factors for angular corners under various boundary conditions. *Engineering Fracture Mechnaics*, 55(4):529–556, 1996.

[39] Y.J. Lee. *Problems Associated with Dynamic Fracture Under High Strain Loading.* PhD thesis, Division of Engineering, Brown University, Providence, RI, 1990.

[40] J.F. Kalthoff. Shadow optical analysis of the fracture behavior under high rates of shear loading. In *SPIE: Proc. Int. Conf. Photomechanics and Speckle Metrology*, volume 814, pages 531–538, 1988.

[41] M.L. Dunn, W. Suwito, and S Cunningham. Fracture initiation at sharp notches: Correlation using critical stress intensity factors. *Int. J. Solids Structures*, 34(29):3873–3883, 1997.

[42] L.B. Freund. *Dynamic Fracture Mechanics.* Cambridge University Press, Cambridge, NY, 1990.

[43] J.J. Mason, J. Lambros, and A.J. Rosakis. On the use of a coherent gradient sensor in dynamic mixed-mode fracture mechanics experiments. *J. Mech. Phys. Solids*, 40(3):641–661, 1992.

[44] H.V. Tippur, S. Krishnaswamy, and A.J. Rosakis. A coherent gradient sensor for crack tip deformation measurements: Analysis and experimental results. *Int. J. of Fracture*, 48:193–204, 1991.

[45] M.F. Kanninen and C.H. Popelar. *Advanced Fracture Mechanics.* Oxford University Press, New York, 1985.

[46] H.V. Tippur, S. Krishnaswamy, and A.J. Rosakis. Optical mapping of crack tip deformations using the methods of transmission and reflection coherent gradient sensing: A study of crack tip K-dominance. *Int. J. of Fracture*, 52:91–117, 1991.

REPORT DOCUMENTATION PAGE

Form Approved
OMB No. 0704-0188

1. AGENCY USE ONLY *(Leave blank)*	2. REPORT DATE	3. REPORT TYPE AND DATES COVERED
	June 1998	Annual, June 1997 - May 1998

4. TITLE AND SUBTITLE
Application of Dynamic Fracture Mechanics Concepts to Composites: Annual Report 1998

5. FUNDING NUMBERS
G ND 0014-96-0774
PR 96 PR 05511-00

6. AUTHOR(S)
James J. Mason

7. PERFORMING ORGANIZATION NAMES(S) AND ADDRESS(ES)
University of Notre Dame
Department of Aerospace and Mechanical Engineering
365 Fitzpatrick Hall
Notre Dame, IN 46556

8. PERFORMING ORGANIZATION REPORT NUMBER
Structural/Solid Mechanics Laboratory Report No. 9813

9. SPONSORING / MONITORING AGENCY NAMES(S) AND ADDRESS(ES)
Office of Naval Research
800 N Quincy St.
Arlington, VA 22217-5560

10. SPONSORING / MONITORING AGENCY REPORT NUMBER

11. SUPPLEMENTARY NOTES
Portions of this report have been accepted for publication in "Experimental Mechanics", submitted to "Journal of Applied Mechanics" or submitted to "International Journal of Fracture".

a. DISTRIBUTION / AVAILABILITY STATEMENT
Approved for public release, distribution unlimited.

12. DISTRIBUTION CODE

13. ABSTRACT *(Maximum 200 words)*

This report summarizes the work completed in the year June 1997 – May 1998. The report is divided into two parts, one covering the work on orthotropic composites and the other covering the work on isotropic metals. Each part consists of two chapters which stand alone, each having been submitted, accepted or prepared for publication in a referred journal. Separate bibliographies are given for parts I and II. The work on composites has succeeded in producing fundamental, dynamic Green's functions solutions for cracks in orthotropic materials. These solutions may be used in calculating the stress intensity factor history on stationary cracks subjected to dynamic loading and may be very useful in predicting crack initiation under such conditions. Currently, experimental investigation of the application of these solutions to crack initiation in composites in two different configurations is beginning. It is expected that a report on that work will be submitted next year. The work on metals has been successful in experimentally demonstrating the usefulness of the dynamic stress intensity factor in predicting shear failure in metals under impact loads. This demonstration is predicted on the assumption that small scale yielding conditions exist in the experiments. The last chapter reflects an ongoing experimental investigation into the validity of that assumption. It seems to suggest that the assumption is correct, but further, more conclusive results are sought.

14. SUBJECT TERMS
Stress intensity factor, composites, shear localization, metals, punch tests

15. NUMBER OF PAGES
107

16. PRICE CODE

17. SECURITY CLASSIFICATION OF REPORT	18. SECURITY CLASSIFICATION OF THIS PAGE	19. SECURITY CLASSIFICATION OF ABSTRACT	20. LIMITATION OF ABSTRACT
Unclassified	Unclassified	Unclassified	